UNIVERSITY OF CALIFORNIA

Santa Barbara

Effects of Molecular Structure and Processing on

Morphology and Performance of Small Molecule Solar Cells

A dissertation submitted in partial satisfaction of the

requirements for the degree Doctor of Philosophy

in Materials

by

John A. Love

Committee in Charge:

Professor Thuc-Quyen Nguyen, Co-chair

Professor Guillermo Bazan, Co-chair

Professor Alan Heeger

Professor Craig Hawker

September 2015

The dissertation of John A. Love is approved.

_____

Craig Hawker

_____

Alan Heeger

_____

Guillermo Bazan, Committee Chair

_____

Thuc-Quyen Nguyen, Committee Chair

Effects of Molecular Structure and Processing on

Morphology and Performance of Small Molecule Solar Cells

iii

ACKNOWLEDGEMENTS

This dissertation and the work reported herein could not have been possible without the incredible encouragement, help and support I have always received from my family, friends, advisors and coworkers. It will not be possible to thank everyone individually, as I would like, thanks to the sheer number of important relationships and dear friends I have made since

starting on my quest five years ago. I would however, like to point out a few individuals whose contributions toward my success cannot be overstated.

First, and absolutely foremost, I want to acknowledge the unwavering love and support I have always received from my family. Despite some harassment about moving to California, you have always supported me. You have encouraged me to follow my own path, do what I enjoy, and do it well. I cannot express enough my gratitude for always having a support team and a place to come back to, a place to call home. I also want to thank all of the great friends I have made in Santa Barbara. From the crazy nights IV and downtown to sailing to wine tasting, my friends have helped me enjoy this PhD experience, and find a work-life balance.

From a technical standpoint, I have had the privilege of collaborating with an incredible cast of talented researchers, both within UCSB and across the globe. In particular I would like to thank the McGehee, and Toney groups at Stanford and the Ade group at North Carolina State with whom I have had the pleasure of many open collaborations. I would also like to acknowledge Anna Köhler, and her group at the University of Bayreuth, with whom I studied for two weeks, and in particular Markus Reichenberger who helped make my stay in Germany a fun and productive one. I also want to make special acknowledgement of Chris Takacs, who has been invaluable to me as a resource, teacher, and friend, whose tireless patience in teaching me how to use the TEM, led to much of the successful work reported in this dissertation.

I want to also thank all of my labmates from the Nguyen and Bazan groups, for making every day of these last five years fun, interesting and exciting. In particular, I think it is important to acknowledge all of the talented chemists whom I have been luck enough to work with, specifically Tom van der Poll, Greg Welch, Zac Henson, Ikuhiro Nagao, Jessi Coughlin, Chunki Kim, Jianhua Liu, Asta Lai, and Shu-hua Chu; your incredible materials make this work

instrumentation and of course, bringing me to Vietnam. Quyen deserves the most thanks, for allowing me to work in her lab, supporting, encouraging, and guiding me over these past five years. You allowed me to work on nearly anything I wanted, and always put me in the best position to succeed. You have let me learn new techniques, use all of the expensive instruments, and connected me with collaborators everywhere. I also have to thank you for encouraging me to present this work and sending me all across the world. I am so glad you took a chance on me five years ago, and I could not be happier with my choice of advisor and lab.

John A. Love

Home Address: 6 Shea Drive, Holliston MA, 01746
Phone: (508) 308-7961   **Email:** JackLove1212@gmail.com

(i) Education:

06/2010 **B.S. Chemistry, B.S. Physical Sciences**, Trinity College
08/2015 **Ph. D. Candidate**, **Materials** University of California, Santa Barbara

(ii) Honors/Awards:

2011/12 Scienceline Award for Outstanding Answerer

(iii) Research Experience

Research Exchange Student, University of Bayreuth, Germany, Advisor: Dr. Anna Köhler (08/2015)

Research Assistant, (Nanosystems Chemistry and Engineering Research summer REU program) University of California, Los Angeles, Advisor: Dr. Sarah Tolbert (06/2009)

Research Assistant, (NSF Theoretically Interesting Molecules) Trinity College, Hartford CT, Advisor: Dr. Tom Mitzel (2006-2010)

Graduate Student Researcher, University of California, Santa Barbara, Advisor: Dr. Thuc-Quyen Nguyen (2010-2015)

(iv) Publications:
1. "Non-basic high-performance molecules for solution-processed organic Solar Cells" van der Poll, T.S.; <u>Love J. A.</u>; Nguyen, T.-Q.; Bazan, G. C. *Adv. Mater.* **2012**, *24*, 3646-3649.

2. "Molecular solubility and Hansen solubility parameters for the analysis of phase separation in bulk heterojunctions" Duong, D.T.; Walker, B.; J Lin, J.; Kim, C.; <u>Love, J.</u>; Purushothaman, B.; Anthony, J.E.; Nguyen, T.-Q.; J. *Polym. Sci. B*: *Polym. Phys.* **2012**, *50*, 1405-1413.

3. "Film morphology of high efficiency solution-processed small-molecule solar cells" <u>Love, J. A.</u>; Proctor, C. M.; Liu, J.; Takacs, C. J.; Sharenko, A.; van der Poll, T. S.; Heeger, A. J.; Bazan, G. C.; Nguyen, T.-Q. *Adv. Funct. Mater.* **2013**, *23*, 5019-5026

4. "Solvent additive effects on small molecule bulk heterojunction solar cells probed in situ during spin-casting" Perez, L. A.; Chou, K. W.; <u>Love, J. A.</u>; van der Poll, T.

S.; Smilgies, D.-M.; Nguyen, T.-Q., Kramer, E. J.; Amassian, A.; Bazan, G. C. *Adv. Mater.* **2013**, *25*, 6380-6384.

5. "A silaindacenodithiophene-based molecular donor: morphological features and use in the fabrication of compositionally tolerant, high-efficiency bulk heterojunction solar cells" Love, J. A.; Nagao, I.; Huang, Y.; Kuik, M.; Gupta, V.; Takacs, C. J.; Coughlin, J. E.; Qi, L.; van der poll, T. Kramer, E. J.; Heeger, A. J.; Nguyen, T.-Q.; Bazan, G. C. *J. Am. Chem. Soc.* **2014**, *136*, 3597-3606.

6. "Topological considerations for the design of molecular donors with multiple absorbing units" Lai, L. F.; Love, J. A.; Sharenko, A.; Couglin, J. E.; Gupta, V; Tretiak, S.; Nguyen, T.-Q.; Wong, W.-Y.; Bazan, G. C. *J. Am. Chem. Soc.* **2014**, *136*, 5591-5594.

7. "Effects of processing conditions on recombination reduction in small molecule bulk heterojunction solar cells" Zalar, P.; Kuik, M.; Ran, N. A.; Love, J. A.; Nguyen, T.-Q. *Adv. Energy Mater.* **2014**, *4*,

8. "Ultrafast charge generation in an organic bilayer film" Kaake, L. G.; Zhong, S.; Love, J. A.; Nagao, I.; Bazan, G.C.; Nguyen, T.-Q.; Cao, Y.; Moses, D.; Huang, F., Heeger, A. J. *J. Phys. Chem. Lett.* **2014**, *5*, 2000-2006.

9. "Mobility guidelines for high fill factor solution-processed small molecule solar cells" Proctor, C.M.; Love, J.A.; Nguyen, T.-Q. *Adv. Mater.* **2014**, *26*, 5957-5961.

10. "Interplay of solvent additive concentration and active layer thickness on the performance of small molecule solar cells" Love, J.A.; Collins, S.D.; Nagao, I.; Mukherjee, S.; Ade, H.; Bazan, G. C.; Nguyen, T.-Q.;

11. "Mapping orientational order in a bulk-heterojunction with polarization-dependent photoconductive atomic force microscopy" Takacs, C. J.; Collins, S. D.; Love, J. A; Mikhailovsky, A. A.; Wyanands, D.; Bazan, G. C Nguyen, T.-Q.; Heeger, A. J.; *ACS Nano*. **2014**, *8*, 8141-8151.

12. "Understanding charge transfer state emission from solution-processed small-molecule organic solar cells" Ran, N. A.; Kuik, M; Love, J. A.; Proctor, C. M.; Nguyen, T.-Q. *Adv. Mater.* **2014**, *43*, 7405-7412.

13. "Use of a commercially available nucleating agent to control the morphologincal development of solution-processed small molecule bulk heterojunction organic solar cells" Sharenko, A.; Treat, N. D.; Love, J. A.; Toney, M. F.; Stingelin, N.; Nguyen, T.-Q. *J. Mater. Chem. A*. **2014**, *2*, 7308-7316.

14. "Probing the bulk heterojunction via nano-thermal analysis" Love, J.A.; Shagarian, K. Germanio, L.; Shetty, R.; Nguyen, T.-Q.; *(Submitted)*

15. "Engineering the morphology of a solution-processed small-molecule solar cell to reduce photo-chemical burn-in" Sachs-Quintana, I. T.; William R. Mateker, W. R.; <u>Love, J. A.;</u> Cheacharoen, R.; Heumueller, T.; Huang,Y.; Bazan, G. C.; Thuc-Quyen Nguyen, T.-Q.; McGehee, M. D. *(Submitted)*

16. "Triplet exciton formation in solution processed small molecule solar cells" Vath, S.; Tvingstedt, K.; Baumann, A.; Sperlich, A.; <u>Love, J. A.;</u> Nguyen, T.-Q.; Dyakonov, V. *(In Prep)*

17. "Solvent vapor annealing with low vapor pressure solvents leads to high degree of morphology control in small molecule solar cells" Lin, C.-H.; <u>Love, J. A.;</u> Nguyen, T.-Q.; (*In Prep*)

18. "Effects of solvent additive on S-shaped curves in small molecule solar cells" <u>Love, J. A.;</u> Chou, S.-H.; Huang, Y.; Kramer, E. J.; Nguyen, T.-Q.; Bazan, G. C. *(In Prep)*

19. "Understanding Charge Transport in Molecular Blend Films in terms of Order and Connectivity of Conductive Pathways." Proctor, C. M.; Kher, A.; <u>Love, J. A.;</u> Huang, Y.; Sharenko, A.; Bazan, G. C.; Nguyen, T.-Q.; *(In Prep)*

20. "Low Disorder Polymer Leads to Minimal Loss in Voc" Ran, N. A.; <u>Love, J. A.;</u> Huang, Y.; Ford, M.; Sadhanala, A.; Friend, R. H.; Nguyen, T.-Q.; Bazan, G. C. *(In Prep)*

21. "Controlling Molecular Orientation Through Solvent Additives" Takacs, C.J.; <u>Love, J. A.;</u> Ran, N. A.; Nguyen, T.-Q.; Chabinyc, M.; *(In Prep)*

22. "Effects of molecular orientation at donor acceptor interface on open circuit voltage" Ran, N. A.; <u>Love, J. A.;</u> Savikhin, V.; Toney, M. F.; Nguyen, T.-Q.; *(In Prep)*

23. "Multiple phase aggregation behavior of a small molecule organic semiconductor" Reichenberger, M.; <u>Love, J. A.;</u> Nguyen, T.-Q.; Kholer, A. *(In Prep)*

(v) Citation Information:
Total citations: 516
h-index: 7
(according to google sholar)

(vi) US Patent Applications:

1. "Inert solution-processable molecular chromophores for organic electronic devices" GC Bazan, TS Van Der Poll, TQ Nguyen, J Love - US Patent App. 13/800,396, 2013

(vii) Presentations:

1. "Small Molecule Organic Solar Cells" IEE Review, University of California at Santa Barbara, 04/2015 (poster)

2. "Controlling Molecular Order and Bulk Morphology of Organic Solar Cells" Erker Symposium, University of California at Santa Barbara, 02/2015 (oral)

3. "Small Molecule Solar Cells: Processing Control of Morphology" International Workshop on Advanced Materials Science and Nanotechnology, Ha Long City, Vietnam, 11/2014 (oral)

4. "Small Molecule Solar Cells: Processing Control of Morphology" International Conference on Electroluminescence and Organic Optoelectronics, Cologne, Germany, 09/2014 (oral)

5. "Small Molecule Solar Cells: Processing Control of Morphology" University of Bayreuth, Bayreuth, Germany, 08/2014 (oral)

6. "Small Molecule Solar Cells: Processing Control of Morphology" Stanford-UCSB symposium, University of California at Santa Barbara, 07/2014 (oral)

7. "New Materials for High Efficiency Tandem Solar Cells " CEEM Review University of California at Santa Barbara, 01/2014 (oral)

8. "Organic Solar Cells: Optimization and Characterization" Chalmers-UCSB Workshop, University of California at Santa Barbara, 09/2013 (oral)

9. "Small Molecule Bulk Heterojunction Solar Cells With High Open Circuit Voltages" CEEM Review, University of California at Santa Barbara, 06/2013 (poster)

10. "High Efficiency Small Molecule Solar Cells" São Paulo-UCSB Symposium, University of California at Santa Barbara, 05/2013 (oral)

11. "Organic Solar Cells: Controlling Film Morphology" Chemical Sciences Student Seminar, University of California at Santa Barbara, 05/2013 (oral)

12. "Film Morphology of High-Efficiency Small-Molecule Solar Cells" CEEM Review University of California at Santa Barbara, 01/2013 (oral)

13. "High Efficiency Small Molecule Solar Cells" International Conference on the Science and Technology of Synthetic Metals, Atlanta, GA 07/2012 (poster)

14. "High Efficiency Small Molecule Solar Cells" Gordon Research Conference, Lucca, Italy, 06/2012 (poster)

(viii) Other Activities and Affiliations:

Mentor: Chia-Hsi Jessica Lin (undergraduate), Eline Beggerman (masters)

Teaching:

Teaching assistant:
Chem 1 CL - General chemistry Lab: spring 2011
Chem 113A - Physical Chemistry: fall 2012
Chem 1 BL – General Chemistry Lab: spring 2015
Chem 153 – Advanced Analytical Techniques: spring 2012, spring 2014

Guest Lectures:
Chem 282C - Methods in Materials Chemistry 03/2013, 02/2014, 11/2014
Chem 153 - Advanced Analytical Techniques: 05/2014
Chem 1B, 1C - General Chemistry: 03/2011

Outreach Activities:

"Scienceline: Ask a scientist" Materials research Laboratory, 2010-2015

Chemistry demonstrations, (Ventura High School Visit), Department of Chemistry and Biochemistry 03/2011, and 03/2012, and 05/2015

"Science as a Career Outreach Project Experiment" Ventura High School, Bishop Diego High School, and Garden Street Academy, 12/2012, 09/2013, 12/2013

"Chemistry: the Elements" (Materials Research Laboratory) Monroe Elementary School, 05/2011 [on YouTube: https://www.youtube.com/watch?v=EtX2EJp23jk]

ABSTRACT

Effects of Molecular Structure and Processing on

Morphology and Performance of Small Molecule Solar Cells

by

John A. Love

This dissertation is concerned with the materials properties of conjugated molecules and their application in bulk heterojunction (BHJ) type solar cells with particular attention paid to the role of processing in determining morphology and device performance. Utilizing alternating electron rich and electron deficient moieties in the conjugated backbone results in tunable energy levels allowing molecules to be tailored to achieve desired optoelectronic characteristics. Two high performance materials in particular are studied in detail with respect to their physical and electronic properties. Specifically, high-resolution transmission electron microscopy, atomic force microscopy, UV-viable absorption spectroscopy and x-ray diffraction are used to examine the BHJ nanostructure in conjunction with current voltage measurements to elucidate structure property relationships. A series of molecules designed for specific goals such as improved absorption and electronics are also each briefly described. Though none of these materials give high efficiencies in BHJ solar cells compared with the first two materials, these smaller studies help demonstrate the intricacies of controlling morphology and how it can affect device performance.

TABLE OF CONTENTS

Chapter 1: Introduction

1.1 Motivation

With increasing concern over the burning of fossil fuels and their detrimental long-term effects on the natural balance on our planet, the need for alternative, renewable energy sources is imminent. Solar energy is widely recognized as an essential component of future global energy production as there is a near limitless supply, and solar cells can convert sunlight directly to electricity with no emissions. However, solar energy technologies are not yet widespread, as they remain prohibitively expensive to compete with fossil fuels on a large scale, and require significant energy and resources for production. Organic solar cells offer the promise of low cost production and scalability.

1.2 Organic Solar Cells

The photovoltaic effect was first observed by Alexandre-Edmond Becquerel in 1839, and refers to the direct transduction of irradiated light into electric current. Traditionally, photovoltaic devices, or solar cells, are made from a semiconductor such an absorbed photon promotes an electron from the valence band to the conduction band to create a free electron and leave behind a free positive charge called a hole which when collected form an electric current.

Electronically active carbon based materials were first rigorously studied and implemented in devices in the 1970's, ultimately leading to the 2000 Nobel Prize in Chemistry. Materials with extended π-conjugated systems such as polyacetylene were found to conduct charge particularly when doped. Organic semiconductors differ from traditional

semiconductors in that they do not undergo band transport. Instead, it has been shown that free charges "hop" from one discrete energy state to another in a thermally activated process. While a photovoltage was first observed in organometallic materials in 1958, and the pioneering semiconducting polymer research started in the late 1970's, the first major breakthrough in organic photovoltaic (OPV) research did not occur until 1986, when Tang et al. paired two organic semiconductors in a bilayer configuration.[1]

1.2.1 Donor-Acceptor Bilayer Device

Most organic materials inherently have a low dielectric constant, with most organic semiconductors falling in the range of 3 to 4 at relatively high frequencies.[2] When a photon is absorbed, and an electron is promoted from the highest occupied molecular orbital (HOMO) to the lowest unoccupied molecular orbital (LUMO) leaving behind a positively charged hole, the charges form a Frenkel exciton, a highly-localized, coulombically bound electron-hole pair. This makes direct conversion of absorbed photons to free charge carriers incredibly inefficient, with quantum efficiencies under 1%. This is in contrast to what happens in inorganic semiconductors, in which high dielectric constants provide sufficient electric field screening to separate the electron and hole a radius larger than the lattice spacing, which leads to high yields of photogenerated free charges.

The key innovation in Tang's bilayer device was the use of two semiconductors with different electron affinities and ionization potentials. This offset in HOMO and LUMO values provides a thermodynamic driving force for the transfer of an electron (or hole) from one material to the other. Thus, while an absorbed photon results in a localized exciton, if it can diffuse to the interface, there is a driving force for the electron to be on the material with high electron affinity (electron acceptor) and the hole to end up on the material with lower

ionization potential (electron donor). Utilizing asymmetric contacts, a built in electric field provides the driving force for holes to migrate to the anode and electrons to the cathode.

1.2.2 Bulkheterojunction (BHJ) Architecture

In the device described above, it is necessary for excitons to diffuse from where the photon is absorbed to the donor-acceptor interface. It has been found that exciton diffusion in organic semiconductors typically is on the order of 5-15 nm. Such thin layers cannot absorb a significant enough fraction of incident light and limits the maximum achievable efficiency in the bilayer structure. This led to the creation of the a bulk heterojunction (BHJ) a bicontinuous, interpenetrating network of donor and acceptor phases, first achieved by Heeger *et al*, who cast soluble semiconducting polyphenylenevinylene and fullerene derivatives directly from a single solution.[3] The increased interfacial area allowed for more efficient charge generation without limitations on photon absorption.

1.3 Device Operation

There are a number of different ways to describe the operation of organic solar cells, as it can be approached from an organic chemistry starting point using molecular orbital theory or from traditional semiconductor physics, describing band diagrams, and equivalent circuits. However, as the field is interdisciplinary, so will be the use of language and approach in this dissertation. Thus, rather than build up from a fundamental starting point, it is instructive to break the process down into steps, and examine each individually. Generally speaking, current generation can be thought of as three major steps: light absorption, charge generation, and charge extraction.

1.3.1 Absorption

One of the fundamental advantages of organic materials over some other semiconductors is having high extinction coefficients or absorptivities. As opposed to silicon, organic materials are direct bandgap semiconductors. This means that the maximum energy state in the valence band has the same crystal momentum as the minimum energy of the conduction band. In organic materials, the highest occupied HOMO and LUMO define the valence and conduction bands respectively. Upon irradiation, an electron can be promoted from HOMO to LUMO directly as it has the same momentum in both states, and does not require an additional phonon.

Without providing a more specific definition, the difference in energy between the HOMO and LUMO levels defines most generally describes the bandgap of the material. The nature of conjugation in the molecular backbone determines the position of these levels and thus can be modulated by molecular structure. First, increasing the conjugation length, that is the distance over which a charge can be delocalized, helps reduce the bandgap. Thus, organic semiconductors most commonly consist of alternating double bonds in a conjugated backbone, leading most often to highly planar structures.

The bandgap of a material can be further tuned using a donor-acceptor approach. This entails connecting alternating electron-rich and electron-deficient units in the conjugated backbone. This leads to the materials having significant quinoidal character, which would result from intramolecular charge transfer, leading to destabilized HOMO levels and stabilized LUMOs, reducing the bandgap. This approach has been used quite successfully in alternating copolymers to tune the bandgap, changing the spectral region of absorption, based on the strength of the electron-deficient and electron-rich moieties.

1.3.2 Charge Generation

As discussed above, once a photon is absorbed it does not often lead directly free charges, but rather a coulombically bound exciton, or hole electron pair. This exciton must diffuse to an interface between donor and acceptor. There are a number of mechanisms that can lead to exciton migration including cascade energy transfer, Forster transfer (mediated by Coulomb interactions), and Dexter transfer (electron exchange interactions). While the role of each of these processes is beyond the scope of this work, and is indeed an ongoing active topic of research, typically the exciton diffusion length in most organic semiconductors is measured to be 5-15 nm. If an exciton does not reach the interface, it can relax back to the ground state, emitting a photon in fluorescence, and not leading to current. This highlights the importance of interfacial area and the need for a bulk heterojunction in order to achieve high quantum yields of charges.

Once an exciton reaches the donor acceptor interface, the offset in energy levels provides a driving force for charge generation. For exactions originating in the donor, this requires donation of an electron to the acceptor, while for excitons in the donor, it is the equivalent donation of a hole to the donor. In either case, the exciton dissociation process goes through a charge transfer state. This is an interfacial state, which can be thought of as the coupling of the HOMO level of the donor and the LUMO level of the acceptor. The nature of the charge transfer state remains subject of much debate. However, the bound charge transfer state must, by electric field or thermal activation, dissociate to free charges, or else it can either radiatively or non-radiatively recombine to the ground state.

It should be noted that there is mounting evidence that charges can be formed more directly, forgoing a bound exciton and migration step, and proceeding to charge generation

at the donor acceptor interface directly upon absorption. Specifically, through transient absorption techniques, Heeger and others have demonstrated that in some systems, a large fraction of free charges are formed on the sub 100 fs timescale after a BHJ is irradiated with a pulsed laser.[4–6] Such fast formation precludes the idea of exciton diffusion, as such a process is observed on much longer timescales. Instead, it is proposed that upon absorption, before an exciton is formed, the delocalization of the wavefunction across a donor acceptor interface can lead to direct formation of free charges.

1.3.3 Charge Extraction

Once formed, the charges must be extracted without recombining. Due to the internal field in the operating regime of a solar cell, there is a driving force for free electrons and holes to migrate to the cathode and anode respectively. As mentioned these charges must undergo hopping transport. This leads low charge carrier mobilities, relative to inorganic semiconductors. Typical zero-field drift mobilities of OPV materials thus far have been below 10^{-2} cm^2/Vs while in single crystalline silicon and other ordered semiconductors they can be well over four orders of magnitude higher. This means at low fields, the charges can send significant time inside of the device. Furthermore, the low dielectric constant of organic materials means the charges are not as well screened as in traditional semiconductors. Thus, free holes and electrons can recombine bimolecularly, reducing the efficiency further. Thus, high charge carrier mobilities are necessary to effectively extract all of the generated charges.

1.3.4 Device Operation

In the dark, an organic solar cell is simply a diode as it rectifies current as a function of voltage. When no voltage is applied, there is no significant current in the device. In reverse

bias, there is very little dark current either, as there are nearly no intrinsic carriers and there is a significant barrier to injection of either holes from the cathode or electrons from the anode. The current that flows is leakage current due to non-infinite resistance. In the low forward bias regime, similar reasoning applies, and the current flows symmetrically as in reverse bias. However, as the applied voltage overcomes the built-in field, charges can begin to diffuse from the contacts into the device leading to a massive increase in current. Additional voltage leads to drift current. When holes are injected from the anode and electrons from the cathode, they recombine within the active layer; this is the working principle of an organic LED as well. A typical dark current measurement is shown below, with the leakage, drift, and diffusion regimes labeled.

While there are nearly no intrinsic carriers, as described above, illumination results in the generation of free charge carriers. Due to the built in field, these carriers can be swept out, resulting in a current density at short circuit, J_{SC}. Applying a negative bias increases the field within the device, which can help to efficiently sweep out free carriers. Under an operating voltage, that is, in the low forward bias regime, the field is reduced, making it harder to extract charges. Also, the photocurrent opposes the dark current, so the illumination current can be described as $J_{photo} - J_{Dark}$. Thus, there is a voltage at which $J_{photo} - J_{Dark} = 0$ or an open circuit voltage, V_{OC}. At open circuit, as there is no net current, so all of the charges must recombine.

The power a solar cell can produce is simply the product of the current produced and a particular voltage upon illumination. Thus scanning the current density as a function of voltage (a JV curve) determines the maximum power produced at a particular illumination intensity. The power conversion efficiency, PCE, is defined as the maximum output power

density compared to the total power of incident light, or 100 mW/cm^2 for AM 1.5 illumination intensity. It is practical to define a parameter called fill factor, *FF*, so as to put the maximum power in terms of V_{OC} and J_{SC}.

$$PCE = J_{SC} \times V_{OC} \times FF$$

Geometrically, the *FF* describes the "squareness" of the curve, as it says how close the maximum power point is to being on the rectangle defined by V_{OC} and J_{SC}. In general it is a good indicator of the voltage dependence of the device. More detailed descriptions of the physics of solar cells will be introduced as they become necessary.

1.4 Small Molecule Solar Cells

Following Heeger's initial report of the BHJ, nearly all of the most efficient, solution processed OPV systems utilized the same motif: a semiconducting electron donating polymer was mixed with a soluble fullerene derivative, and cast to form a BHJ. There are however several drawbacks to using polymers, namely the statistical distribution of molecular weights, and by consequence, difficulty in reproducing this distribution consistently for a given material, or across multiple materials systems for study. It has been shown that changes in molecular weight can have profound effects on efficiency.

An alternative to a polymeric system is to use oligomers or small molecules with well defined molecular weights. For example, people used α-sexithiophene or other oligothiophenes in place of polythiophenes. However, the efficiencies of these systems were often much lower than their polymeric counterparts. Prior to 2010, when this thesis work was first started, the highest performing small molecule system had been developed in our group by using a diketopyrrolopyrole based donor which gave a maximum $PCE = 4.4\%$.[7]

This was a big improvement over previous reports, and was the only example of a small molecule based donor system achieving a *PCE* > 3.5%.

In 2011 Bazan *et al.* introduced a new molecular framework featuring an alternating sequence of electron rich moieties and electron deficient pyridalthiadiazole units,[8] mimicking the "donor-acceptor" motif that had led to such great improvement in polymeric systems, but with even greater control of energy levels. Concurrently, Chen and coworkers were developing modified oligothiophenes, which began to show improvements in *PCE*. In early 2012, both classes of molecules were shown to achieve over 6% *PCE*.[9–11]

1.5 Conclusions

For organic solar cells to reach their potential as an alternative energy source, their efficiency must advance. Improved efficiencies directly translate to lower energy costs in dollars/Watt, as power per area or panel increases assuming equal production cost. Materials systems must first be designed with appropriate energy levels and band gap to maximize the potential of a device, balancing spectral absorption and achievable voltage. The small molecule architecture designed by Bazan et al provides a framework for tuning such properties.

Materials design however, is only the first step in creating high efficiency devices. Inefficiencies and losses can occur in every step of the current generation process. It is of vital importance to achieve nanoscale morphology with high interfacial area, yet high charge carrier mobility. Control over the phase separation process, mitigating kinetic and thermodynamic molecular interactions during or after casting can be quite a challenge. This dissertation will examine a series of materials systems which have been designed, optimized

and studied, to help push the efficiency of small molecule solar cells forward, while also providing insight into fundamental processes to help future systems.

Chapter 2: Experimental Techniques

2.1 Overview

One of the biggest challenges of organic photovoltaic (OPV) research is that it demands a multidisciplinary approach – understanding physics, chemistry, and materials engineering. It requires understanding interactions and properties on the molecular scale up to device design and electrical engineering. Thus, the research requires a multitude of techniques, probing physical, optical, and electronic properties of materials and films. This chapter describes in more detail the general experimental procedures used in this dissertation. This list is not exhaustive, as particular projects require more specialized techniques, but details the procedures I have used most often throughout this work. The unique properties, which make these small molecule materials useful in solar cell devices, include their ability to absorb light, form charges, and transport charges to electrodes. These properties arise from a combination of fundamental molecular properties and solid-state arrangement as well as the nanoscale morphology of the blends.

Measuring the energies of electronic states and transitions in real materials can be accomplished spectroscopically using UV-vis (Section 2.2) and cyclic voltammetry (CV) as described in Section 2.3. The way in which materials self-assemble into well-ordered crystalline domains can be quantified using X-ray diffraction (Section 2.4) and visualized using atomic force microscopy (AFM) as described in Section 2.5 or transmission electron microscopy (TEM) as described in Section 2.6. All of this information can be used to elucidate structure-property relationships, allowing us to understand and optimize molecular structures and processing conditions to achieve specific material characteristics. We ultimately wish to use these materials to make functioning devices as described in Section

2.7. And finally, the instrumentation and techniques used to characterize their photovoltaic properties of these devices are described in Section 2.8.

2.2 UV-Visible absorption

The ability of a compound to absorb visible light can be characterized by its UV-vis absorption spectrum. While information about the All UV/Vis absorption spectroscopy performed in this dissertation was carried out using either a Beckman Coulter DU 800 Spectrophotometer or more often a Perkin Elmer Lambda 750 spectrophotometer. Total absorption measurements were taken with the Perkin Elmer instrument equipped with a 60 mm integration sphere. In general, UV-Vis instruments generate light using a combination of a deuterium lamp for ultraviolet and a tungsten lamp for visible to near infrared wavelengths. The white light from the lamp is collimated into a beam by passing through a slit, and then split into component wavelengths with a diffraction grating. The amount of light transmitted through the sample (either a thin film on a transparent substrate, or solution in a cuvette) is compared to a reference (typically a transparent substrate or cuvette), and the absorbance is calculated. There are a number of ways to quantify the amount of light absorbed in a material, but in this dissertation, unless noted otherwise, "absorption" refers to absorbance. The absorbance, A, of a sample is defined by

$$A = log_{10}\left(\frac{\phi_i}{\phi_t}\right)$$

where ϕ_i is the radiant flux incident on, and ϕ_t is the radiant flux transmitted by the material.[12] As the absolute absorbance is not typically as important as the spectral shape, and variations in thickness across a film cause errors in calculations, so most absorption curves have been normalized arbitrarily.

The absorption of thin films is used to understand which regions of the solar spectrum will be absorbed. We often use the onset of this absorption edge as the definition of the optical bandgap of the material.
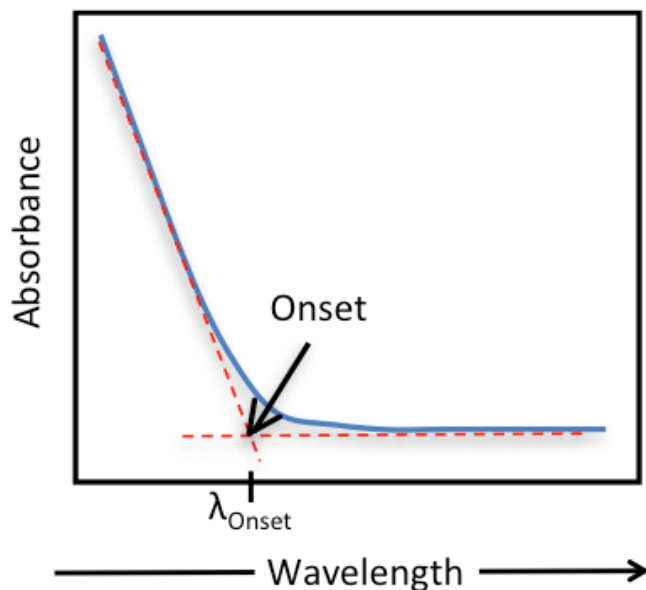
Figure 2.1. Finding the Onset of Absorption

To find the onset, the background at low energies is fit linearly, as is the tail edge of absorption. Where these two extrapolated lines cross is defined as the onset wavelength. This process is shown in Figure 2.1. From λ_{onset}, we can calculate the bandgap as $E_{optical} = (1240 \text{ nm /eV}) / \lambda_{onset}$.

2.3 Cyclic Voltammetry (CV)

Cyclic voltammetry (CV) is an analytical method that is used to measure the switching potential of a diffusion-controlled oxidation or reduction event. In this project it is primarily used to determine the HOMO and LUMO levels of materials. During a CV measurement, the current through the analyte is measured as function of an applied voltage The waveform

of this voltage is triangular in nature, scanning from a positive to negative potential and back

linearly as shown in Figure 2.2.[13]
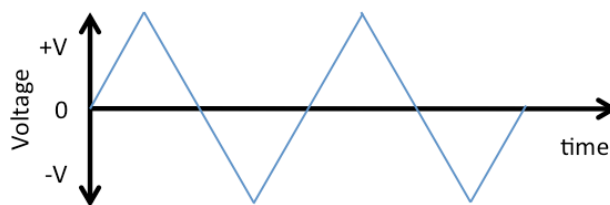
Figure 2.2. Waveform of Cyclic Voltammetry Signal

To carry out cyclic voltammetry three electrodes are used: a working electrode, a counter electrode and a reference electrode. The working electrode is a glassy carbon electrode, whose potential is varied according the waveform shown in Figure 2.3. As a reference electrode, we use an Ag/Ag+ electrode. The potential of this electrode is kept constant during the measurement. The counter electrode is a platinum wire, which conducts electricity from the signal source through the solution to the working electrode. All three electrodes are positioned in a cell containing the analyte and an excess of a nonreactive supporting electrolyte, $TBAPF_6$ in a solvent. The electrodes are connected to a linear sweep generator and a data acquisition system according to a circuit similar to that shown in Figure 2.3. [13]
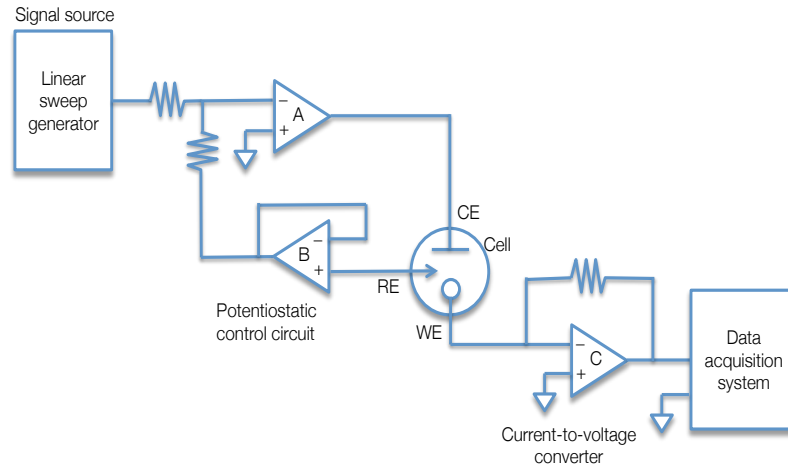
Figure 2.3. Schematic of Circuit Describing CV Instrument

Since the electrical resistance of the control circuit is very large, all current flows from the counter electrode to the working electrode. This current is measured as a function of time, and thus as a function of applied voltage, creating a voltammogram; an example voltammogram is shown in Figure 2.4. In this voltammogram we can see that initially, no current flows, but once a large enough voltage is applied an anodic current will start flowing. Based on this onset voltage, one can determine the energy needed to remove an electron from the analyte. In the reverse scan direction, the onset of the cathodic current signals the reduction of the analyte.
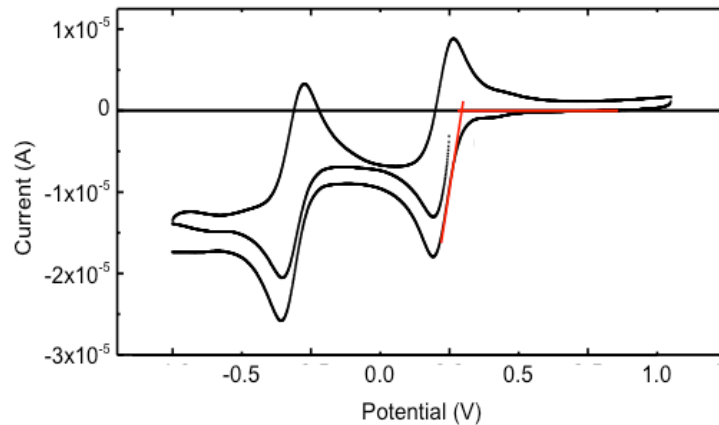
Figure 2.4. Example of a Voltammogram Using CV

In order to associate a particular voltage with an absolute energy level, it is necessary to use a standard to account for differences from one system to the next. We use the ferrocene/ferrocenium redox couple as a reference, which is accepted to have a reduction potential of 4.8 eV.[14] The HOMO and LUMO levels of the analyte can then be calculated using the following equations

$$E_{HOMO} = -(E_{OX}^{Fc/Fc+} + 4.8)$$

$$E_{LUMO} = -(E_{RED}^{Fc/Fc+} + 4.8)$$

Where

$$E_{OX}^{Fc/Fc+} = E_{OX}^{ONSET} - E_{1/2}^{Fc/Fc+}$$

$$E_{RED}^{Fc/Fc+} = E_{RED}^{ONSET} - E_{1/2}^{Fc/Fc+}$$

$E_{1/2}^{Fc/Fc+}$ is the average voltage for the maximum and minimum of a ferrocene curve taken right after the measurement on the analyte. This term is used to compensate for fluctuations in the data due to changes in the measurement setup.

2.4 X-ray Diffraction (XRD)

Organic molecules are often able to self-assemble into regularly repeating patterns or crystal structures in the solid state. In small molecule semiconductors, this crystallization tends to have desirable properties, as it decreases the energetic disorder of the material and leads to extended delocalization of electronic orbitals over multiple molecules, leading to improved charge generation and transport. These repeating patterns can be detected and characterized by thin-film or powder X-ray diffraction. A simplified schematic diagram of the x-ray diffraction process is illustrated in Figure 2.5.

Bragg's Law: $n\lambda = 2\,d\,\sin\theta$
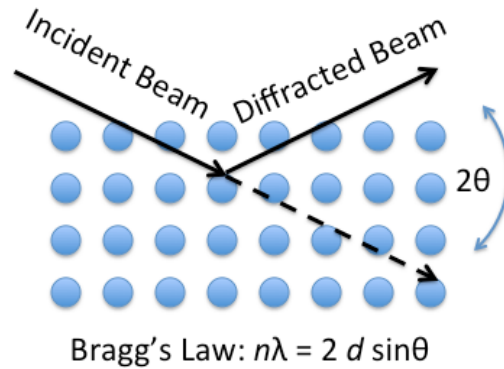
Figure 2.5. Schematic illustration of the X-rays (black lines) being diffracted by nuclei (blue dots) with a vertical spacing of d.

In this technique, a monochromatic X-ray beam with wavelength λ is generated and impinged upon a sample at an angle θ, and the diffracted beam is measured. If a material exhibits crystallinity, with a regular spacing between nuclei of distance d, the X-ray beam will be diffracted if and only if Bragg's equation is satisfied.[13][15] Bragg's equation states:

$$d = \frac{n\lambda}{2sin(\theta)}$$

where n is an integer value. Different materials exhibit unique packing motifs such that they generate unique patterns when diffraction intensity is plotted against diffraction angle (2θ). When a single crystal can be grown, this allows for the crystal structure to be identified. In polycrystalline materials, such as in a thin film, d-spacings can be identified in addition to the degree of crystallinity and order.

As crystallinity is three dimensional in a thin film, information can be learned about the texture or orientation of the crystallites depending on the direction of diffraction. The detector can be set to look at either in-plane or out-of-plane diffraction. Alternatively, if the intensity is high enough, 2-dimensional detectors are used to capture all diffracted beams at once. This is demonstrated in Figure 2.6.
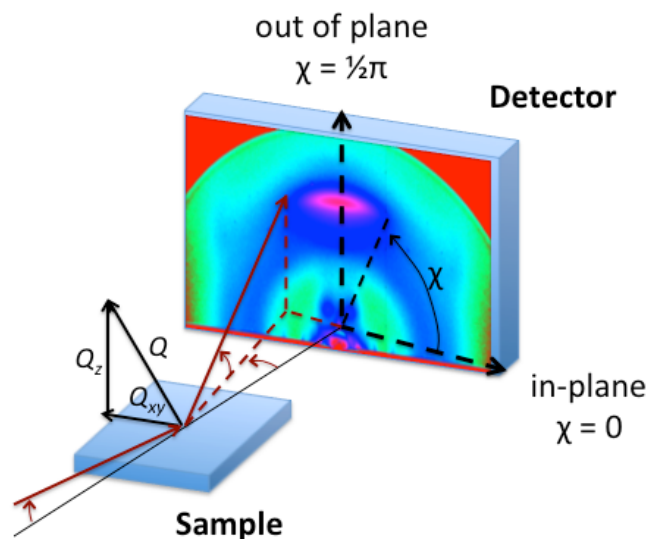
Figure 2.6. Schematic showing 2-Dimensional X-ray Diffraction

The XRD spectra presented in this dissertation were recorded using a variety of x-ray diffractometers, depending on the needs. Experiments performed in-house were taken using a Rigaku Smartlab High-Resolution Diffractometer at 45 kV and 40mA with a scanning rate of 0.004 degrees per second, and Cu Ka radiation (with wavelength of 1.5405 Å). As organic materials are not as well-ordered as inorganic crystals, we often made use of high intensity x-rays from the synchrotron radiation sources of the SLAC National Accelerator Laboratory and Advanced Light Source at Lawrence Berkeley National Lab.

2.5 Atomic Force Microscopy (AFM)

Organic bulk heterojunction (BHJ) films are typically on the order of 100 nm thick. Thus, features that are seen on the surface can often give a good indication of bulk structure. Thus, AFM is an indispensible tool for probing the morphology of BHJ films. A schematic illustration of an atomic force microscope is illustrated in Figure 2.7.
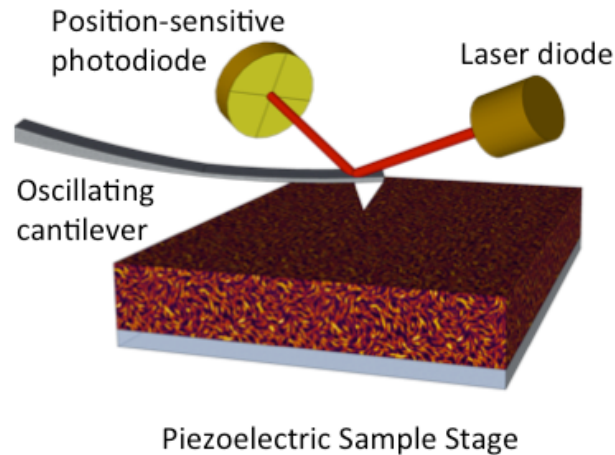
Figure 2.7. Schematic Illustration of an AFM

A sample is mounted on top of a piezoelectric stack, and a reflective cantilever is brought near the surface of the sample.[16] A laser beam is reflected off the surface of the cantilever and the reflected light is detected by a set of photodiodes. Small horizontal or vertical deflections in the cantilever cause the reflected beam to move away from its aligned position, which is detected on the photodiodes. In the simplest type of AFM, contact mode, the tip is brought in contact with the surface, causing the surface to push against the tip with a certain force, which depending on the spring constant, results in a deflection of the cantilever and a change in the signal of the photodiodes. The vertical position of the sample is adjusted to keep a constant force applied to the cantilever via a feedback loop between the photodiode and z-piezo.

The sample is then moved in the x and y direction the vertical movement of the z-piezo is recorded for each x and y coordinate in the scan area, typically in the range of about 10 μm × 10 μm, though larger or smaller ranges are possible. Because the instrument is capable of accurately moving the sample over arbitrarily small distances, the resolution of an AFM

19

image is ultimately limited by the size of tip that contacts the surface, which is typically tens of nanometers in diameter.

Tapping mode AFM is an imaging method in which the cantilever is driven to oscillate near its resonant frequency just above the surface of the sample. The oscillation of the tip causes a sinusoidal photodiode signal, where the amplitude of this signal is proportional to the amplitude of the tip's oscillation, which is monitored continuously. As the tip approaches the surface of the sample, forces between the tip and the surface cause a change in the amplitude of oscillation. The tip does not necessarily need to contact the surface in this process, which makes tapping mode especially suitable for imaging soft materials, such as organic BHJs, which might otherwise be perturbed by the force of a tip operating in contact mode.

Unless otherwise noted, all AFM in this dissertation was carried out using an Innova scanning probe microscope (Veeco) operating in tapping-mode, using silicon probes with spring constants of 40 N m^{-1} and resonant frequencies of 300 kHz (Budget Sensors).

2.6 Transmission Electron Microscopy (TEM)

Analytical characterization of BHJ morphology represents a major challenge to the field; as it requires studying multiple length scales, form the angstrom level distances between molecules to the bulk device structure to long-range molecular organization, which can span microns. Added to that is the sensitivity and challenge of achieving contrast between carbon-based materials. Finally, morphology is three-dimensional; a surface sensitive technique is not adequate. TEM can give incredibly high resolution imaging individual molecular planes but can also be used to look at larger structures, has multiple methods of inducing contrast, and is a transmissive technique meaning it samples the entire three-

dimensional volume. It should be noted there while there are a number of TEM techniques that can and have been used to study BHJ morphology, bright field TEM is used extensively throughout this dissertation, and thus will be described in detail.

2.6.1 Sample Preparation

For TEM imaging of organic films, sample preparation is typically quite simple. Films are prepared as they would be for devices, spin-cast atop a PEDOT:PSS layer. Carefully submerging the scored edge of the substrate into deionized water dissolves the underlying PEDOT causing the film to peel off of the substrate. The floating film is then collected along with a drop of water and cast onto a copper TEM grid with carbon support film and allowed to dry. A number of different support films have been used for different applications, but the majority of images in this dissertation are taken with a Protochips C-flat™, holey carbon-coated TEM support grid.

2.6.2 Phase Contrast Imaging

As both donor and acceptor in a BHJ blend are primarily carbon-based materials, it is not usually possible to distinguish between the two using simple mass contrast. In order to induce contrast, phase contrast is typically employed, by intentionally introducing a small amount of defocus. This method relies on the fact that as the electrons leave the source and travel through the column, they are coherent, that is they have the same energy and phase, and can be described as a plane wave. When the electrons interact with the sample they most often do so elastically, meaning they do not lose any energy. They do however undergo a modulation of phase that is material dependent. This can be thought of as analogous to light undergoing a change in phase as it passes through a material of different index of refraction. [15]

While in-in focus, this phenomenon does not produce enhanced contrast, however, defocusing the image slightly, allows the electrons to interfere with each other either constructively or destructively. This dependence of enhanced contrast on feature size, can be expressed mathematically by the contrast transfer function (CTF).[15] At small levels of defocus, the CTF favors contrast enhancement of small features, while at larger defocus values, artifacts can be introduced to complex interference patterns.[17] While the signals produced by this technique can be difficult to interpret sometimes, it is indispensible for imagining phase separation in many BHJ systems.

2.6.3 High Resolution Imaging

As mentioned above, phase contrast imaging can be used to enhance contrast via defocus. At relatively high magnification (typically 32,000 – 45,000 x zoom or higher) a small level of defocus (1 μm) shifts the contrast transfer function such that lattice fringes from alkyl stacking can be resolved. Practically this type of imaging requires a stable, parallel, well columated beam; thin, crystalline samples mounted on well-supporting substrates; and careful attention to minimizing beam exposure. To achieve these conditions, an FEI Titan 300 kV FEG TEM/STEM System is used in this dissertation. To minimize exposure, typically a beam size of 6 or 7 is used on the instrument, with exposure times of 2-4 seconds. This results in 50-200 counts per pixel in the final image. Furthermore, the beam is first prepared at one particular spot on a section of the sample and allowed to stabilize before being shifted off of the optical axis, to a fresh portion of sample a few microns away, at which point an image is immediately taken.[9]

2.6.4 cross sectional TEM

One of the challenges of TEM is that it provides a top-down view of a 3-dimensional surface. The entire sample is in focus, and thus it is impossible to know if the imaged features are at a particular interface or throughout the bulk; there is no depth information. While tomography can be used, it requires a large tilt series of images, adding to the beam exposure and sample damage. As an alternative, we employ cross sectional TEM by preparing TEM lamella using a focused ion beam (FIB) microscope. The instrument used in this dissertation is an FEI Helios FIB.

The difficulty in sing an FIB to mill out a TEM lamella is that it must be done at low operating voltages, and with limited exposure to avoid damage as much as possible. Typically, an organic film is first capped with a protective aluminum layer, evaporated thermally like a top contact. Platinum is then deposited (1 μm) on top to serve as further protection. A 20 μm × 1 μm × 5 μm deep slice is then milled out with the microscope operating at 30 kV and, at most, 0.92 nA. , The slice is then undercut, and transferred to a copper support using an in-situ Omni probe system. It is then progressively thinned further using a 30 kV ion beam operating at 93 pA or less. To minimize damage, the final thinning is performed with a 5 kV ion beam at 0.16 nA to a final thickness of ≈75 nm.

2.7 Diode and Solar Cell Fabrication

One of the major advantages of solution processed BHJ organic solar cells is the ease of fabrication. Its potential as a low cost energy solution hinges on fact that organic semiconductors can be printed quickly from solution. In the lab, the whole process, from bare substrates to a batch of working devices only takes a few hours. The typical solar cell device structure used in this dissertation consists of the BHJ layer sandwiched between a

transparent anode bottom contact and a metal cathode top contact. This is considered a conventional architecture, and is by far the most commonly used structure in this work, and thus the fabrication procedure will be described in detail. The overall procedure though is quite general. To fabricate devices in an inverted architecture or to create single carrier diodes, which are also studied, simply requires depositing different electrodes

The process begins with indium tin oxide (ITO) substrates, consisting of a 250 nm thick ITO layer on glass, purchased from a commercial supplier. The substrates are cleaned by scrubbing both sides in a detergent solution, followed by sonication (using an ultrasonic cleaner) in a detergent solution for 20 minutes, sonication in deionized water (2×10 minutes) sonication in acetone (10 minutes) and sonication in isopropanol (10 minutes). Substrates are next blown dry with nitrogen and stored in an oven at ~100 $^{\circ}$C until immediately prior to device fabrication. Care is taken to minimize exposure to dust and other airborne contaminants.

The deposition of layers begins with the commercially available conductive interlayer, polyethylenedioxythiophene:polystyrenesulfonate (herein referred to as PEDOT:PSS) which serves to create a smoother, more amenable surface than bare ITO, as well as selectively transport one type of charge carrier, holes. Unless otherwise noted, a water-based, p-doped PEDOT:PSS acid composite (H.C. Starck Baytron P 4083) was used as a conductive buffer, applied by filtering through a 0.45 μm PVDF syringe filter, spin-casting at 2500 rpm and annealing at 150 $^{\circ}$C for 30 minutes in ambient air. These conditions are found to yield a film about 45 nm thick with an RMS roughness of less than 1 nm on top of the ITO.

After annealing the PEDOT:PSS layer, the substrates are transferred immediately into a glovebox. The active layer is next deposited on top of the conductive buffer by spin coating.

The concentration and spin rate can be adjusted in order to achieve a specific film thickness, where lower concentrations and higher spin rates lead to thinner films. For most BHJs described in this dissertation, chlorobenzene was used as a solvent at a concentration of 35-40 mg of total semiconductor solids dissolved per mL, spin cast at 1750 rpm at as high acceleration as possible. Solutions were first prepared by weighing the solid, organic semiconductors in air, transferring to a Teflon-capped vial, then adding the solvent inside the glove box with an Eppendorf pipette. Solutions of all small molecule materials were typically heated at 60 $^{\circ}$C for higher overnight prior to casting. Filtering the solution after heating was typically not needed, though in some cases where solubility was a concern, did help produce a higher quality film.

Dispensing of solutions was typically done by taking a small (10-30 μL) aliquot of solution using a micropipette and dispensing it directly onto the substrate. After spin coating the active layer, the film may undergo post processing such as thermal or solvent vapor annealing. Thermal annealing was carried out by placing devices directly onto the surface of a hotplate for a certain amount of time; 10 minutes, unless otherwise noted.

Next, metal electrodes were typically applied to the top of the organic film by thermal evaporation through a shadow mask. Scratching through one edge of the organic layer using tweezers makes electrical contact to ITO. A thin (10 nm) layer of calcium topped with a thicker (80 nm) aluminum layer was typically used as the top electrode, Evaporations were carried out using an Angstrom Engineering-built evaporator fit with a cryopump which achieves a pressure of approximately 10^{-6} Torr, and a water level below 10^{-8} torr. High levels of water lead to oxidized calcium. The calcium is deposited at a rate of 0.1-0.2 Å/s

and aluminum started at 0.3 Å/s gradually increasing to a rate of 2.3 Å/s. A typical finished device is illustrated in Figure 2.8.
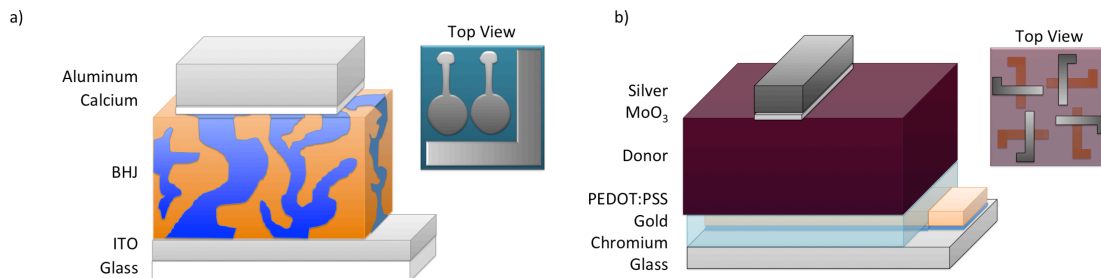
Figure 2.8. Cartoon Schematic of Standard Solar Cell and b) Hole-only Diode Architecture

When making charge selective devices, hole-only or electron-only diodes, it is useful to make "crossbar" structures as shown in Figure 2.8b. Using a metal contact on both the top and bottom improves conductivity, so the current through the device is not as limited by the resistance of the ITO. Furthermore, the small overlapping area reduces edge effects and on the contacts. The PEDOT layer (can also use MoO_3) allows for good wetting, as compared with depositing organics on metals.

2.8 Solar Cell Characterization

The most common, and perhaps important characterization technique for solar cells is the measurement of current density-voltage (*JV*) characteristics under simulated solar irradiation (100 mW/cm^2). From *JV* curves, efficiency can be calculated and much can be gleaned about the physics of the device. For more insight, *JV* characteristics are also studied as a function of light intensity and in the dark. Additionally, photocurrent was measured under spectrally resolved light in order to quantify the external quantum efficiency (*EQE*) or

26

incident photon-to-electron conversion efficiency (*IPCE*); that is, the number of electrical charges that are generated for each photon incident upon the device over the solar spectrum.

All *JV* measurements were performed in a glovebox. A Keithley 2400 source measure unit (SMU) controlled by a Lab View program was used to perform voltage sweeps while measuring the current. A 300 W Xenon arc lamp was used to simulate solar light, where light was passed through an AM1.5G global filter, focused into one end of a fiber optic cable while the other end of the fiber optic cable was positioned relative to the sample using micrometers in order to produce a light intensity of 100 mW/cm^2. The light was shown through the glass side of the sample, reflecting off of the top metal electrode as shown in Figure 2.9. The area of the device was defined by the total area of the evaporated metal, or by an aperture lined up with the device through which only a well-defined area of flux can pass. The light intensity was calibrated immediately prior to each testing session using and NREL certified photodiode put in place of the sample. For lower light intensities neutral density filters are placed in front of the light source, and the intensity is calibrated with the photodiode signal. For dark measurements, a beam stop is placed in the path of the light and a dark cover is placed over the glovebox in order to block out stray light.
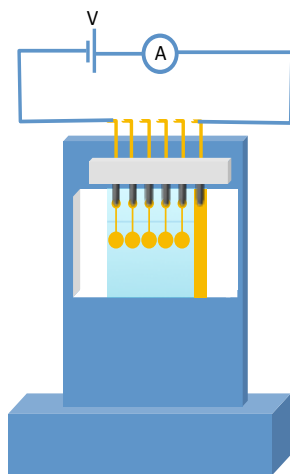
Figure 2.9. Schematic Illustration of Sample Testing Holder

For *EQE* measurements, a somewhat more complicated system is necessary, as at any particular wavelength of the spectrally pure light the intensity is low, which makes small changes in ambient light far more significant. As in the *JV* measurements, white light is first generated using a Xenon arc lamp but is then modulated into a periodic (138 Hz) signal using a chopper and a chopper controller and a function generator.

The modulated light is spectrally resolved using a diffraction grating, and focused into two fiber optic cables, one leading to the test device, and the other to a reference photodiode. The photocurrent signals produced by the device and the reference photodiode are measured by lock-in amplifiers which receive the same 138 Hz signal, so they only detect current which oscillates with the same frequency created by the function generator. The light is focused on the device so as to give the highest signal. The current produced by the device relative to the reference is then measured for each wavelength.

In order to calculate the *EQE*, calibration with a diode of known *EQE* is necessary. This calibration was also done with each testing session. Integrating the *EQE* and accounting for the known AM1.5 spectrum, it is possible to back calculate the J_{SC} from the *EQE*, which should and most often does match the *JV* measurement under white light.

2.9. Molecular Glossary

Throughout this dissertation, there will be a number of molecules studied and it can be a challenge to recognize and remember the differences, due to similarities in naming. While they will be introduced throughout the text, they also appear here as a glossary with their abbreviated names as well as any colloquial names that are used commonly at UCSB. The general architecture of the majority of donor materials studied is described by a central electron rich donor core, flanked symmetrically by electron deficient acceptor moieties with

additional donor moiety endcaps, or linearly referred to as a D^1-A-D^2-A-D^1 structure. A schematic is shown below along with the moieties used in this dissertation.
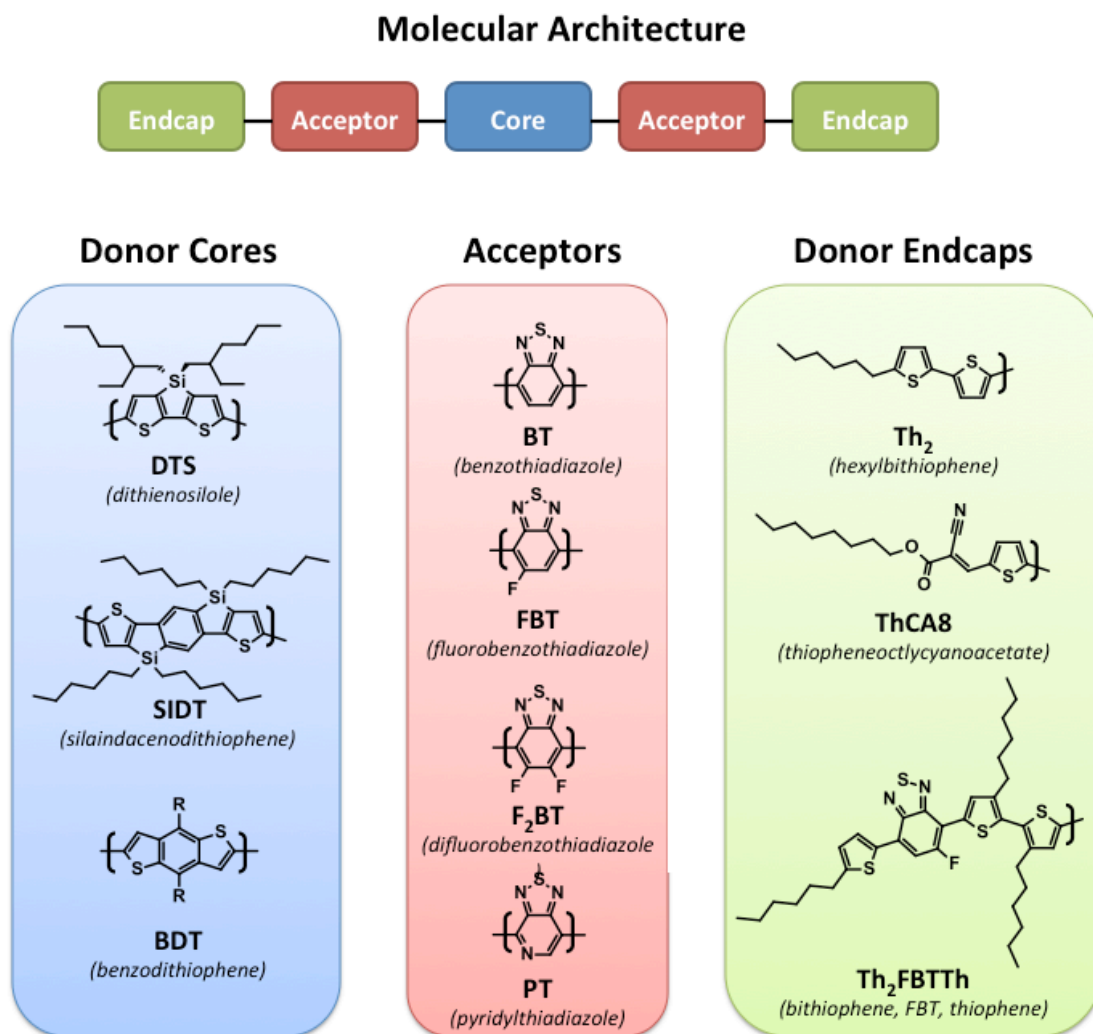
Figure 2.10. Molecular architecture and individual moieties incorporated in materials

The abbreviation scheme for this class of molecules is to start with the core and work outward. If the acceptor moieties contain a non-symmetry such as in PT or FBT, the direction with which the heteroatoms point, inward toward the central core or outward toward the endcap, determine if the material is "proximal" or "distal" respectively, which is placed at the beginning of the name. Thus, a typical name reads as "[p or d]-

[Core]([Acceptor][Endcap])₂" The abbreviations for each molecule are shown below along

with their abbreviations used colloquially at UCSB and in this dissertation.

p-DTS(FBTTh₂)₂
"T1"

p-SIDT(FBTTh₂)₂
"H1"

d-DTS(FBTTh₂)₂
"T2"

p-DTS(FBTThCA8)₂
"SH2"

DTS(F₂BTTh₂)₂
"F₂BT"

p-SIDT(PTTh₂)₂
"H2"

p-DTS(PTTh₂)₂
"G24"

p-BDT(FBTTh₂)₂
"BDT1"

d-DTS(PTTh₂)₂
"G9"

p-BDT(FBTTh₂)₂
"BDT2"

DTS(BTTh₂)₂
"BT"

PCBM   Vinazene   PDI

d-DTS(FBTTh₂FBTTh)₂
"AT1"
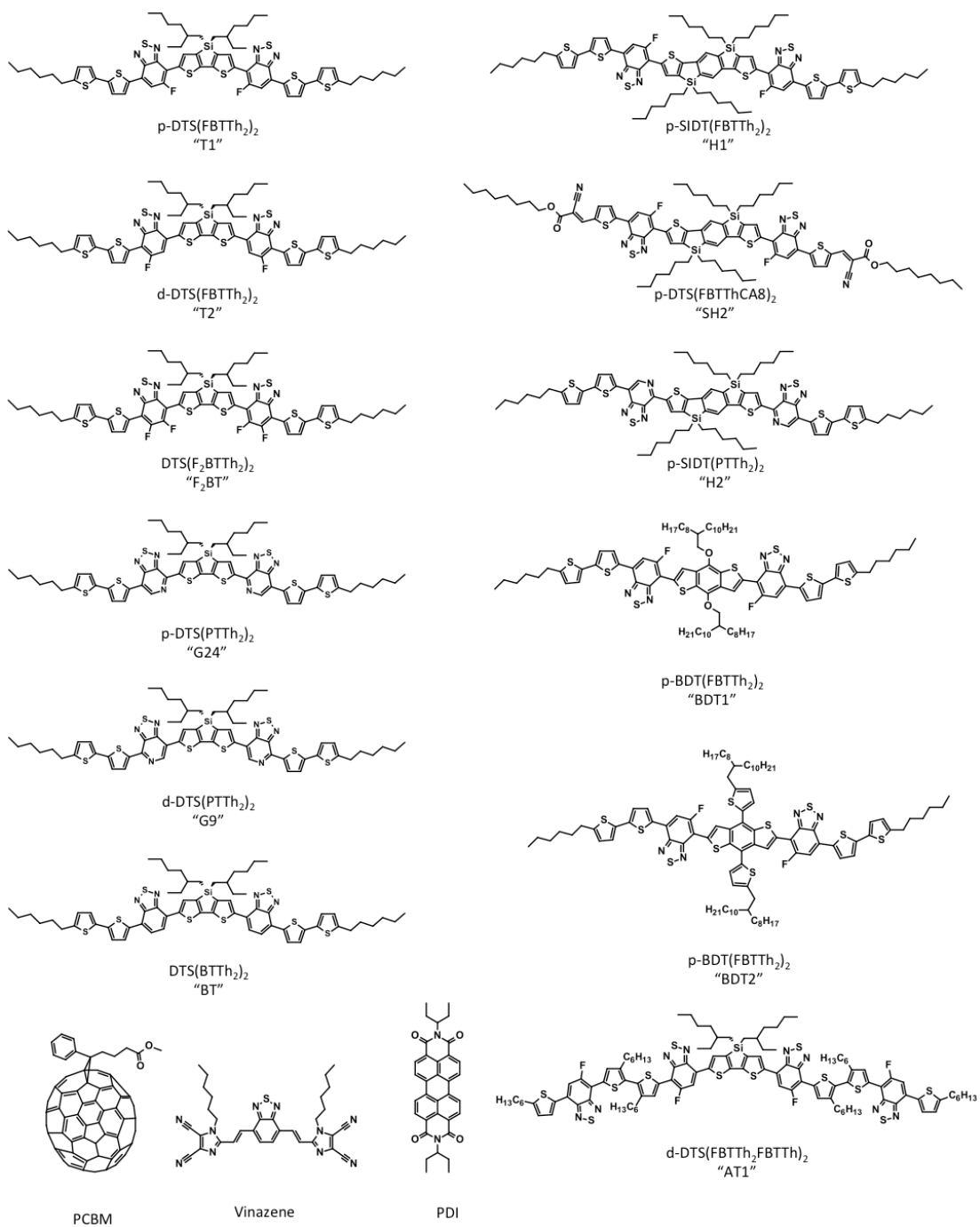
Figure 2.11. Molecular structures studied with shorthand names used for each

30

Chapter 3: A new small molecule: p-DTS(FBTTh$_2$)$_2$

3.1 Introduction

The successful framework developed by Bazan and coworkers largely hinged on the inclusion of [1,2,5]-thiadiazolo-[3,4-c]-pyridine heterocyle (here abbreviated as PT), which is an electron deficient unit.[18][9][8][19] Coupling PT to other readily available conjugated building blocks affords chromophores with desirable light harvesting properties and imparts asymmetry such that near quantitative site-selective cross-coupling can be achieved.[20][21][22] Bulk heterojunctions involving p-DTS(PTTh$_2$)$_2$ and other PT containing small molecules however, need to employ metal oxides, i.e. MoOx, as an anode interlayer. Using a PEDOT:PSS interlayer, much more common in organic photovoltaics (OPV) leads to a diminished performance, and in particular a loss in V_{OC}. This drop in performance has been attributed to the acidic nature of PEDOT:PSS, which ultimately results in protonation of the PT pyridyl nitrogen.[23] The need to develop materials with versatile utility that will not limit fabrication options led us to design a molecule with desirable optical, electronic and physical properties without the incorporation of sites sensitive to protonation. Instead, the key feature of the new chromophore is the incorporation of 5-fluorobenzo[c][1,2,5]thiadiazole (FBT) as the acceptor unit, which has previously found utility in organic polymers for high performance OPV devices.[24][25] The fluorine atom provides an electron-withdrawing functionality, and imparts asymmetry during synthesis,

but has no lone pairs of electrons that may be prone to participate in acid/base reactions.[26][27][28][29] The new molecule, abbreviated as p-DTS(FBTTh$_2$)$_2$ is shown below in Figure 3.1.
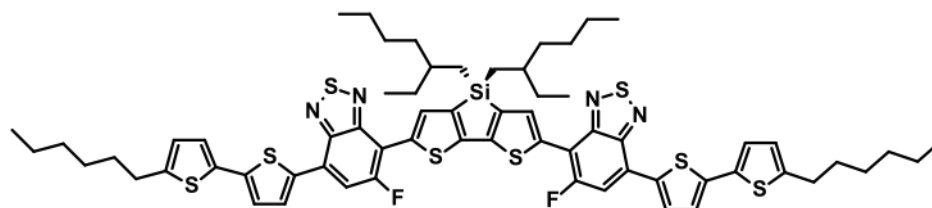
Figure 3.1. Molecular structure of p-DTS(FBTTh$_2$)$_2$

3.2 Molecular Properties

Optical properties were investigated using UV-visible absorption spectroscopy (Figure 3.2). In chloroform solution and in the solid state, p-DTS(FBTTh$_2$)$_2$ exhibits broad low energy transitions with favorable overlap with the solar spectrum, with λ_{max} values of 590 and 678 nm and λ_{onset} values of 670 and 800 nm, corresponding to optical band gaps of 1.85 and 1.55 eV, respectively. Thin film absorption exhibits vibronic structure, typical of ordered thin films.[30][31] The λ_{max} red-shift of 88 nm in going from solution to the solid is notably higher compared to, for example, p-DTS(PTTh$_2$)$_2$, in which the λ_{max} red shift is 55 nm. Solution cyclic voltammetry (CV) measurements indicate that the highest occupied molecular orbital (HOMO) and lowest unoccupied molecular orbital (LUMO) are -5.12 and -3.34 eV, respectively, corresponding to a band gap of 1.78 eV, in reasonable agreement with the optical band gap calculated from solution absorption onset.[32] These data suggest that the frontier molecular orbitals of p-DTS(FBTTh$_2$)$_2$ line up favorably with those of common fullerene acceptors to generate useful V_{OC} in BHJ solar cells.[33][34]
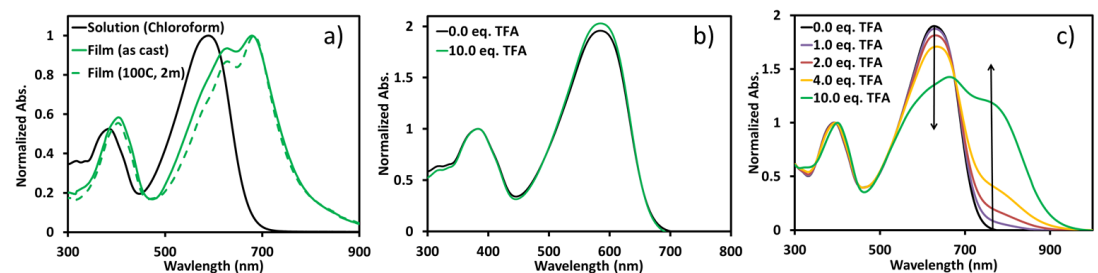
Figure 3.2. Absorption spectra of a)p-DTS(FBTTh₂)₂ solution in chloroform, thin film and annealed film, b) p-DTS(FBTTh₂)₂ and c) d-DTS(PTTh₂)₂ with various equivalents of trifluoroacetic acid in chloroform

To probe whether the design elements proved useful to reduce sensitivity toward protonation, the solution absorption profile of p-DTS(FBTTh₂)₂ was monitored as function of CF_3CO_2H concentration. Figure 3.2b shows that the absorption of p-DTS(FBTTh₂)₂ remains unchanged when in the presence of up to ten equivalents of CF_3CO_2H. By comparison, d-DTS(PTTh₂)₂ (here "d" denotes that the pyridyl N atoms point away from the interior DTS core, i.e. a distal regiochemistry) was subjected to the same conditions as a control. The resulting absorption profiles (Figure 3.2c) show significant changes immediately upon acid addition; namely one observes new low energy transitions suggesting that the chromophore backbone is influenced by the protonation. Notably, the effect does not saturate even up to ten equivalents of acid, indicating an equilibrium between protonated and non-protonated species in solution. These data indicate that p-DTS(FBTTh₂)₂ is more resilient against acidic conditions and argues in favor of using PEDOT:PSS interlayers in OPV devices.

3.3 Solar Cell Device Performance

Photovoltaic devices were fabricated using the general architecture: ITO/PEDOT:PSS/DTS(FBTTh₂)₂:PCBM/Ca/Al. Solutions were cast from a 3.5% w/v total blend concentration in chlorobenzene. A series of studies were conducted to explore

improvements in *PCE*. The influence of the p-DTS(FBTTh$_2$)$_2$:PCBM ratio was examined by looking at the following compositions: 40:60, 50:50, 60:40 and 70:30. Spin-rates ranging from 1000 rpm to 5000 rpm were also examined. Best devices from this examination had a p-DTS(FBTTh$_2$)$_2$:PCBM ratio of 60:40, as produced by spin coating at 1750 rpm; typical current-voltage characteristics and external quantum efficiency (*EQE)* plots are shown in Figure 3.3. These data show a *PCE* of 1.8%, with a V_{OC} of 780 mV, a short circuit current (J_{SC}) of 6.6 mA cm−2, and a FF of 0.36. Post-deposition annealing temperatures were then investigated on the films described above by looking at the effect of heating for 10 minutes within the temperature range of 70 to 150 °C. The best improvement was observed by heating at 130 °C: $V_{OC} = 0.82\,V, J_{SC} = 10.8\,mA/cm^2$, and $FF = 0.65$, yielding a *PCE* of 5.8%.
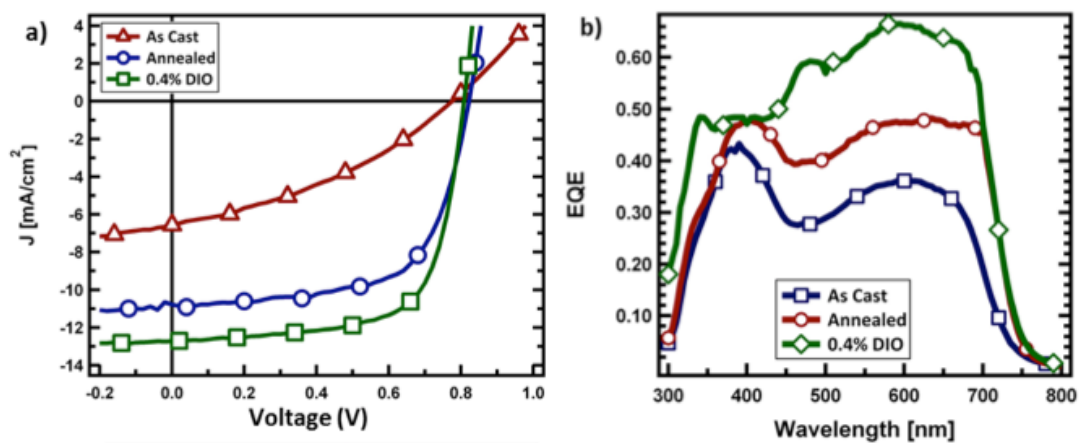
Figure 3.3. a) Current voltage characteristics of solar cells with an active layer comprised of p-DTS(FBTTh$_2$)$_2$ and PCBM as cast, annealed and with 0.4 % (v/v) diiodooctane solvent additive and b) corresponding external quantum efficiency plots

Further optimization involved using small quantities of diiodooctane (DIO) as a solvent additive during the film-casting step. The following DIO concentrations in chlorobenzene were used: 0.1, 0.15, 0.2, 0.25, 0.3, 0.35, 0.4, 0.5, 1.0 v/v%. One finds a progressive increase in *PCE* up to [DIO] = 0.4 v/v%, followed by a rapid deterioration of

device characteristics. Altogether, we find that by using [DIO] = 0.4 v/v%, followed by heating at 70 °C (in order to remove residual solvent and DIO), one can obtain a *PCE* of 7.0% ($V_{OC} = 0.81\,V$, $J_{SC} = 12.8\,VmA/cm^2$, and $FF = 0.68$), which at the time of publication, was the highest reported efficiency of a solution processed SM-BHJ solar cell to date.

3.3.1 Photocurrent Analysis

By plotting the photocurrent against the effective voltage, differences in charge generation and collection between the as cast, annealed, and optimized DIO conditions become evident. The effective voltage, that is the voltage at which no photocurrent is generated less the applied voltage, V_0–V, determines the strength of the electric field within the device and thus the driving force for charge extraction.[35] In the case of the 0.4% DIO and annealing conditions, the photocurrent quickly increases and then begins to plateau at relatively low effective voltages, ≈0.2 V; that is to say a very small driving force is needed for charge collection, suggesting good transport within the films and explaining the relatively high FF. In contrast, the photocurrent in as-cast devices does not begin to saturate, until an effective voltage of ≈4 V. The much stronger electric field required to sweep out photogenerated charges suggests relatively poor charge transport within these devices. This rationale will be examined in more detail to follow.
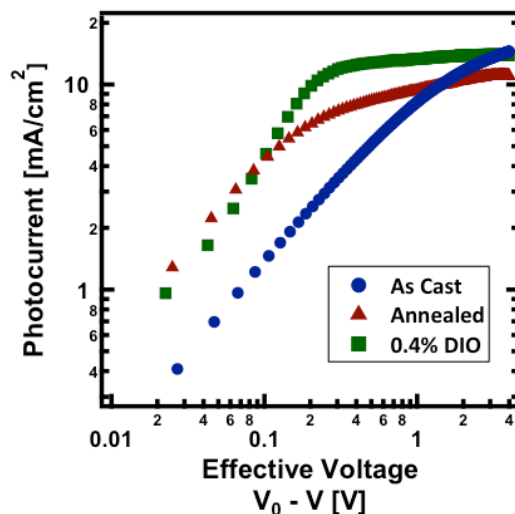
Figure 3.4. Photocurrent vs. effective voltage for three processing conditions: as cast (blue) thermally annealed at 130 °C (red) and with 0.4% DIO additive (green).

At sufficiently high electric fields, we expect to collect nearly all of the generated charges within a device due to the strong driving force for extraction.[35] Thus, comparing the photocurrents at high effective voltages offers insight into the differences in photogeneration as a function of internal structure. In both the optimum DIO processed and as-cast film, the photocurrent at 4 V is $\approx$16 mA cm^{-2}, suggesting that photogeneration rates are quite similar, despite obvious differences in performance. In the thermally annealed device, on the other hand, photocurrent saturates at $\approx$12 mA cm^{-2}. As these films are all of similar thickness, slight variations described in the film absorption cannot account for this substantial discrepancy in photocurrent. Rather, this is most likely evidence of a reduced photogeneration rate in the annealed film.

3.3.2 Photoluminescence

This observation is confirmed by photoluminescence spectroscopy shown in Figure 3.5. For all three films, the PL spectrum has a peak at 1.55 eV, consistent with singlet emission from p-DTS(FBTTh$_2$)$_2$ domains.[36]
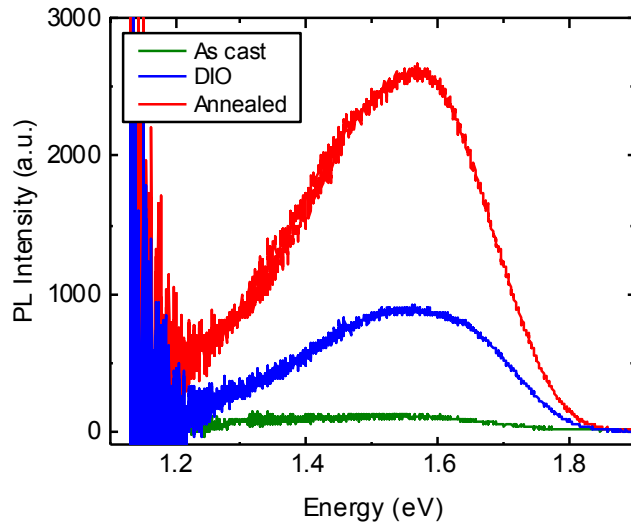
Figure 3.5. Photoluminescence for three film processing conditions: as cast (green) thermally annealed at 130 °C (red) and with 0.4% DIO additive (green).

The intensity of the emission varies greatly from film to film. In the as-cast film, nearly all PL is quenched. This suggests nearly all excitons reach an interface and dissociate. The DIO processed device does show some emission, however, not nearly to the extent of the annealed device. This suggests that some singlet excitons in the annealed device do not reach a donor acceptor interface and dissociate.

3.3.3 Internal Quantum Efficiency

From the *EQE* spectra in Figure 3.3b, the most important enhancement in the photocurrent occurs in the low energy region, attributed to excitons generated on p-DTS(FBTTh$_2$)$_2$.[37][38] To further quantify how efficient the charge generation and extraction processes are in the optimum devices, we have calculated the internal quantum efficiency (*IQE*) of the 0.4% DIO processed device. Following the technique described by McGehee and colleagues,[39] we determine the active layer absorption by subtracting the calculated

parasitic absorption (due to PEDOT:PSS, Al, etc.) from the total device absorption, measured using a spectrometer fitted with an integrating sphere, as shown in Figure 3.6.
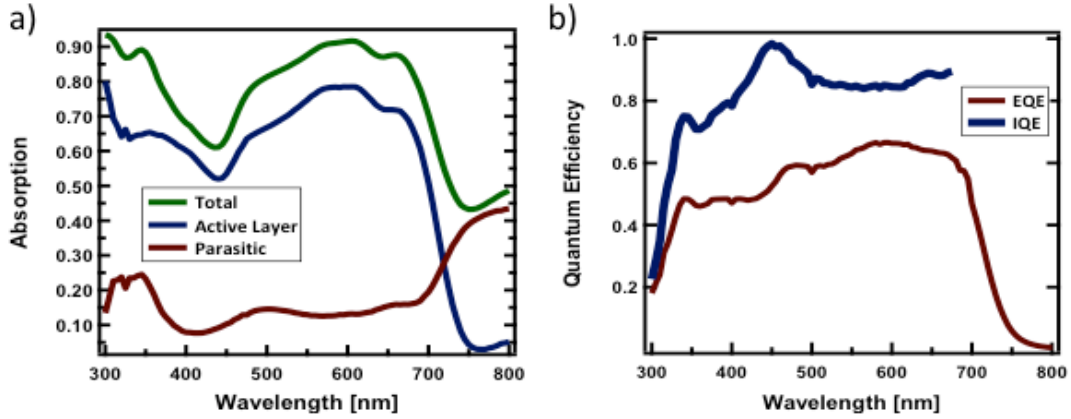
Figure 3.6. a) Total, parasitic, and active layer absorption of optimized device and b) internal quantum efficiency of optimized device.

Under the optimum conditions, we find that the *IQE* reaches nearly 100% for light at 445 nm and remains close to 90% efficient across the entire spectral range as seen in Figure 3.6b. Nearly all absorbed photons result in free charges, which are subsequently extracted, resulting in high short circuit current. Under ideal casting conditions, the device layer thickness was determined to be 100 ± 10 nm as measured by profilometry. While p-DTS(FBTTh$_2$)$_2$ has a relatively high optical density and covers a broad spectral range, solubility limitations prevent thicker film formation and thereby limit optical absorption of the active layer in devices. It can be seen in Figure 3.6a that the active layer never absorbs more than 80% of incident photons across the spectral range. This suggests that the J_{SC} in the optimum DIO processed devices is most limited by the absorption of the film rather than the charge generation or charge extraction processes.

38

3.4 Morphology Characterization

3.4.1 UV-Visible Absorption

The influence of processing conditions on film properties was first examined through UV-visible absorption spectroscopy (Figure 3.7). The absorption of p-DTS(FBTTh$_2$)$_2$ in chloroform gives a maximum (λ_{max}) at 615 nm and an absorption onset (λ_{onset}) at 680 nm. The value of λ_{onset} defines an optical bandgap of 1.8 eV. Thin films of neat p-DTS(FBTTh$_2$)$_2$ show a red-shift in absorption, with λ_{max} = 688 nm and λ_{onset} = 780 nm, corresponding to a 1.5 eV bandgap. The appearance of vibronic structure at 688 nm and the red-shift in λ_{onset} of 100 nm suggests good molecular ordering within the film as was discussed for the neat film.[40][41]
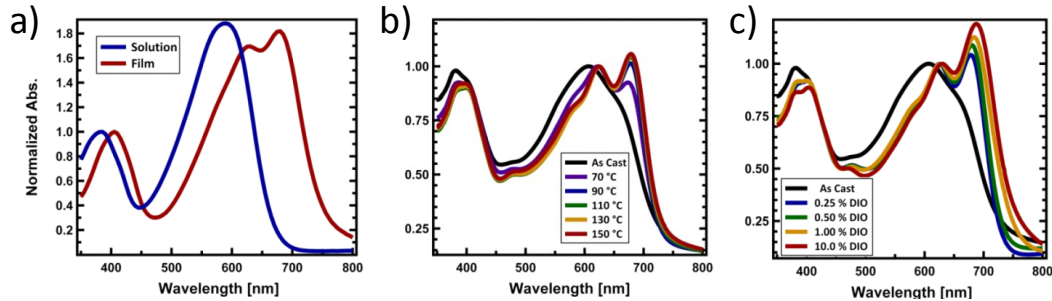
Figure 3.7. UV-visible absorption spectra of the (a) neat p-DTS(FBTTh$_2$)$_2$ solution and film (b) BHJ annealed films and (c) BHJ films processed with DIO all cast on PEDOT:PSS coated ITO substrates.

When p-DTS(FBTTh$_2$)$_2$ is cast from a blend with PCBM, (Figure 3.7b, black) λ_{max} (620 nm) is similar to what is observed in solution. This feature, in combination with the loss in vibronic structure, suggests that PCBM serves to break up some of the solid-state ordering seen in neat p-DTS(FBTTh$_2$)$_2$. As shown in Figure 3.7b, the vibronic structure reappears upon thermal annealing and becomes more pronounced with increasing temperature. We can surmise at this point that thermal annealing allows intermolecular

motion within the film such that the molecular components can more readily achieve better organization.[7]

Films cast from solutions containing DIO exhibit similar phenomenology as those that undergo thermal treatment (Figure 3.7c). Just 0.25% additive by volume results in the reemergence of a vibronic peak at 670 nm, which, as described previously, is not evident in the blend cast from pure chlorobenzene. Subsequently, there is a clear, progressive increase in intensity of the vibronic peak and a red-shift of λ_{onset} as DIO increases up to 10%. Addition of large amounts of DIO yields slightly thinner films, so the spectra in Figure 1 are normalized to the peak at 625 nm to more clearly highlight the progression in vibronic structure.

3.4.2 Transmission Electron Microscopy

We note that films of p-DTS(FBTTh$_2$)$_2$ and PCBM formed smooth films when cast atop PEDOT:PSS, with rms < 2.0 nm, as confirmed by atomic force microscopy. While annealing and solvent additives lead to some structure visible in the surface topography, all the films are relatively smooth. We employed transmission electron microscopy (TEM) to understand the origin of the observed changes in optical properties upon thermal treatment or use of solvent additive, and the nature of the molecular order suggested by the UV-visible spectra. Films were prepared for TEM in the same fashion as devices, atop PEDOT:PSS coated glass, however the PEDOT:PSS layer was not annealed and no cathode was deposited. The films were then scored and floated off of the substrate in deionized water and collected on a copper mesh grid coated with ultra-thin carbon coating. Low-resolution bright field images were taken on a FEI Tecnai G2 Sphera microscope operating at 200 kV. For good contrast, relatively long exposure times of 10–30 s were needed under low defocus

conditions. As seen in Figure 3.8 the as-cast film shows almost no discernible structure, even at relatively large defocus values and various exposure conditions. Thus, when cast from chlorobenzene, p-DTS(FBTTh$_2$)$_2$ and PCBM seem to be well mixed, with no significant crystallization or phase separation observable. When these films are annealed, however, one observes wire-like structures that propagate throughout the film with characteristic widths of 40–50 nm and lengths of hundreds of nanometers. These domains are assigned as regions of p-DTS(FBTTh$_2$)$_2$ within the BHJ based on their high relative intensity (bright regions) compared to the surrounding film.[42] In addition, there appear to be larger scale phase fluctuations evidenced by the variations in contrast across the film, while any smaller scale structures that may exist between the wires lack significant contrast.
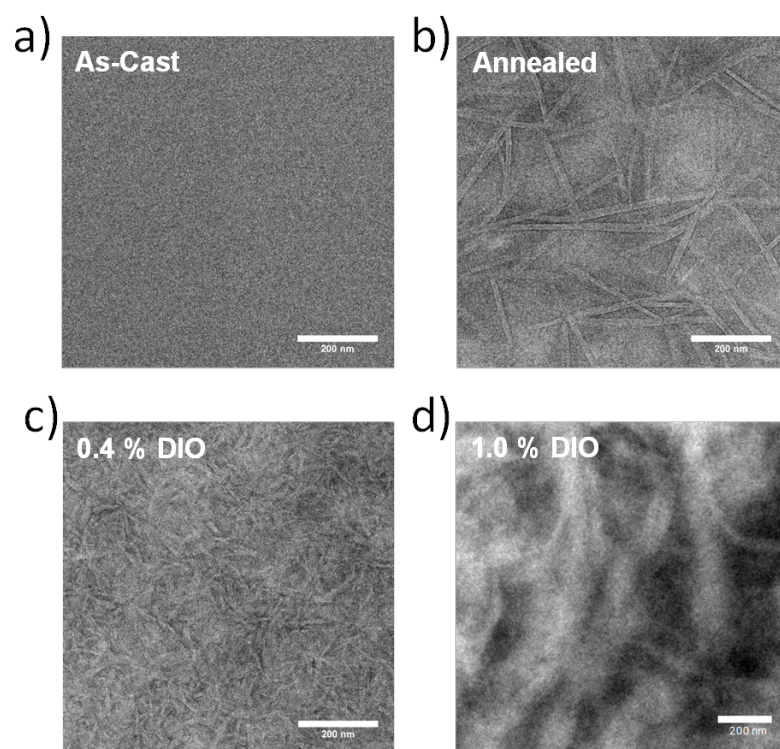
Figure 3.8. Bright field TEM images of p-DTS(FBTTh$_2$)$_2$:PCBM films (a) as-cast from chlorobenzene, (b) thermally annealed at 130 °C, (c) cast from 0.4% DIO, and (d) from 1.0% DIO. Scale bars all correspond to 200 nm.

A different picture is observed in the film processed with 0.4% DIO. Smaller p-DTS(FBTTh$_2$)$_2$ domains are visible with good contrast compared to the surrounding. These grains have a characteristic size of about 30–40 nm and seem to form a continuous network throughout the film (Figure 3.8c). While the use of large values of defocus to induce contrast in organic films can introduce small-scale features into an image which do not correspond directly with microstructure,[43] the structures seen in Figure 3.8 remain apparent and unchanged across all levels of defocus as shown in Figure 3.9, helping to confirm the features are morphological, and not a consequence of imaging.
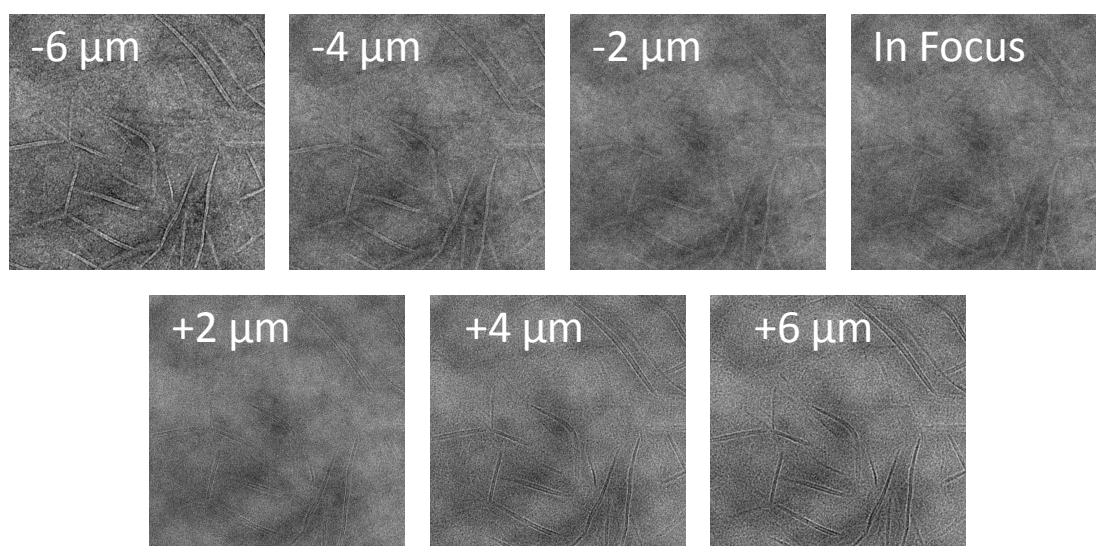
Figure 3.9. Bright field TEM images of annealed p-DTS(FBTTh$_2$)$_2$: PCBM film imaged at (from left to right, top then bottom) d = -6, -4, -2, 0, +2, +4, +6 µm defocus, where a negative value denotes underfocus.

In films formed from 1% DIO solutions, conditions that lead to deterioration of *PCE* to less than 1% (Figure 3.10a) much larger scale wires are formed (Figure 3.8d, 3.10b). The wires have widths close to 100 nm and can be up to microns long. A large-scale perspective of the wires, is shown in Figure 3.10b. While 0.4% DIO helps induce a network of small

grains of p-DTS(FBTTh$_2$)$_2$, too much DIO results in significantly larger p-DTS(FBTTh$_2$)$_2$ domains.
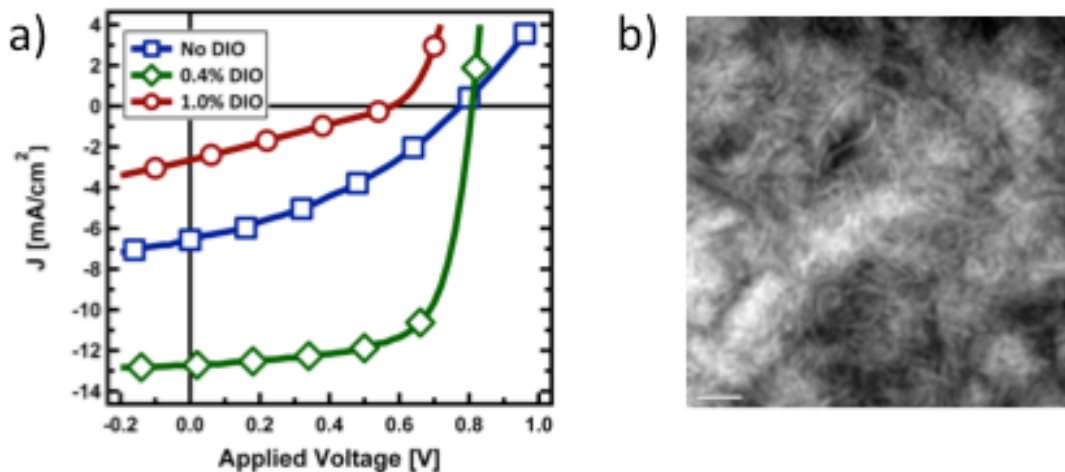
Figure 3.10. a) JV characteristics of P-DTS(FBTTH$_2$)$_2$:PCBM devices processed with three additive concentrations, 0% (blue) 0.4% (green) and 1.0% DIO by volume (red) (Device performance of 1.0% processed device: J_{SC} = 2.41 mA cm^{-1}, V_{OC} = 550 mV, FF = 0.31, PCE = 0.40%) and b) Low magnification bright field TEM image of 1.0% DIO processed p-DTS(FBTTh$_2$)$_2$:PCBM film imaged at 5 μm defocus and 20 s exposure. Scale bar corresponds to 1 μm.

Further insight into the morphology can be gained through low-dose, high-resolution TEM. High-resolution images were taken on a FEI Titan FEG microscope, using C-Flat Carbon holey carbon grids for stability. To achieve high-resolution images, a low-dose imaging procedure was applied in which the sample was allowed to mechanically stabilize. A 1.0 μm defocus was applied to focus on the in-plane stacking within the film. The beam was then shifted electronically off of the optical axis to an undamaged area of the film for imaging. Using a 10 μm aperture, exposure times of 4 s were used to achieve images with average signals of 50–200 counts. By adjusting the contrast transfer function through a small defocus, it is possible to directly image crystal lattice fringes within the film. This technique helps to understand the nature of crystallinity within the morphology seen using traditional bright field TEM. The crystals are highly sensitive to the electron beam, so care needs to be

taken to minimize the dosage and avoid degradation. Images are obtained at an exposure time of 4 s, approximately one third of the exposure time necessary for the fringes to completely disappear.
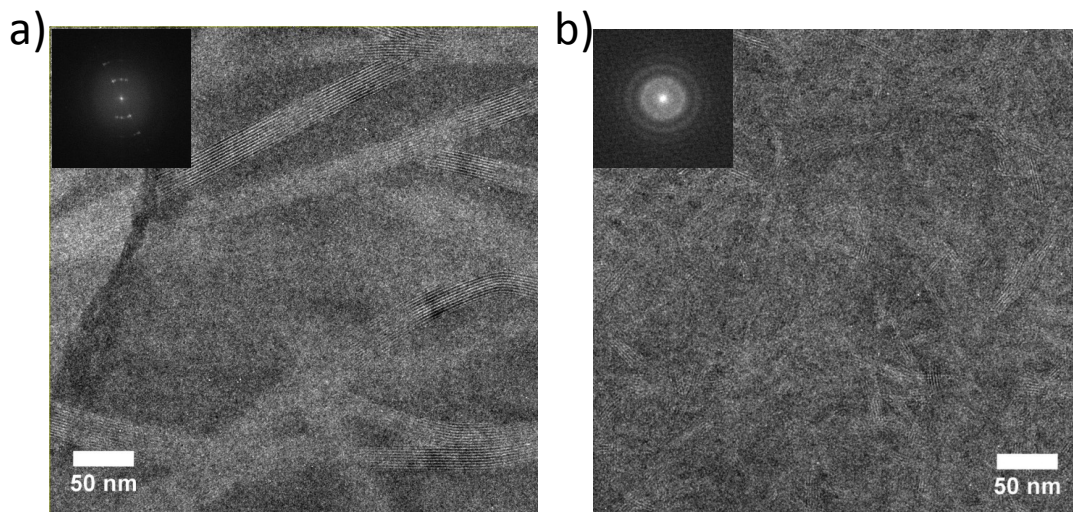
Figure 3.11. High-resolution TEM images of p-DTS(FBTTh$_2$)$_2$:PCBM films showing lattice fringes (0.3 A^{-1}) from in-plane stacking of the p-DTS(FBTTh$_2$)$_2$ phase in a) thermally annealed, and b) 0.4% DIO processed BHJ films. Fourier transforms of images are provided in the insets.

From Figure 3.11a, there is a clear correlation between the direction of the observed wires and the imaged lattice spacings in the thermally annealed blend film. Fringes run along the length of the wires, corresponding to repeating 2.2 nm lattice planes across the width of the wires. It is also worth noting that additional lattice fringes with 1.6 nm spacing are visible in some of the images taken, in the areas between the wires Figure 3.12. This crystal population likely leads to some of the observed diffraction contrast in the high-resolution TEM images. However, these crystallites are particularly sensitive to electron beam damage, and disappear within a few hundred counts, making the extent of this crystal population difficult to quantify.
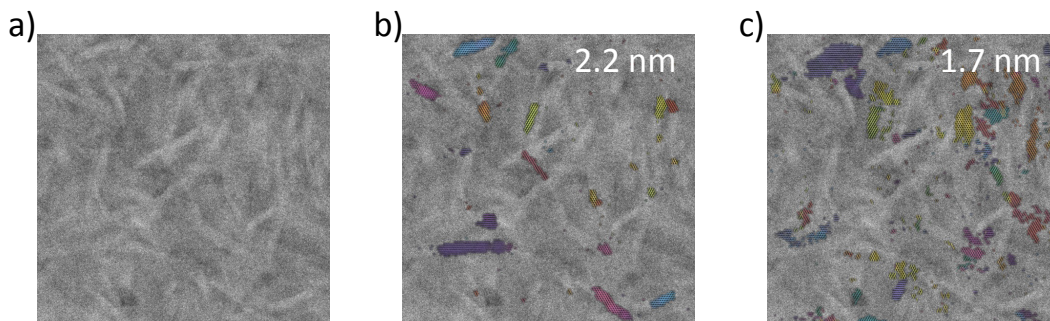
Figure 3.12. a) High-resolution TEM images of pure P-DTS(FBTTH₂)₂ film annealed at 130 °C highlighting (b) 2.2 nm lattice fringes from alkyl stacking and (c) 1.6 nm lattice fringes from hexyl stacking. The colors and directions of the crosshatches correspond to the direction of the fringes as determined via the methods described in ref 12. All images are 656 nm per side.

The structures in the optimum 0.4% DIO processed film Figure 3.11b are not nearly as well resolved or as coherent as in the annealed film. The same 2.2 nm spacing can be observed throughout the film, although the imaged crystalline domains are much smaller. The lattices form much shorter wires, making grain-like structures reminiscent of those seen by conventional TEM. This gives a good indication that the features seen in bright field TEM are due to crystalline p-DTS(FBTTh₂)₂.

One drawback of high-resolution TEM is that it is not sensitive to all orientations of crystals within the film; only lattices normal to the electron beam can be imaged.[15] The resultant image is a projection of the crystallites throughout the film, which lie in-plane. Cross-sectional TEM was employed to examine the three dimensional nature of the BHJ morphology.[17][44][45][46][47] A focused ion beam (FIB) was used to mill out a TEM lamellar, and using an Omni probe system, attach it to a TEM grid. The sample was then further thinned to a thickness of approximately 75 nm in multiple etching steps working at a low voltage and using progressively lower operating currents. Particular care was taken to not expose the sample to any unnecessary dose of either the ion or electron beams to reduce the

amount of FIB damage and implantation as much as possible, as these can cause difficulty in the interpretation of cross-sectional samples. [48]

Rather than looking at the as-cast, annealed, and solvent additive conditions separately, all three BHJ films were deposited on top of each other in a stacked manner. The utility of such a stacked configuration, beyond allowing the simultaneous preparation and imaging of all three systems of interest at once, is reduction in the ambiguity that might result from thickness variations, ion beam damage, or gallium implantation.[46] Any artifacts visible in one layer should also be present and equal in each of the other layers. In order to fabricate such samples, films were prepared successively with thin titanium oxide layer spacers.[47] Before casting the successive BHJ layers, relatively thick layers of PEDOT:PSS were applied to each titanium oxide layer to create a nearly equivalent architecture to that found in working devices. Samples for cross-section analysis were prepared atop a silicon substrate with a 200 nm oxide coating. The annealed bulk heterojunction was deposited as in devices atop PEDOT:PSS and annealed at 130 °C for 10 min in an inert atmosphere. A 30 nm TiOx layer was then deposited from an ethanol solution as described, and annealed at 70 °C for 10 min in air. Two successive layers of PEDOT:PSS were then deposited and annealed in air at 70 °C for 10 min each. The additive processed film was then cast and annealed at 70 °C as in devices. Again, a TiOx layer was deposited and annealed in air, two layers of PEDOT:PSS deposited, the final BHJ film cast, and 100 nm of aluminum deposited on top. The sample was prepared as described in Chapter 2.9. It bears noting that the order in which the BHJ films are deposited was chosen due to the thermal requirements of each film, as any annealing steps affect all of the deposited layers. Thus, the first layer was annealed prior to subsequent layer depositions.

The results from the cross-sectional TEM studies are shown in Figure 3.13. Differences between the three film structures can be easily observed. The wire-type structures seen in the top-down images of the annealed film, that is, Figures 3b,4a, are also present in the cross-section. These wires do not seem to have a preferential orientation, but rather propagate throughout the film oscillating vertically. We also bring attention to what seems to be a coating of p-DTS(FBTTh$_2$)$_2$ directly atop the PEDOT:PSS layer in the annealed film that covers the entire width of the slice. While we cannot draw conclusions about the extent of this layer from such a small fraction of the film, it was seen independently in two different FIB cross sectional images.
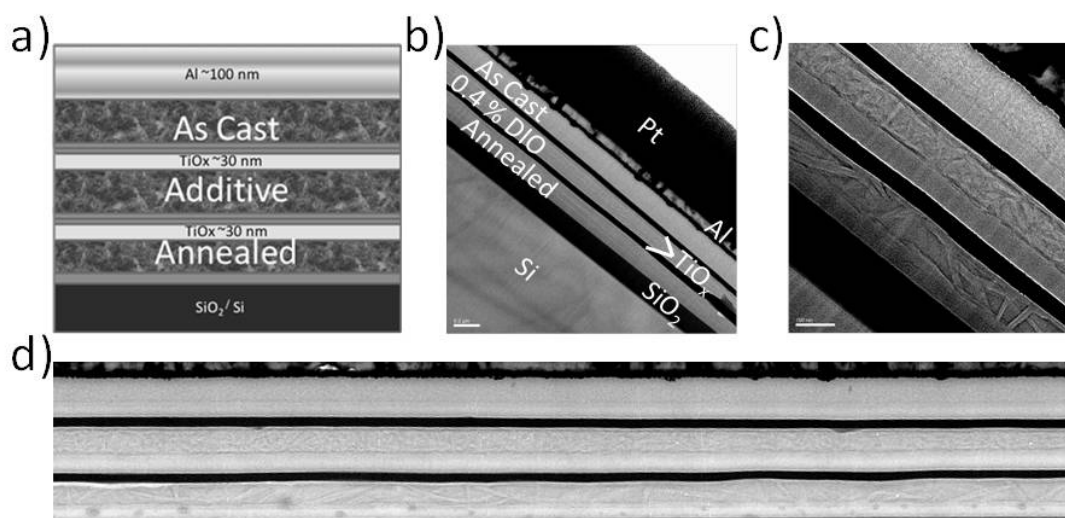
Figure 3.13. a) Cartoon schematic of multilayer stack, b) cross-sectional TEM of multilayer stack at 7 μm defocus showing stack architecture, c) small section of a stack at 7 μm defocus, and d) multilayer sample from stitched images at 5 μm defocus.

Although the network within the p-DTS(FBTTh$_2$)$_2$:PCBM film processed with 0.4% DIO is not as easy to discern as the wire structures in the thermally annealed film, it again correlates well with the top-down images in Figures 3c,4b. This particular p-DTS(FBTTh$_2$)$_2$:PCBM blend exhibits finer-scale phase separation than in the annealed film.

The "rice-grain" structure seen in-plane in the top down TEM seems to extend vertically as well. The lack of discernible structure within the as-cast layer of the stack is further evidence that the materials are well blended when cast from chlorobenzene alone.

3.4.3 X-Ray Scattering

One of the promising features of discrete molecular systems, such as p-DTS(FBTTh$_2$)$_2$, compared to conjugated polymer counterparts is the possibility to obtain a complete picture of the distance and orientation between the optoelectronic units in the solid state via single crystal X-ray diffraction studies. Indeed, it was possible to grow suitable single crystals of p-DTS(FBTTh$_2$)$_2$ from a chloroform solution through vapor diffusion of hexane. The resulting crystal possesses a triclinic system with two molecules assigned to a unit cell, as shown in Figure 3.14. The conjugated backbone remains planar, with almost no twisting. Such a flat conformation enables intramolecular interaction between the electron-poor fluorinated benzothiadiazole (FBT) moieties and the electron-rich silyldithiophene (SDT) and bithiophene moieties, and extends the molecule's conjugation length. Besides the intramolecular conformation, p-DTS(FBTTh$_2$)$_2$ packs in a slip-stack fashion (Figure 3.14c) forming a two-dimensional columnar array, which is favorable for intermolecular charge transport,[49][50] as opposed to the "herringbone" packing commonly observed in many conjugated small molecules such as oligothiophenes,[51] and diketopyrrolopyrrole derivatives.[52][53]
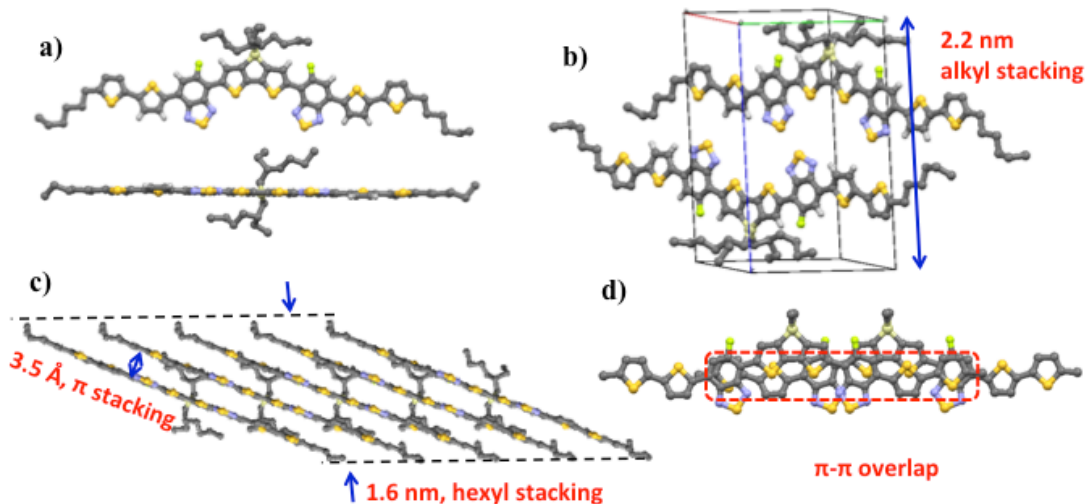
Figure 3.14. a) Molecular conformation of p-DTS(FBTTh$_2$)$_2$ with C, N, S and F atoms shown in grey, blue, yellow, and green respectively b) Unit cell showing 2.2 nm alkyl spacing c) viewed down (1,4,1) plane highlighting π-stacking and hexyl stacking d) Intermolecular π-conjugated backbone overlap of adjacent molecules, viewed perpendicular to the plane of the conjugated backbones. Alkyl chains (2-ethylhexyl) are simplified as methyl groups for clarity

Intermolecular overlap of conjugated backbones geometrically provides the capacity for π-orbital interaction, critical for charge carrier hopping during transport.[54] Many conjugated molecules only show overlap at their end-groups or the edge of the conjugated backbone, leading to a small area with direct π–π overlap. A superior π–π overlapping area is observed between two adjacent p-DTS(FBTTh$_2$)$_2$ molecules as shown in Figure 3.14d (as highlighted by the red rectangle) in which nearly the entire conjugated backbone, including the DTS core, FBT units and two of the four thienyl units, have direct overlap with neighboring molecules. This overlap, intrinsic to the solid state arrangement of p-DTS(FBTTh$_2$)$_2$, may have merit for effective charge transport.

Since single crystal growth is an inherently different process than casting a thin film, grazing incidence wide-angle X-ray scattering was used to probe the crystallites within the thin film (Figure 3.15). The diffraction pattern was indexed according to the obtained crystal structure and the good correlation supports that the single crystal and crystallites within the

spin coated thin film are of the same polymorph. The π-stacking within the crystal has a distance of 3.5 Å between two adjacent conjugated backbones that can be described by the (141) plane. In the out of plane direction (polar angle = 0 °), the most prominent reflections occur at 2.7, 5.4, and 8.1 nm^{-1}. These correspond to the (001), (002) and (003) planes, respectively. These reflections are due to the 2.2 nm spacing associated with the alkyl stacking of p-DTS(FBTTh$_2$)$_2$. The presence of higher order reflections and the narrow distribution of the alkyl stacking peak across the polar angle indicates that p-DTS(FBTTh$_2$)$_2$ preferentially orders with vertical alkyl stacking within the film. This corresponds well with the size of the spacing imaged via high resolution TEM. Additionally there is a peak in plane at 4.0 nm^{-1}, corresponding to a spacing of 1.6 nm, which we identify as the hexyl stacking peak. This may be attributed to the second, more sensitive crystal population found in the some of the TEM images.
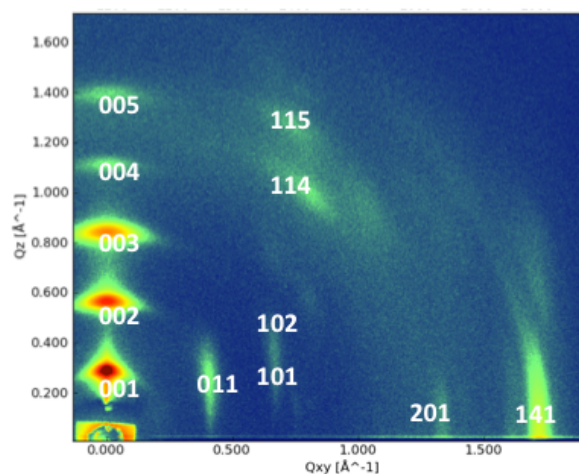
Figure 3.15. GIWAXS plot of neat p-DTS(FBTTh$_2$)$_2$ film annealed at 130°

This provides a very clear picture as to the preferential crystallization orientation of pure p-DTS(FBTTh$_2$)$_2$, in which the ethyl hexyl chains are oriented vertically and the conjugated backbones form layers in plane with the substrate. To help quantify the degree of

crystallization, from the breadth of the (002) reflection, the crystal correlation length (CCL) was calculated to be 20 nm using the Scherrer equation. The CCL is a measure of the size and/or perfection of a crystallite.
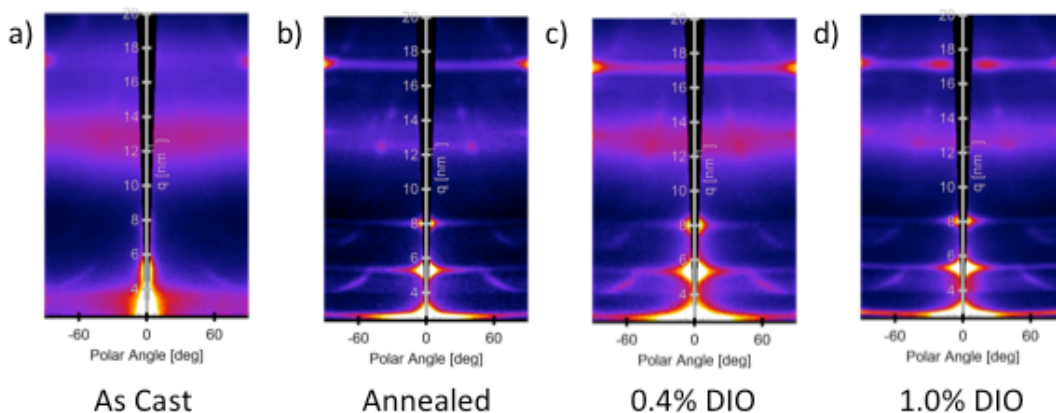
Figure 3.16 GIWAXS sector plots for BHJ blends, a) as cast b) annealed at 130° c) cast with 0.4 %DIO and d) cast with 1.0% DIO all on Si/PEDOT substrates

Blend films identical to those studied in devices were also analyzed to determine how PCBM affects the self-assembly of p-DTS(FBTTh$_2$)$_2$. In an as-cast p-DTS(FBTTh$_2$)$_2$/PCBM BHJ blend (Figure 3.16a) few p-DTS(FBTTh$_2$)$_2$ reflections are apparent above the background scattering of the sample and the CCL is 7.5 nm. The washing out of p-DTS(FBTTh$_2$)$_2$ reflections and reduction in its CCL when compared to neat films indicates that PCBM interferes with the self-assembly and crystallization of p-DTS(FBTTh$_2$)$_2$ during casting, consistent with observations from the absorption experiments. Annealing the BHJ blend, (Fig 3.16b) however, increases the CCL to 16.3 nm and restores the higher order out of plane reflections. Annealing therefore increases the size and/or perfection of p-DTS(FBTTh$_2$)$_2$ crystals when blended with PCBM, but not to the extent that exist in annealed neat p-DTS(FBTTh$_2$)$_2$ films. This is consistent with the reemergence of vibronic structure in the absorption spectra upon annealing. In each blend a

broad, isotropic feature centered at approximately 13 nm^{-1} exists which we assign to amorphous PCBM.

The processing additive DIO also causes p-DTS(FBTTh$_2$)$_2$ to crystallize when added to BHJ blend solutions. When 0.4 vol. % (optimum concentration) DIO is used, p-DTS(FBTTh$_2$)$_2$'s CCL is 11.4 nm (Figure 3.16c). In the absorption experiments, it was clear that use of additional DIO resulted in further increases in vibronic structure and red shifting of the absorption onset. Using 1.0 vol % DIO further increases the CCL found in GIWAXS to 16.3 nm (Figure 3.16d). Thus the GIWAXS spectra support the same conclusion; the extent of order within the film can be controlled through DIO concentration. Furthermore, it is clear that the spacings and orientations in the blend films are consistent both with those seen in the pure p-DTS(FBTTh$_2$)$_2$ film, and with each other. This indicates the type of crystallization in each BHJ is very much the same, and the differences are only due to size and perfection of the crystals within the film.

In a bulk heterojunction, there are multiple length scales relevant to device performance. While GIWAXS probes molecular spacings (crystallization) it does not indicate the extent of larger scale phase separation associated with the BHJ structure. Using grazing incidence small angle x-ray scattering (GISAXS) we can probe smaller values of q in the range of 0.004 – 0.1 A^{-1} (Figure 3.17). These values of q-space correspond to the size of domains (10-150 nm) typically associated with phase separation in a BHJ solar cell.
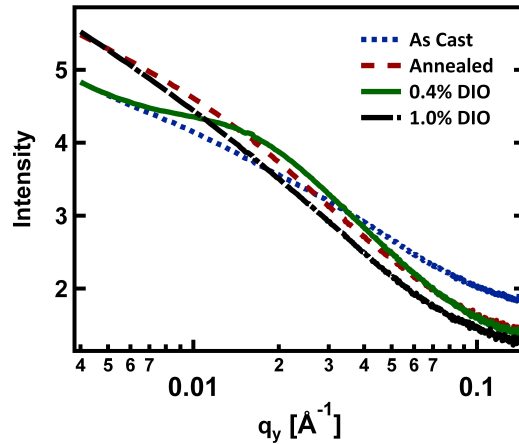
Figure 3.17. GISAXS plots of BHJ films cast on Si/PEDOT substrates

The linear relationship between intensity on a logarithmic scale and q on a logarithmic scale seen for the as-cast blend indicates the absence of any features of a distinct size in the 5-150 nm range in real space. The blend film processed with 0.4% DIO on the other hand, shows a very distinctive bend or "Guinier knee" centered close to 0.02 A^{-1} indicating a characteristic domain size of approximately 30 nm within the film. There is a very slight bend in the trace from the annealed film potentially suggesting domains of ~50 nm in size, though it is very slight and not well defined. The trace from the film processed with 1.0% DIO also appears nearly linear, though the slight curve at higher q values indicates there may exist features beyond the length scales probed by this experiment. This demonstrates that concomitant with the increase in the size and/or perfection of p-DTS(FBTTh$_2$)$_2$ crystallites seen with GIWAXS the length scale of p-DTS(FBTTh$_2$)$_2$/PCBM phase separation increases upon annealing or addition of DIO as well. These results are quite consistent with what was identified by TEM.

3.5 Charge Transport

With a deeper understanding of the film morphology, it is useful to examine more closely the transport properties of these devices, which were suggested to play a large role in the solar cell properties. One of the fundamental requirements of donor materials for OPV devices is the ability to effectively transport holes. To measure mobility, while most accurately mimicking transport in a solar cell, we fabricate hole selective diodes, which as opposed to field effect transistors, have charge densities comparable with solar cells and have the same vertical architecture. In order to facilitate Ohmic injection into the HOMO energy level of p-DTS(FBTTh$_2$)$_2$, hole-only diodes of the neat material with a PEDOT:PSS bottom contact, and a Au top contact were fabricated.

The obtained current-voltage characteristic shows clear space charge behavior following the Mott-Gurney relation,

$$J = \frac{9}{8} \varepsilon_r \varepsilon_0 \mu \frac{(V - V_{bi})^2}{L^3},$$

where ε_0 is the vacuum permeability, ε_r is the dielectric constant (assumed to be 3), L the active layer thickness, V is the applied voltage, V_{bi} the build in voltage and μ the zero field hole mobility. A fit to the data in Figure 3.18 results in a hole mobility for neat p-DTS(FBTTh$_2$)$_2$ of 5x10^{-4} cm^2/Vs. The temperature scan of the device current reveals an activation energy of 0.25 eV, consistent with the universal activation energy-mobility relation proposed by Craciun et al.
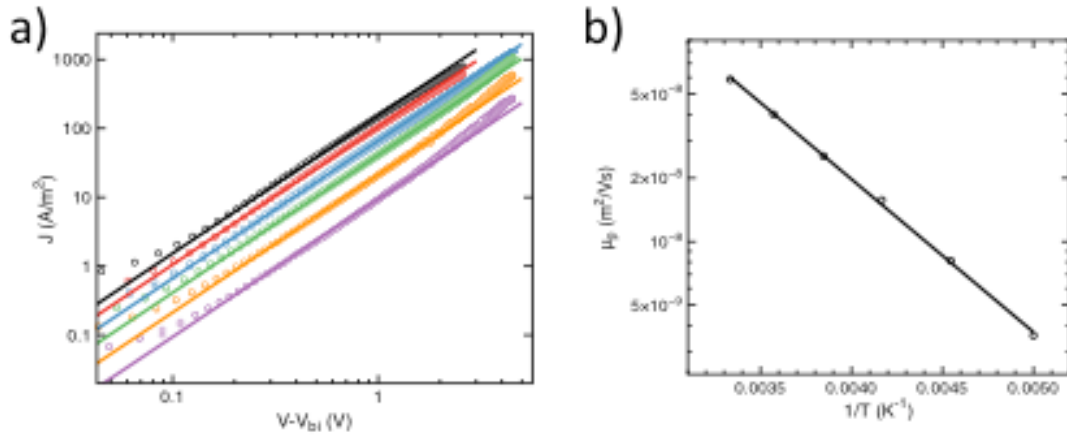
Figure 3.18. a) Temperature Dependent JV Characteristics of p-DTS(FBTTH$_2$)$_2$ Hole Only Diode and b) Extracted Mobilities

It is worth noting that in order to determine accurate mobilities from current-voltage measurement a number of prerequisite conditions must be met. The active layer should be sufficiently thick, eliminating contact effects, which can increase density , and give rise to increased mobility in thin layers. Additionally, thin layers can cloak possible charge trapping effects as a consequence of the rather high density in the active layers. Finally, thick layers will simply allow a more accurate fit of the Mott-Gurney relation to the data since the voltage range for the fit is larger and decreases the possible error due to asymptotic nature of a $1/L^3$ dependence. The obtained zero field mobility should ideally also follow this third power dependence on thickness. However, forming thick layers can be particularly challenging for solution-processable small molecules, as they do not impart to solutions the same increases in viscosity as polymers at the same concentrations. Thus validating the third power dependence is inherently difficult, complicated by the finding that thicker films of p-DTS(FBTTh$_2$)$_2$ are rather rough, (RMS = 20 nm), and so a highly precise determination of the thickness is impossible. The characteristics in Figure 3.18 are of the maximum obtainable thickness for a p-DTS(FBTTh$_2$)$_2$ layer of 230 nm.

In general carrier transport has a percolative behavior where the individual carrier transport mechanisms are heavily influenced by the ratio and morphology in the blend and thus a high hole mobility in the neat film does not indicate the mobility in the blend. A first glance into the magnitude of the transport in organic solar cells is simply by analyzing the dark current of these solar cells. The dark current of organic solar cells is governed by a recombination process that is similar to that in the OLED operation. Holes are injected at the PEDOT:PSS anode and electrons are injected at the Ca/Al cathode where the recombination, often emissive from the charge transfers state, will take place at the donor/acceptor interface. Provided the contacts are chosen to be Ohmic with the frontier molecular orbitals of the donor and acceptor, this implies that this non-geminate recombination process of free carriers exactly follows the bimolecular Langevin-type recombination description. The Langevin recombination strength follows the relation,

$$k_L = \frac{q}{\varepsilon}\left(\mu_p + \mu_n\right),$$

where q is the elementary charge, μ_p is the hole mobility and μ_n is the electron mobility. It can be understood from this equation that for the dark current the fastest carrier in the equation dictates the bimolecular recombination, which for organic solar cells is often the electron mobility of the fullerene in the blend.

The dark currents are shown in Figure 3.19a depicts space charge fits to the dark current of the solar cells for the three conditions. For blends, all analyses were done on films prepared identically to solar cells, and thus are all of thickness ~100 nm, inducing some imprecision to the measurement. For all three conditions the obtained dark current mobility, μ_D is between 2×10^{-4} and 5×10^{-4} cm^2/Vs, close to the hole mobility of neat p-

DTS(FBTTh$_2$)$_2$ and about a factor 2 lower then the electron mobility of neat PCBM, as can be seen from Table 3.1.

Table 3.1. Charge Mobilities in Neat and Blend Films

	μ_p (cm^2/Vs)	μ_n (cm^2/Vs)	μ_D (cm^2/Vs)
Neat p-DTS(FBTTh$_2$)$_2$	5x10^{-4}	-	-
Neat PCBM	-	1x10^{-3}	-
As-cast	1x10^{-5}	5x10^{-4}	5x10^{-4}
Annealed	2x10^{-4}	6x10^{-4}	2x10^{-4}
DIO	5x10^{-4}	5x10^{-4}	5x10^{-4}

In many cases, in dark current analysis we can assume the fastest charges are electrons in the PCBM phase, however the high hole mobility of neat p-DTS(FBTTh$_2$)$_2$ makes this more ambiguous. Unfortunately then, little can be concluded yet as this technique does not give the identity of the fastest charge carrier nor an understanding of if the charge mobilities are balanced. The as-cast and DIO processing conditions give nearly identical results, so this alone cannot explain the large differences in solar cell performance.

To further probe charge transport in the blends, electron transport was examined by producing electron selective devices following the recipe proposed by Neher et al. Traditionally bare Al on glass is used as the bottom hole blocking contact for an electron only device. However, likely due to the crystallinity of the blend, the film does not wet on such a surface. Hence, the glass substrate is pre-spin-coated with PEDOT:PSS before the Al bottom contact is applied. After the active layer is topped with a Ca/Al contact the current-voltage characteristics of these devices also show clear quadratic behavior, Figure 3.19c, which leads to the anticipated electron mobilities in the blend (Table 3.1). Specifically, we

see that electron mobility in all three of the blends is good, with mobilities 5-6 x10^{-4} cm^2/Vs. This matches very well with the dark current mobilities so we can likely assign the fastest carriers as electrons in the PCBM phase, consistent with most other systems. Again interestingly, the differences in mobilities between the three conditions are negligible. It is worth clarifying that the deviation of the space charge fits at low currents is due to parasitical leakage currents and the deviation at high currents is due to the series resistance of the contact materials.
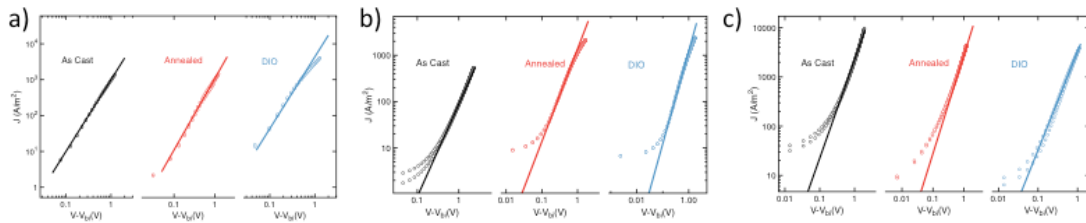
Figure 3.19. JV Characteristics a) hole only, b) electron only, and c) double carrier diodes of p-DTS(FBTTH$_2$)$_2$:PCBM blends as cast (black) annealed (red) and with 0.4% DIO (blue)

For the complete picture, hole selective diodes were also fabricated. The hole mobility of the as-cast device, μ_p = 1x10^{-5} cm^2/Vs (Table3.1) is more then an order of magnitude lower then the mobility neat p-DTS(FBTTh$_2$)$_2$ and the mobility deduced from the dark current. The hole mobility in the as-cast blend is likely hindered due to the lack of phase separation and crystal formation as seen by TEM. In the more crystalline blends that are annealed or cast with DIO, with larger phase, the mobility increases back close to the neat value. This is consistent with the increased *FF*s in these devices, and subsequent *PCE* compared with devices left as cast. The lower hole mobility with respect to the electron mobility for the as-cast device likely contributes to the increase in non-geminate recombination lowering the *FF* and *Jsc*. Since in both the annealed and the DIO devices the

mobilities are balanced as suggested by photoluminescence measurements, it is likely that geminate recombination lies at the origin of the J_{sc} difference.

Thus far we have demonstrated that when p-DTS(FBTTh$_2$)$_2$ is in a well mixed blend with PCBM, it has significantly reduced hole mobility, while inducing crystallization results in a hole mobility in the blend more consistent with neat p-DTS(FBTTh$_2$)$_2$. This is perhaps not surprising; crystalline features on the 30-50 nm length scale have a significant influence on transport through films of 100 nm thickness. But perhaps the more interesting question to ask then is if these wire like crystals influence the nature of the recombination mechanisms as well, and to what extent.

3.6 Recombination

Where recombination in gases is isotropic, the transport, and thus recombination, in organic materials is shown to be of a percolative nature leading to a filamentary transport structure with differences in local current densities that can vary over many orders of magnitude. Inconsistencies in the active layer that arise from common film preparation methods such as spin-coating may also contribute to predicted perturbations of Langevin type recombination. Hence a reduction of the recombination strength based on the Langevin expression is often observed for organic solar cells and defined as a prefactor, γ_{pre}. While many traditional polymer systems such as MEHPPV follow Langevin recombination with a small reduction factor, $\gamma_{pre} = 0.3$, others such as the archetypical P3HT:PCBM show reduction of $\gamma_{pre} = 0.001$ corresponding to a factor of 1000 reduction in recombination.

Recent work by Wetzelaer *et* al. has presented the possibility of calculating the Langevin reduction factor based exclusively on the dark, hole and electron current of an organic solar cell. This work is based on the assumption that the dark current is a

combination of the limiting cases of slow recombination, injected plasma limit, and infinitely strong recombination, two single carrier diodes in series, which results in the expression for the Langevin reduction factor,

$$\gamma_{\text{pre}} = \frac{16\pi}{9} \frac{\mu_p \mu_n}{\mu_{\text{eff}}^2 - (\mu_p + \mu_n)^2},$$

where μ_{eff} is the dark current mobility, μ_p the hole mobility and μ_n the electron mobility. From the results of the mobility studies (Table 3.1), the as-cast, annealed and DIO devices do not show reduced recombination. It is worth nothing that there are significant challenges with accurate determination of the mobilities, which is compounded in determination of the Langevin reduction factor. Therefore one must be careful not to over interpret the presented data. As pointed out, for thin layers leakage current and series resistance of contacts can limit the voltage range over which diodes follow SCLC behavior. However, in a similar study using a device architecture designed to reduce these effects, we found similar behavior, with no apparent reduced recombination in any of the three BHJ devices. We can say at very least that despite the drastic changes in morphology and large differences in performance, processing does not have an exceptionally large effect on recombination reduction factor.

3.7 Solvent Vapor Annealing

With a better understanding of the effects of p-DTS(FBTTh$_2$)$_2$:PCBM morphology on device operation, we sought to develop a more tunable methodology towards optimizing morphology. The idea was to use post deposition exposure to solvent vapor – specifically, DIO vapor – as this would allow the DIO to work on a already cast film, without the kinetic restrains of the film formation process. Furthermore, the study should enhance our

understanding of the fundamental mechanisms behind solvent additives. Finally, vapor annealing should not be sensitive to casting methodologies, and thus it may not be necessary to do a full optimization procedure when scaling up from spin coating to more commercially relevant deposition methods.
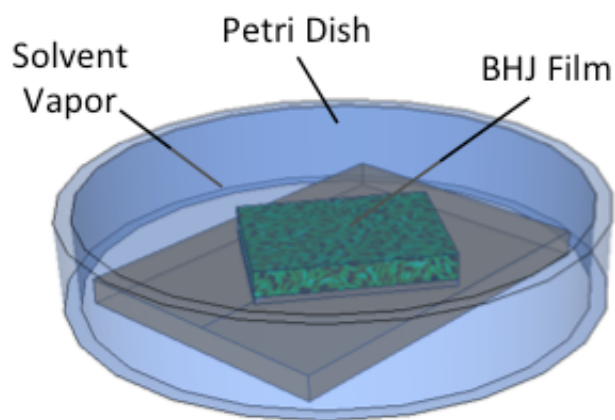
Figure 3.20. Solvent vapor annealing set-up consisting of a small petri dish with a built-in platform

Films of p-DTS(FBTTh$_2$)$_2$:PCBM were cast from pure chlorobenzene as described previously for the as-cast devices and then exposed to solvent vapor using the experimental setup diagrammed in Figure 3.20. A closed petri dish serves as the vapor chamber, with a small glass stage inside. Prior to introducing the films, a small amount of solvent was added to the chamber and heated on a hot plate until condensation was visible. The petri dish and vapor were then allowed to cool for 15 minutes to RT and it was assumed the vapor was saturated before films were introduced and placed on the small stage. When relatively volatile organic solvents such as chloroform or chlorobenzene were used to anneal the films, extreme crystallization occurs over the course of seconds. This was easily seen by AFM in Figure 3.21.
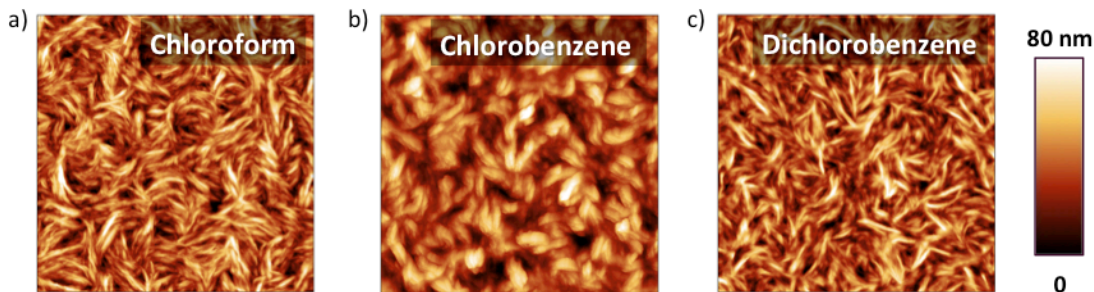
Figure 3.21. AFM topography images of p-DTS(FBTTH₂)₂:PCBM films after 1 minute of exposure to a) chloroform, b) chlorobenzene, and c) dichlorobenzene vapor

The solvent additive, DIO, has a vapor pressure reported as only 0.01-0.04 Pa, which is about 10,000 times lower than the vapor pressure of chlorobenzene. This means the vapor concentration in the chamber is much lower, which can extend the timescale over which it takes the films to reorganize. As-cast films were exposed to DIO vapor for different time durations before top electrodes were deposited afford solar cells of the architecture ITO/PEDOT/p-DTS(FBTTh₂)₂:PCBM /Ca/Al As we increased the time in which a film was vapor annealed, the *JV* properties of the device improved, increasing in J_{SC} and *FF* (Figure 3.22).
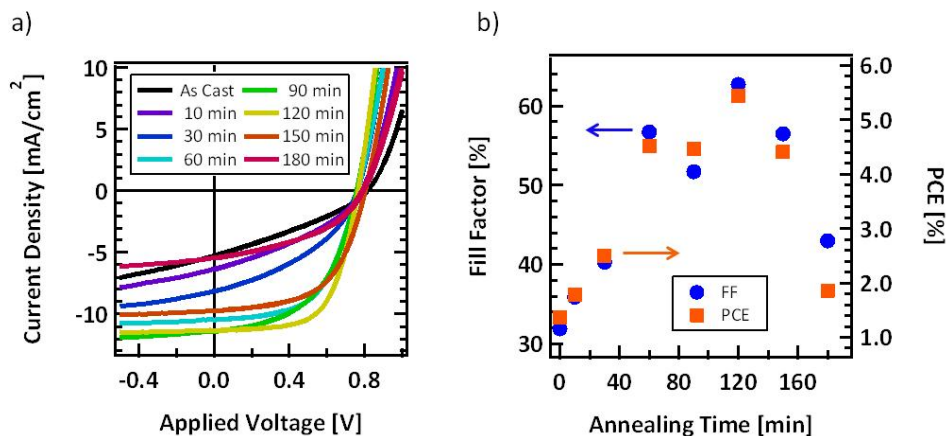
Figure 3.22. a) Solar cell performance of p-DTS(FBTTh₂)₂:PCBM system as a function of DIO solvent vapor annealing time with extracted b) power conversion efficiencies and c) FFs for eight solvent vapor annealing durations.

62

After two hours of solvent vapor annealing, our p-DTS(FBTTh$_2$)$_2$:PCBM solar cell attained a maximum power conversion efficiency of 5.44% with $J_{SC} = 11.4 \, VmA/cm^2$ $FF = 0.63$ and $V_{OC} = 0.77 \, V$. From Table 3.2, one can see that the optimization of vapor annealing is very similar to thermal annealing or adding DIO. There is a concomitant increase in J_{SC} and FF until they reach a maximum, after which additional annealing time (or additive) hurts the device. The reported V_{OC} is slightly low for this system, but remains nearly constant regardless of annealing time.

Table 3.2: Solar cell parameters as a function of solvent annealing time

Time (min.)	J_{SC} (mA/cm^2)	V_{OC} (V)	FF (%)	PCE (%)
0	5.3	0.81	0.32	1.4
30	8.2	0.76	0.40	2.5
60	10.5	0.76	0.57	4.5
120	11.4	0.77	0.63	5.4
150	9.7	0.80	0.57	4.4
180	5.5	0.79	0.43	1.9

The influence of solvent vapor annealing on the morphological properties of the bulk heterojunction film was first examined by means of UV-visible absorption spectroscopy (Figure 3.23a). In order to maintain a consistent film thickness, repeated solvent vapor annealing and absorption spectroscopy were performed on the same film for a cumulative duration of 120 minutes. Without any processing, the p-DTS(FBTTh$_2$)$_2$:PCBM blend film displays a broad peak at ~610 nm with a small shoulder peak at around 665 nm. Continued vapor annealing slightly enhances the overall absorption of the p-DTS(FBTTh$_2$)$_2$:PCBM film and triggers the emergence of vibronic structure at 676 nm. The overall enhancement in

absorption may be due to changes in the scattering of light due to changes in interface roughness, however there is also a significant change in absorption profile. Over two hours of solvent vapor annealing, instead of a single low energy peak with a shoulder, two distinct peaks emerge each of which are red-shifted by approximately 15 nm compared to the initial film. The evolution of the spectral profile is progressive with respect to annealing time, with the relative strength of the low-energy vibronic peak increasing over time. These features have been attributed to greater molecular ordering within the film.
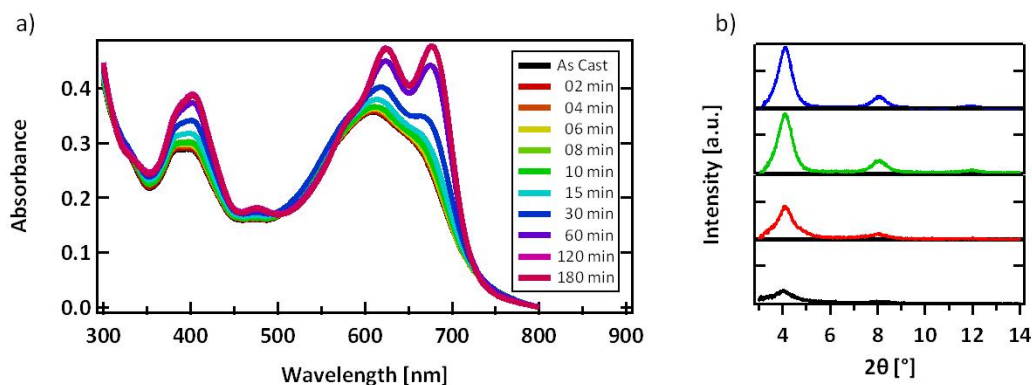
Figure 3.23. a) UV-Visible absorption spectra of the processed film with increasing solvent vapor annealing. b) X-ray diffraction data for four processing conditions: as-cast (black), 60 min. solvent vapor annealing (red), 120 min. solvent vapor annealing (green), 180 min. solvent vapor annealing. The spectra have been offset for clarity.

To better understand the cause of the shift in absorption spectra, we followed the morphological transformation of the film by means of X-ray diffraction (Figure 3.23b). From previous morphological studies, it is known that the crystalline p-DTS(FBTTh$_2$)$_2$ has a strong reflection corresponding to the alkyl stacking direction. As such, we followed the evolution of this diffraction peak at $2\theta = 4.1°$ in the blend film as a function of DIO vapor exposure time. The as-cast film has only a small diffraction peak at 4.1°. This suggests there is little crystallization present when the film is first cast. Crystallization of the p-DTS(FBTTh$_2$)$_2$ within the BHJ film occurs upon annealing.

After 60 minutes of solvent vapor annealing, the peak at 4.1° shows significantly higher intensity and a narrower profile compared to the as-cast film. Additionally, there is emergence of a broad peak at 8.2° which corresponds to the second order diffraction of the alkyl stacking. This suggests a more crystalline film. By two hours of vapor annealing, the first and second order reflections become stronger and better defined. A third reflection begins to manifest as well, indicating larger, more ordered crystallites within the film. There is not a significant difference in the X-ray diffraction from the 120 min. and 180 min. samples. This purports that beyond 120 minutes of solvent vapor annealing there is little change in the crystallization within the film.

While X-ray diffraction gives information about ordering on the molecular level, for insight into the larger scale phase separation which might occur in the blends, we utilized atomic force microscopy (AFM) as shown in Figure 3.24. As-cast, the p-DTS(FBTTh$_2$)$_2$:PCBM film is quite flat and lacks any clear features. Upon annealing for 60 min in DIO vapor, small surface features become visible. These surface structures become more pronounced at longer annealing times, growing in size. This is consistent with the XRD results, though unlike the XRD data, the features in the 180 min sample are significantly larger than in the 120 min sample. This suggests that at longer time scales, while additional crystallization may not occur, phase separation may still occur leading to larger phases. The AFM phase images of Figure 3.24b help confirm the phase separation that was suggested by the topographical AFM images.
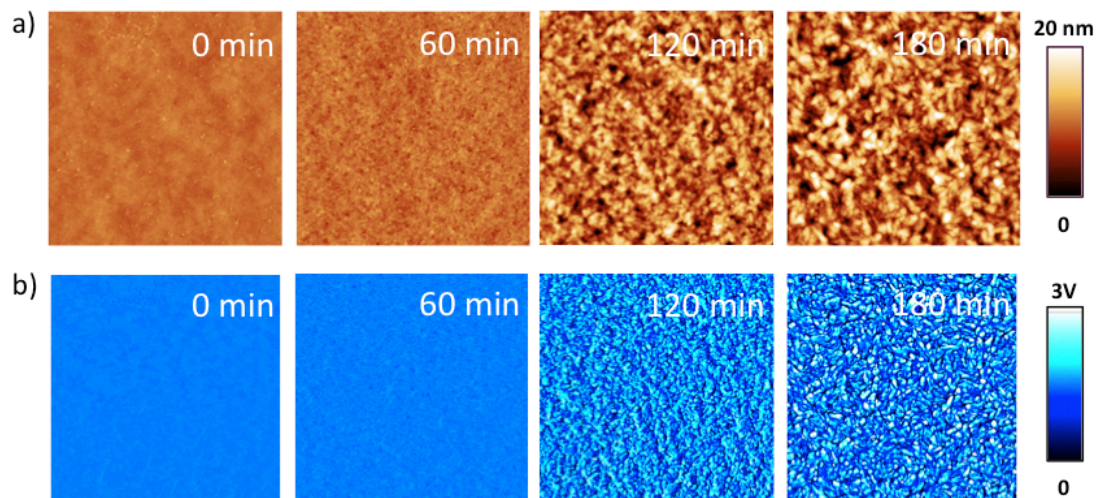
Figure 3.24. AFM characterization of four solvent vapor annealing durations showing a) topography and b) phase. Images are 5 x 5 μm

As demonstrated before, TEM can be a powerful technique to further understand the phase separation behavior of p-DTS(FBTTh$_2$)$_2$:PCBM blends. (Figure 3.25) The TEM further confirms what is seen by AFM and in the X-ray data. As the annealing time increases, crystalline p-DTS(FBTTh$_2$)$_2$ domains become apparent. It is difficult to quantify the exact size of the domains, but they do seem to grow in size with vapor annealing time. Qualitatively it is clear that the domains are similar to what is seen when cast with additive. They are small, crystalline, rice-grain features. The lattice spacing for the crystals is consistent with structure found previously.
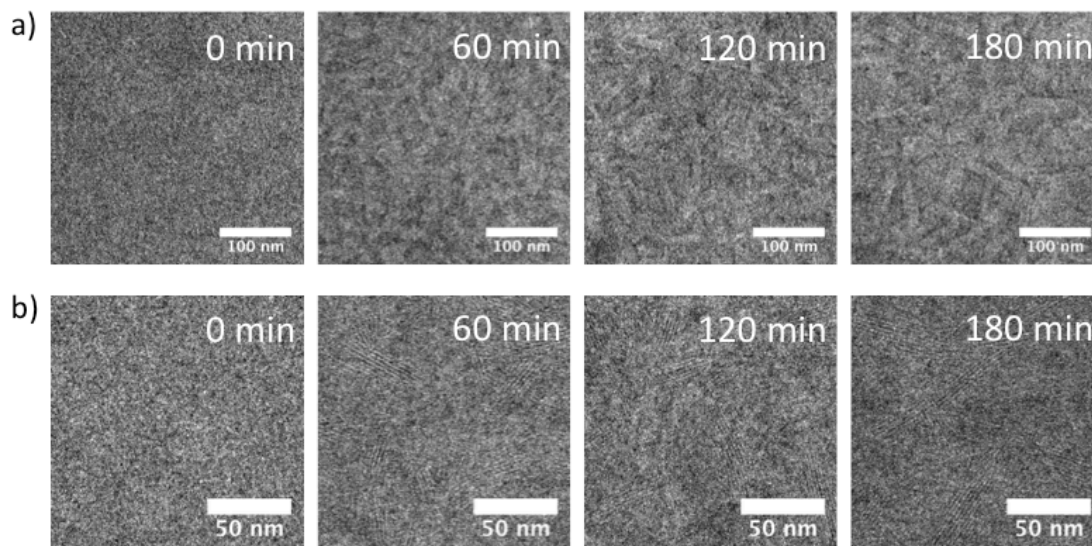
Figure 3.25. Bright field TEM characterization of four solvent vapor annealing durations, showing a) phase separation and b) crystallization at higher magnification

While solvent vapor annealing with DIO did not achieve quite as high performance as when it is included in the casting solvent, it was effective at improving *PCE* with similar improvements to what was seen with thermal annealing. Despite the low vapor pressure of DIO, it was able to penetrate the film, induce crystallization of the p-DTS(FBTTh$_2$)$_2$, and promote phase separation. This suggests there are specific interaction of DIO and the semiconductors, which results in the morphology optimization, and not just a kinetic effect of slowing down film formation. This topic continues to be explored. Furthermore, this demonstrates the utility of solvent vapor annealing in small molecule solar cells, and may prove important in the commercialization of OPV.

3.8 Conclusions

In the three years since we introduced and patented the p-DTS(FBTTh$_2$)$_2$ molecule, it has become commercially available from a number of sources, has been studied in a number of different contexts including hybrid solar cells and photodetectors, and the results we first

reported have been reproduced in a number of different countries by a number of different groups. It remains one of the highest performing small molecule donor materials and has become a standard in the field. The initial paper has been cited over 250 times, and over 50 papers have since been published using this material. As opposed to materials such as P3HT or PTB7, the efficiency of the standard devices never deviates much from what we first reported. This speaks to the reproducibility and robust nature of small molecules as well as the clear, accurate reporting of synthesis and device processing. Furthermore, it is validation of the most prominent accomplishment thus far of my career.

Chapter 4: Characterization and Optimization of a Mid-Bandgap Donor Material: p-SIDT(FBTTh$_2$)$_2$

4.1 Introduction

To harvest photons from a broader spectral range while maintaining large voltages, the highest achievable power conversion efficiencies (*PCE*s) require fabrication of tandem cells.[55][46][56][57][58][59] A primary consideration in this type of device structure is the availability of soluble semiconductors that have complementary absorption profiles and appropriate frontier orbital levels relative to each other for ensuring sufficient photocurrent generation and charge collection in the stacked, multijunction architectures. Considering the limited examples of molecular donors with blue-shifted absorption and deep highest occupied molecular orbital (HOMO) level (arbitrarily defined here as an onset below 700 nm and deeper than −5.3 eV, respectively), which can be used to fabricate efficient devices (*PCE* > 6%),[60] we set our objectives toward designing such materials. Of particular interest was to consider not only molecular features, but also the organizational tendencies as a result of solution processing.

A reasonable starting point for structural design is compound p-DTS(FBTTh$_2$)$_2$, which yields *PCE*s in excess of 8% by controlling the deposition conditions, modifying the compositions of BHJ blends with fullerene acceptors, and adjusting the device architectures.

[61][62][63] The compound p-DTS(FBTTh$_2$)$_2$ is a part of a class of donor materials described by the D^{1}AD^{2}AD^1 molecular architecture, in which D^1 (bithiophene) and D^2 (dithienosilole, DTS) are electron-rich fragments and A (fluorobenzothiadiazole) is an electron-poor fragment.[8][18] It seemed appropriate that exchanging the internal D^2 DTS fragment with a less electron rich counterpart would result in weaker charge transfer characteristics (therefore blue-shifted absorption and a deeper HOMO level).[64] On the basis of the recent success of polymers with silaindacenodithiophene (SIDT),[65][66][28][67] we postulated that benzo[1,2-b:4,5-b]bis(4,4′-dihexyl-4H-silolo[3,2-b]thiophene-2,2′-diyl)bis(6-fluoro-4-(5′-hexyl-[2,2′-bithiophene]-5-yl)benzo[c][1,2,5]thiadiazole (p-SIDT(FBTTh$_2$)$_2$) in Figure 4.1 would be a suitable candidate for achieving the goals set above. As a final relevant design element, p-DTS(FBTTh$_2$)$_2$ and p-SIDT(FBTTh$_2$)$_2$ keep the D^{1}A "wings" of the structure constant; only the central D^2 is different. We surmised that due to these overall structural similarities it would be possible to use previously optimized processing conditions as a starting point for exploring deposition conditions for the new material. Such considerations are worthwhile given the wide range of variables that must be investigated with a new material to optimize its function in a device.
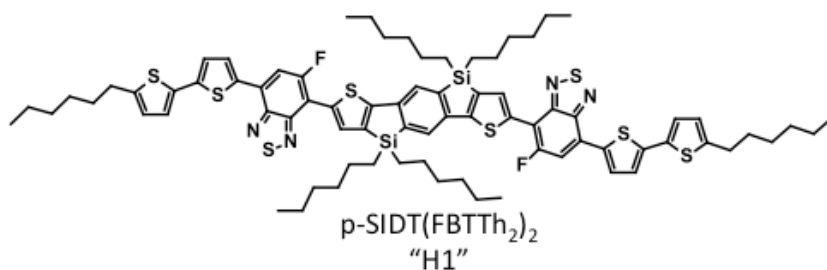
p-SIDT(FBTTh$_2$)$_2$
"H1"

Figure 4.1. Molecular structure of p-SIDT(FBTTh$_2$)$_2$.

70

4.2 Molecular Properties

Complete synthesis and characterization details for p-SIDT(FBTTh$_2$)$_2$ have been reported. Of note are the four hexyl side chains on the donor unit, which provide a high degree of solubility but do not affect the molecular backbone or optical absorption properties.

4.2.1 UV-Visible Absorption

Figure 4.2a shows the optical absorption spectra of p-SIDT(FBTTh$_2$)$_2$ in solution and in the solid state. In chloroform, p-SIDT(FBTTh$_2$)$_2$ shows intramolecular charge transfer absorption typical of chromophores with a $D^1AD^2AD^1$ architecture. One observes a low-energy transition with a maximum at 571 nm and a molar absorption coefficient of 6.5×104 M^{-1} cm^{-1}. The absorption maximum is red-shifted approximately 30 nm in thin films cast from chloroform. Additionally, there is an emergence of fine structure in the absorption profile which we attribute to molecular order in the solid state and a more planar molecular backbone structure[40][41]
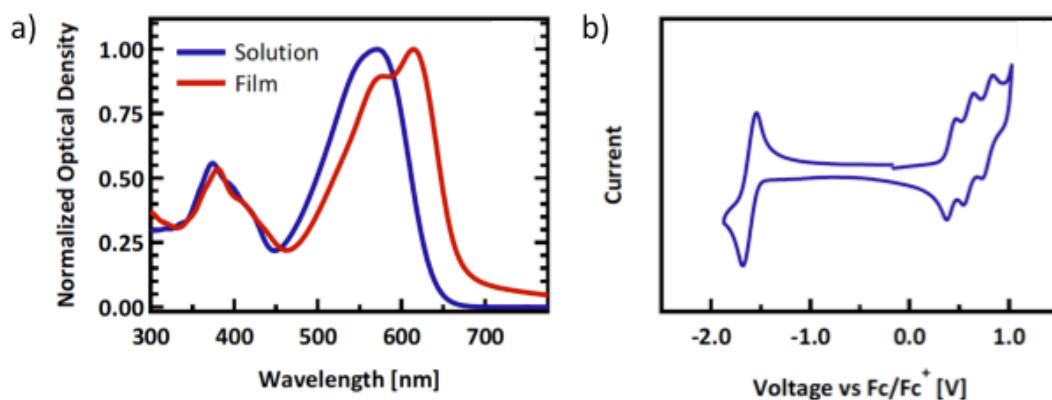
Figure 4.2. a) Absorption traces of neat P-SIDT(FBTTH2)2 in solution and film and b) CV trace of P-SIDT(FBTTH2)2

From the onset of the absorption (675 nm), the solid-state optical band gap was estimated to be 1.84 eV. This is a significantly wider band gap compared to that of p-DTS(FBTTh$_2$)$_2$, whose solid-state absorption onset at 780 nm suggests a band gap of 1.59 eV. Thus, the substitution of SIDT for the central DTS unit does increase the band gap as expected. It bears noting that the solid-state absorption profile of p-SIDT(FBTTh$_2$)$_2$ is quite comparable to that of the archetypical donor polymer P3HT, which remains a common material employed in the wide band gap subcells of state-of-the-art tandem architectures.[68]

4.2.2 Cyclic Voltammetry

Cyclic voltammetry measurements of p-SIDT(FBTTh$_2$)$_2$ in dichloromethane were carried out to estimate the position of the frontier orbital levels, as shown in Figure 4.2b. From the onset of the reversible reduction and oxidation peaks, the lowest unoccupied molecular orbital (LUMO) and HOMO energy levels of p-SIDT(FBTTh$_2$)$_2$ were estimated as −3.36 and −5.21 eV, respectively. The electrochemical band gap of 1.85 eV is consistent with the optical band gap.

Ultraviolet photoelectron spectroscopy (UPS) measurements were also used to evaluate the ionization potential of the material in the thin film and provided a value of −5.45 eV. The deep HOMO level of p-SIDT(FBTTh$_2$)$_2$ is supported by density functional theory calculations, which predict a HOMO level of −5.4 eV. These complementary measurements confirm that the introduction of an SIDT unit into the molecular framework effectively pushes the HOMO level to a lower energy value relative to that of p-DTS(FBTTh$_2$)$_2$.[61]

4.2.3 X-Ray Diffraction

While the previously noted fine structure seen in the absorption profile of p-SIDT(FBTTh$_2$)$_2$ suggests the presence of molecular order in the solid state, the crystalline properties of the donor material must be closely examined, as they can have a profound effect on the ability to form BHJ thin films of suitable photovoltaic performance, as observed with other small molecules.[62][69] Due to these considerations, grazing incidence wide-angle X-ray scattering (GIWAXS) was used to obtain high-resolution scattering profiles. Use of a 2-D detector allows for determination of both crystallite spacing and orientation, where χ denotes the angle from normal to the substrate.[70] Thin films of neat p-SIDT(FBTTh$_2$)$_2$ were examined to probe the crystalline nature of the pure donor material. When cast from chlorobenzene, the scattering profile of p-SIDT(FBTTh$_2$)$_2$, shown in Figure 4.3, reveals strong, anisotropic texturing, as evidenced by the number of sharp, distinct peaks. Attempts to grow a single crystal of p-SIDT(FBTTh2)2 of suitable size and quality proved unsuccessful, so we cannot definitively assign peaks of the GIWAXS profile. We can, however, interpret the reflections on the basis of convention, as is commonly done with polymer systems.[70]
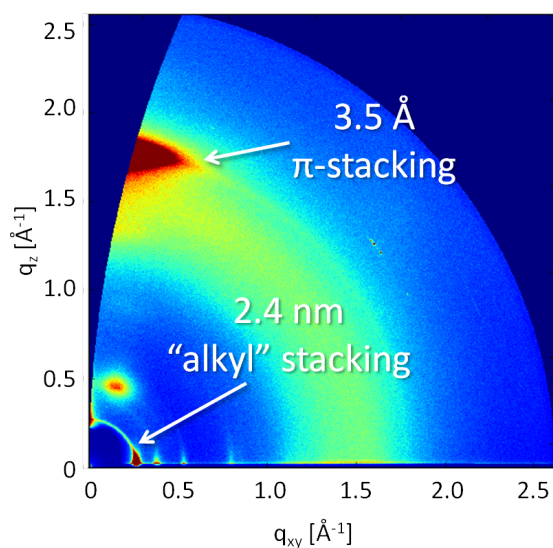
Figure 4.3. GIWAXS Scattering profile of a p-SIDT(FBTTh₂)₂ film

A strong out of plane reflection at q = 1.77 Å⁻¹ is observed in Figure 4.3, which corresponds to a real-space distance of 3.5 Å and is attributed to intermolecular π-stacking of the conjugated backbones. This π–π distance is comparable to those of other donor molecules, including p-DTS(FBTTh2)2.[52][53][62] Note that the π-stacking peak in this film is anisotropic with respect to χ, appearing only in the out of plane direction. This indicates that p-SIDT(FBTTh2)2 must preferentially adopt a "face-on" orientation with respect to the substrate with π-stacking through the thickness of the film. The strong intensity of the peak suggests the film is relatively well ordered in the π-stacking direction, though the film is only 20–40 nm thick, which may lead to some of the broadening of the peak.[70] This orientation is in contrast to what is observed with p-DTS(FBTTh2)2, which predominantly adopts an "edge-on" orientation.(24) How such significant morphological differences arise as a function of molecular connectivity is unclear at this point, but it is worth pointing out that the face-on texture of p-SIDT(FBTTh2)2 has also been observed in a number of conjugated polymer systems containing the same SIDT donor unit.[71][72]

A series of peaks at lower q values also appear in the in-plane direction. There is a sharp, intense peak at q = 0.26 Å⁻¹, which, while seen to some extent for all χ values, is considerably more evident in the in-plane direction. This corresponds to a distance of 2.4 nm in real space, which is typically associated with "alkyl stacking" or arising from columns of π-stacked units separated by alkyl side chains.[70][73][74] As π-stacking and alkyl stacking are often pseudo-orthogonal to each other, an alkyl spacing oriented in the plane of the substrate is also consistent with the proposed face-on texture.

Weaker reflections at q = 0.52 and 0.79 Å^{-1} are also observed in Figure 4.3 which are preferentially oriented in-plane and are assigned to the second- and third-order reflections from the alkyl stacking.[75][76] As a more quantitative measure, we can calculate the crystal correlation length (CCL), which reflects the extent of order in the crystalline lattice and increases with the crystallite size and/or perfection.[73] The Scherrer equation was used to estimate the correlation length from the peak breadths.[73][77] We find p-SIDT(FBTTh2)2 has a CCL of 37 nm. This is a relatively large CCL for molecular organic semiconductors deposited from solution and helps confirm the high degree of order in the neat material.[70,78]

Additional features (χ = 90°, q = 0.37 Å^{-1} and at χ = 20°, q = 0.50 Å^{-1}) are also observed that are difficult to assign in the absence of a single-crystal X-ray diffraction determination. All efforts to obtain such a structure have unfortunately been unsuccessful. We therefore use the GIWAXS information to determine a strong anisotropic arrangement that strongly favors the face-on orientation.

4.3 Solar Cell Device Performance

Initial solar cell performance was evaluated using the device architecture ITO/PEDOT:PSS/p-SIDT(FBTTh2)2:PCBM/Ca/Al. A concentration of 40 mg of total solids/mL of solvent was found to give a film thickness of 100 nm and was kept constant in subsequent studies. Following the optimization of p-DTS(FBTTh2)2, and other structurally similar small-molecule BHJ systems,[9,61] the use of small amounts of the solvent additive diiodooctane (DIO) was first screened, and it was found that a DIO concentration of 0.4% by volume was optimum; see further discussion below.

4.4 Donor:Acceptor Blend Ratio

Keeping the concentration of total solids in the solution constant at the optimum 0.4% DIO additive content, we set forth to understand the effects of systematically adjusting the p-SIDT(FBTTh2)2:PCBM blend ratio. The solar cell parameters obtained from these studies are shown in Table 4.1. Optimal performance was obtained at a 50:50 weight ratio of p-SIDT(FBTTh2)2:PCBM; under these conditions, the blend can achieve $J_{SC} = 11.0 \, mA/cm^2$, $V_{OC} = 0.91 \, V$, $FF = 0.65$ and $PCE = 6.4\%$. This performance is comparable to that of some of the highest performing small-molecule systems, despite the blue-shifted absorption.[9,60,63,79,11]

Table 4.1. Photovoltaic Characteristics of Devices as a Function of the p-SIDT(FBTTh2)2:PCBM Blend Ratio (concentration of DIO = 0.4% v/v)

D:A	J_{SC} (mA/cm^2)	V_{OC} (V)	FF (%)	PCE (%)
08:92	4.6	0.94	0.31	1.3
12:88	7.0	0.96	0.33	2.2
16:84	8.7	0.98	0.38	3.3
20:80	9.0	0.96	0.44	3.9
30:70	9.8	0.98	0.48	4.6
40:60	10.0	0.98	0.57	5.2
50:50	11.0	0.91	0.65	6.4
60:40	10.0	0.88	0.64	5.6
70:30	9.0	0.88	0.57	4.6
80:20	9.0	0.89	0.41	3.5
90:10	2.1	0.82	0.38	0.7

Closer examination of the blend ratio reveals unexpected results. Remarkably, photovoltaic efficiencies of over 3% can be maintained in blends over a range of p-SIDT(FBTTh2)2 content, from 80 down to 16 wt % within the blend. This stability is primarily attributed to J_{SC} values that remain relatively stable across this composition range. At 16% p-SIDT(FBTTh2)2, $J_{SC} = 8.8\ mA/cm^2$, increasing to a maximum of $J_{SC} = 11.0\ mA/cm^2$ for the 50:50 blend. The current then gradually decreases as the blends become more donor-rich, still achieving $J_{SC} = 9.0\ mA/cm^2$ at 80% p-SIDT(FBTTh2)2.

4.4.1 Optical Absorption

As all films are of approximately the same thickness, on the order of 100 nm, one might expect that increasing the p-SIDT(FBTTh2)2 content would lead to gains in absorption and should result in larger J_{SC}. In single-pass absorption experiments (Figure 4.4a) high donor content does indeed lead to a significantly increased absorbance in the visible range. However, for the total device absorption in the solar cell device (Figure 4.4b), which includes interface scattering and reflection off the back contact,[39] the differences in total light absorbed between the blends are not particularly dramatic. Absorption of 100 nm thick films on transparent substrates shows linearly shifting absorbance profiles, but in the two-pass architecture of a solar cell with reflective contact, when viewed on a linear scale, almost regardless of composition, the film can absorb a large fraction of light. Even at only 10% donor content, the absorption in the region of 450–650 nm remains over 75%. This is due both to the good absorption of p-SIDT(FBTTh2)2 and to the absorption of PCBM in this spectral region (Figure 4.4b, dark blue).
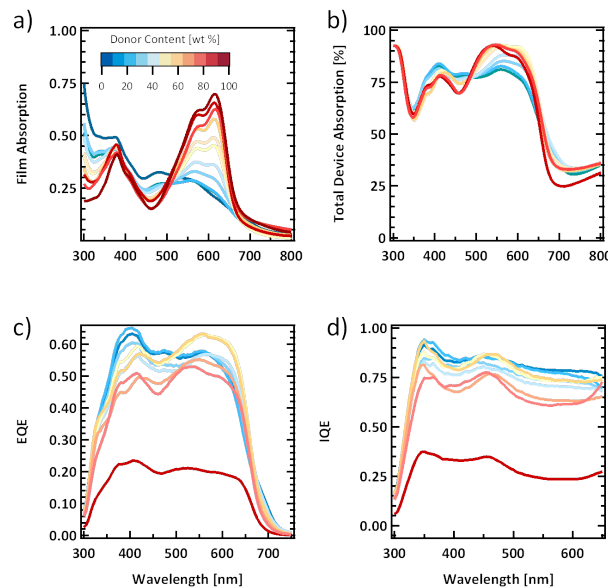
Figure 4.4. (a) Absorbance of p-SIDT(FBTTh2)2:PCBM films as a function of blend ratio, (b) total device absorption of the active layer films in a solar cell device architecture including a reflective Al back contact, (c) external quantum efficiency and (d) internal quantum efficiency of these devices.

While good absorption is requisite for large J_{SC}, it also indicates efficient and continuous charge transport pathways from 16:84 to 80:20 blend ratios, despite the composition. Utilizing a transfer matrix model to determine the parasitic absorption from the substrate and contacts, and the measured external quantum efficiencies (*EQE*s; see Figure 4.6c) of each blend, we calculated the internal quantum efficiency (*IQE*) for the different ratios and provide the results in Figure 4.6d.[39]

4.4.2 Internal Quantum Efficiency

Despite differences in *EQE*, the *IQE* maintains a relatively constant profile across the relevant spectral range for each blend, with only slightly higher efficiency near 400 nm due to PCBM absorption. *IQE* is highest, maintaining 80–90% efficiency across the entire spectral range, in blends with 20% p-SIDT(FBTTh2)2 and progressively decreases with increased donor content. The fact that the *IQE* in the PCBM absorbing region remains above

90% at such a large fullerene content indicates that nearly all of the fullerene excitons reach a p-SIDT(FBTTh2)2/PCBM interface, and despite the high acceptor content even up to 80 wt % PCBM, the domain size must not increase greatly past the exciton diffusion length. Furthermore, even at only 20% p-SIDT(FBTTh2)2, the hole transport must be sufficient to extract a large portion of the photogenerated holes at short circuit conditions to achieve such high IQE. From the IQE results, it is clear that the efficiencies of the charge generation and extraction processes are resilient toward the blend ratio. This suggests this materials system has the tendency to form a favorable morphology, with percolating phases able to effectively extract photogenerated holes and electrons, despite changes in composition.

4.4.3 Charge Transport

From Table 4.1, in the 16:84 to 80:20 range, while J_{SC} only ranges from 8.7 to 11 mA/cm^2, the changes in FF are much greater, ranging from 38% to 65%, with the FF peaking at a 50:50 blend ratio. One explanation for the steeper dependence of the FF would be an imbalance in charge transport. Though at short circuit the charge transport may not limit extraction, a reduced hole or electron mobility may lead to a buildup of a space charge within the devices and increased bimolecular recombination at low internal fields, explaining the low FF.[80][81] Charge transport was therefore probed by fabricating single-carrier diodes using charge-selective contacts.(56) Hole-selective devices were fabricated for the different blend ratios of the solar cells, using ITO/PEDOT:PSS as the bottom contact, but incorporating a gold contact on top of the BHJ film. The work function of gold should be significantly deep enough to prevent injection of electrons into the LUMO level of the PCBM or p-SIDT(FBTTh2)2.[82] The electron-selective device had an Al bottom contact and

Ca/Al top contact. The *JV* characteristics of the devices were fit to the space charge limited current (SCLC) Mott–Gurney expression[83][54]

$$J = \frac{9}{8} \varepsilon_r \varepsilon_0 \mu \frac{(V - V_{bi})^2}{L^3},$$

where ε_0 is the vacuum permeability, ε_r is the relative dielectric constant, V is the applied voltage less the builtin voltage, L is the device thickness, and μ is the zero-field charge carrier mobility (either hole or electron). It bears noting that despite the challenge of analyzing relatively thin (100 nm) diodes, the SCLC expression fits the experimental data quite well without the need for additional parameters such as a field dependence term, see Figure 4.5.
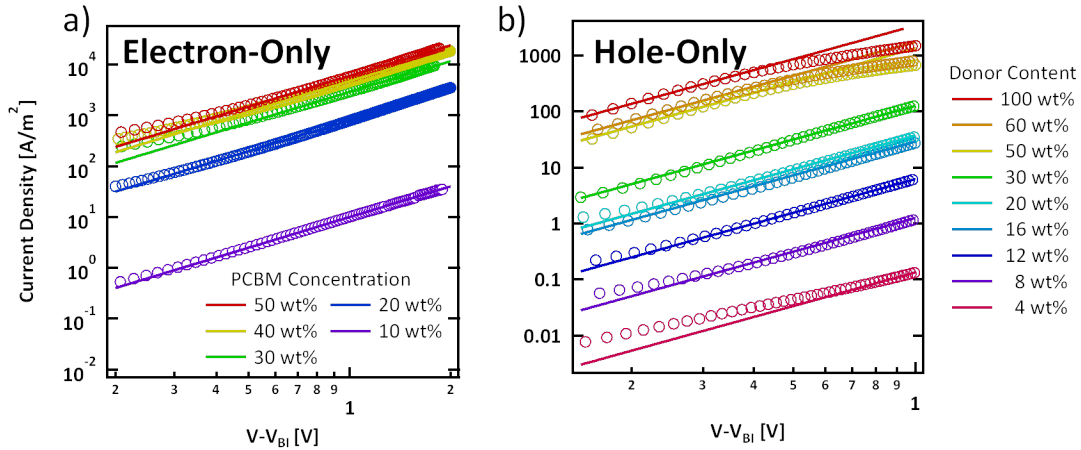
Figure 4.5 SCLC fits for a) electron-only, and b) hole-only devices at various blend ratios

The hole and electron mobilities are plotted as a function of the blend ratio in Figure 4.6. At a ratio of 50:50, the hole and electron mobilities are $4 \times 10{-}4$ and 1×10^{-3} cm^2/(V s), respectively, only reduced slightly from those of the neat materials ($\mu_{donor} = 1 \times 10^{-3}$ and $\mu_{PCBM} = 2 \times 10^{-3}$ cm^2/(V s). As the content of p-SIDT(FBTTh2)2 increases, and PCBM content is reduced, electron mobility (filled circles) is reduced. Likewise, when the cells are PCBM rich, the hole mobility (open squares) is reduced.

80
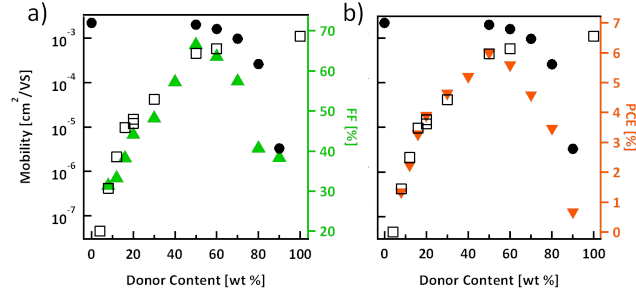
Figure 4.6. Electron (circles) and hole (square) mobilities across the range of p-SIDT(FBTTh$_2$)$_2$:PCBM blend ratios plotted showing remarkable similarities with the trends in (a) FF (green triangles) and (b) PCE (orange triangles). Donor in the x-axis refers to p-SIDT(FBTTh$_2$)$_2$.

When the mobility data are plotted with the solar cell parameters, as in Figure 4.6, it becomes clear that when either the hole or electron mobility are significantly reduced, the *FF*, and subsequently *PCE*, decreases. Thus, with a nearly constant J_{SC}, the efficiency remains high across all blend ratios in which the charge carrier mobilities are relatively balanced.

4.4.4 Percolation Threshold

Of note is the fact that the BHJs show SCLC behavior down to 4 wt % p-SIDT(FBTTh2)2. This indicates that, even at such low loading, the donor phase maintains percolation such that hole transport is possible. This is below the threshold predicted on the basis of a close-packed sphere model of percolation.[84,85] Such a low threshold suggests the system has a tendency to assemble into an interconnected percolating nanostructure. This phase behavior would reasonably explain the ability of the active layer to maintain high J_{SC} and thus *PCE* across such a wide range of blend ratios.

Typically, for a percolative system in which only one phase is conductive, the conductivity, σ, can be described by the equation[84–86]

$$\sigma = \sigma_{pure}(p - p_c)^t$$

where p is the volume fraction of the conductive phase, p_c is the percolation threshold volume fraction, and t is the critical exponent, which has been shown to typically be equal to 2.0 for systems in three dimensions.[84,87]
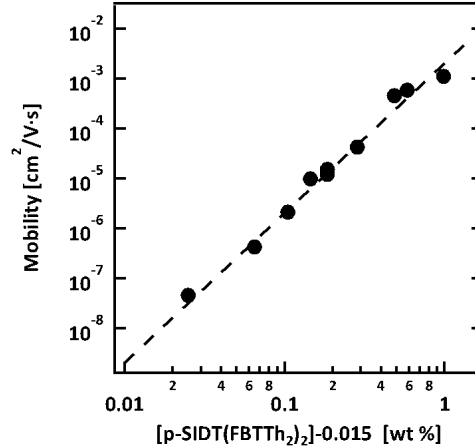
Figure 4.7. Hole mobility data fit to the percolation equation (3) with a percolation threshold of 1.5 wt% p-SIDT(FBTTh₂)₂and a critical exponent of 3.0.

If we assume that the densities of p-SIDT(FBTTh2)2 and PCBM are comparable, that is, that the weight percent of each material is approximately equal to the volume percent in the film, we can fit the mobility data to eq 3. We find empirically that the data fit best at a percolation threshold of 1.5% p-SIDT(FBTTh2)2 and a critical exponent of 3.0. That is

$$\mu \propto ([\text{P-SIDT(FBTTH2)2}] - 0.015)^3$$

A good fit to the experimental results indicates small perturbations in the percolation threshold have little effect on the value of t, implying that the hole mobility is indeed more sensitive to the blend ratio than should be expected from theory, which predicts t = 2.0. This may be due to the propensity for self-organization of the donor material to form domains of a particular size or shape[88] or could be caused by the presence of pure and impure phases, i.e., a mixed phase, which has also been suggested previously to result in a stronger dependence on the volume fraction.[87,89]

82

To fit these data well, we span nearly two decades in blend ratio and are able to fit mobilities ranging over 4 orders of magnitude from 10^{-7} to 10^{-3} cm^2/(V s). We believe, even at very low donor content, the transport remains exclusively in the p-SIDT(FBTTh2)2 and no holes are transported through the PCBM phase, as neat PCBM hole-only devices of the same architecture show large built-in voltages due to a large hole injection barrier from the ITO/PEDOT:PSS to its low-lying HOMO (5.8 eV).[90,91] Due to the difficulty in achieving the equivalently low leakage electron-only devices, unfortunately, we were only able to achieve a limited number of data points for electron mobilities in the blends, and a similar analysis of the percolation of PCBM is not possible.

4.5. Additive Concentration

In the study of the blend ratio, the DIO concentration in the solvent remained fixed at 0.4% (v/v) as was found in the initial optimization of p-DTS(FBTTh2)2:PCBM solar cells. However, the full effect of addition of DIO on device performance and film morphology deserves further discussion.

4.5.1 Device Performance

The complete results of this additive optimization are provided in Table 4.2. The V_{OC} shows a steady decrease upon addition of DIO starting from 1.0 V for devices with no additive decreasing to 0.87 V for devices processed from 1.0% DIO by volume. The increase in performance upon addition of DIO comes from the change in the FF (from 29% for no DIO to 64% with 0.4% DIO) and J_{SC} (from 5.7 mA/cm^2 for no DIO to 11.0 mA/cm^2 for 0.4% DIO). These differences cause devices prepared from pure chlorobenzene to yield $PCE = 1.7\%$, compared to $PCE = 6.4\%$ achieved with 0.4% DIO processing. The current voltage characteristics of these devices are also shown in Figure 4.8.
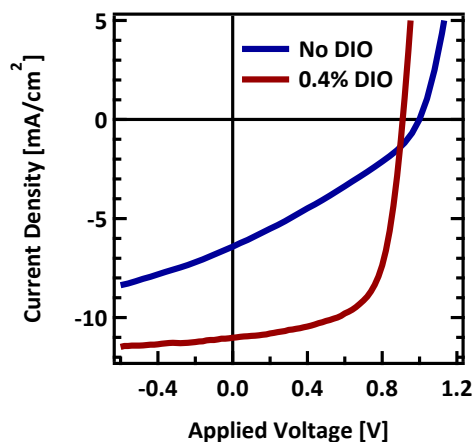
Figure 4.8 Current density-voltage (JV) characteristics of 50:50 p-SIDT(FBTTh₂)₂: PCBM blends processed without (blue) and with (red) DIO.

Alternatively, when the concentration of DIO in solution is increased to 1.0%, *FF* and J_{SC} drop to 35% and 4.1 mA/cm², respectively, yielding a *PCE* = 1.2%, thus illustrating the acute sensitivity of the active layer performance to the processing history.

Table 4.2. Photovoltaic Characteristics of 50:50 Devices as a Function of the DIO Concentration in the Processing Solution (D:A ratio = 50:50)

[DIO]	J_{SC} (mA/cm²)	V_{OC} (V)	FF (%)	PCE (%)
0	5.7	1.00	29	1.7
0.2	7.2	0.99	34	2.5
0.4	11.0	0.91	64	6.4
0.6	9.0	0.90	62	5.0
0.8	6.1	0.87	44	2.4
1	4.1	0.87	35	1.2

Altogether, these findings are well in line with the previous optimization of p-DTS(FBTTh2)2 and other small-molecule systems. Without additive, the devices achieve low efficiency in large part due to low *FF* (29%) and J_{SC} (5.7 mA/cm²). Each system optimizes at 0.4% DIO and shows a sharp drop off in performance when excess additive is

used. This helps demonstrate that, for the SIDT for DTS substitution, the processing conditions initially determined for p-DTS(FBTTh2)2 provide a reasonable starting point for optimizing the structurally similar p-SIDT(FBTTh2)2.

4.5.2 X-ray Diffraction

In previous small-molecule BHJ systems, it has been shown that the main function of the DIO additive is to affect the nanoscale morphology.[62,92] Specifically, the increased efficiencies have been ascribed to controlling the crystallization behavior of the donor materials within the blend films, resulting in optimized domain sizes. To probe if DIO serves a similar function in this system, we carried out GIWAXS measurements on p-SIDT(FBTTh2)2:PCBM films with and without additive (Figure 4.9). There are two relatively broad peaks seen at $q = 0.26$ and 1.4 Å–1 in the scattering profile of the 50:50 p-SIDT(FBTTh2)2:PCBM film cast from pure chlorobenzene Each is relatively diffuse and isotropic with respect to χ, implying random orientation within the film. The $q = 1.4$ Å–1 halo is typically attributed to amorphous scattering from the PCBM within the blend.[93] The peak at $q = 0.26$ Å–1 corresponds to the 2.4 nm alkyl spacing previously observed in the neat film (Figure 4.4). However, the weak intensity and diffuse nature of this reflection suggest the p-SIDT(FBTTh2)2 is relatively disordered in the blend cast without additive.
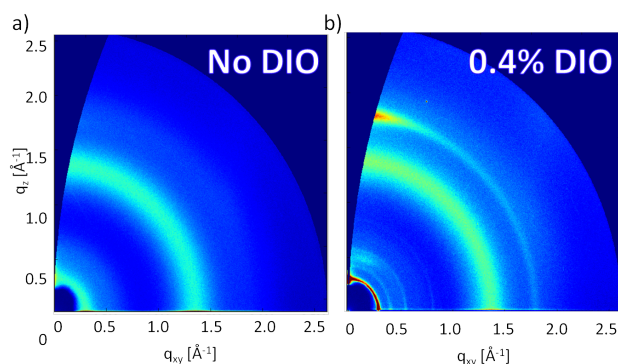
Figure 4.9. (a) GIWAXS scattering profiles of 50:50 p-SIDT(FBTTh$_2$)$_2$: PCBM blends processed (a) without and with (b) with 0.4% v/v DIO.

Processing with 0.4% DIO leads to significantly more obvious scattering (Figure 4.9b). There is a strong π-stacking reflection at q = 1.77 Å–1 primarily in the out-of-plane direction. The anisotropy of the reflection with respect to χ shows that while there are some population p-SIDT(FBTTh2)2 crystals oriented in all directions in this film, the material preferentially π-stacks out of the plane of the substrate, as it does in the neat film, again indicating a face-on orientation. The blend film also shows in-plane peaks at q = 0.26, 0.37, and 0.52 Å–1, and though they are less intense and less anisotropic with respect to χ compared to those in the neat film, they are consistent with a face-on texture.

From the breadth of the alkyl stacking peak oriented in-plane, we can calculate the CCL to be 28 nm in the additive processed blend. This length is significantly shorter than in the neat film, suggesting that, despite the use of solvent additive, the PCBM serves to break up some of the crystallization and anisotropy of the texturing. However, the CCL and appearance of higher order diffraction suggest that the p-SIDT(FBTTh2)2 regains quite a bit of order within the blend, particularly when compared to films cast from pure chlorobenzene. This is consistent with the results observed in the model p-DTS(FBTTh2)2 system;[62] DIO aids in the crystallization of the donor material within the BHJ.

4.5.3 Transmission Electron Microscopy

We can further probe the crystallization and phase separation behavior of these blends using transmission electron microscopy (TEM). At moderately high resolution, a small level of defocus is used to shift the contrast transfer function such that phase contrast is obtained for imaging of crystal lattice planes within the film.[88,94,95] Avoiding electron

beam damage is paramount with this technique, as the lattice fringes can begin to disappear after only seconds. A description of the imaging process followed has been described in detail previously.
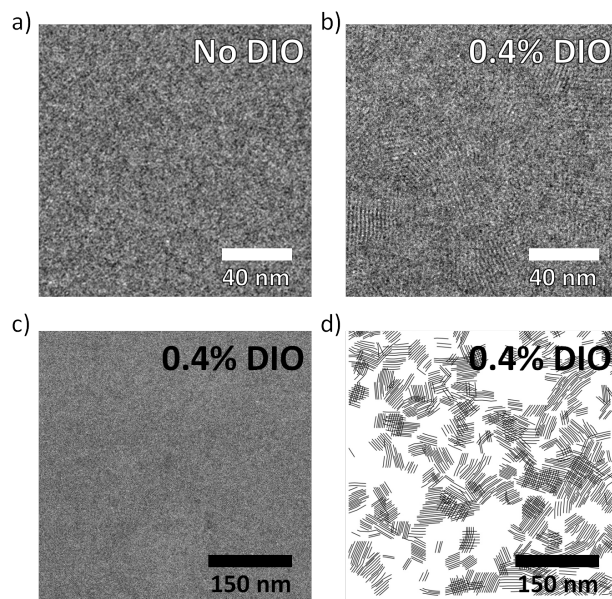
Figure 4.10. a) High resolution TEM image of 50:50 p-SIDT(FBTTh$_2$)$_2$:PCBM films, cast without and b) with 0.4% v/v DIO with c) larger area of DIO processed film and d) corresponding director field diagram highlighting lattice planes

When the film is processed from pure chlorobenzene, as shown in Figure 4.10a, there are no lattice fringes evident in the image. Additionally, there are no obvious larger scale features, which might arise from phase or mass-density contrast typically attributed to phase separation in the BHJ blend.[96] The relative homogeneity of the image is consistent with a molecularly well-mixed, disordered blend, consistent with the GIWAXS data.

In contrast, the p-SIDT(FBTTh2)2:PCBM film processed with 0.4% DIO shows a multitude of crystalline features throughout the area of the image, as seen by the parallel hatching in Figure 10b. The lattice spacing is at 2.4 nm, as observed with the neat film and by GIWAXS. Though there is little mass-thickness contrast between donor and acceptor phases on the larger scale (Figure 10c), we can use image analysis to extract the crystalline

regions imaged in larger areas. The results of this analysis are shown in the director field in Figure 10d. While there does not seem to be a uniform size or shape to the imaged crystals, they are on the order of 20–40 nm, oriented isotropically throughout the imaged area, consistent with the CCL extracted from the in-plane GIWAXS profile. In a BHJ, large phases can lead to exciton decay due to the limited diffusion length.[96] Thus, it is likely not a coincidence that, in this high-performance device, the majority of the imaged crystals are on a length scale comparable to the typical exciton diffusion length. The appearance of some larger scale phases may help to explain why *IQE* does not reach 100%.

To examine if the lower *FF* in devices cast without additive is due to the buildup of space charge,[80,81] we looked at hole and electron mobilities in each blend using single-carrier diodes as described above. All devices fit the SCLC behavior described by eq 1, and the extracted mobilities are shown below in Table 4.3. The hole mobilities extracted from the *JV* curves for blends cast without and with DIO are 1×10^{-4} and 4×10^{-4} cm^2/(V s), respectively, while the electron mobilities remain the same, 1×10^{-3} cm^2/(V s), for both devices. These electron mobilities are not significantly reduced compared to that of neat PCBM, so it does not seem that electron mobility poses a significant limitation.[91]

Table 4.3. Hole (μh) and Electron (μe) Mobilities Extracted from Single-Carrier Diodes for the 50:50 p-SIDT(FBTTh2)2:PCBM Blend

	μ_h (cm^2/(V s))	μ_e (cm^2/(V s))
no DIO	$1 \times 10{-4}$	$1 \times 10{-3}$
0.4% DIO	$4 \times 10{-4}$	$1 \times 10{-3}$

4.5.4 Light Intensity

Changes in *FF* are a consequence of the charge recombination present within the devices.[97,98] As an initial investigation into the recombination mechanisms, the solar cell

performance was tested over a range of incident light intensities,[35,99–101] the results of which are shown in Figure 4.11.
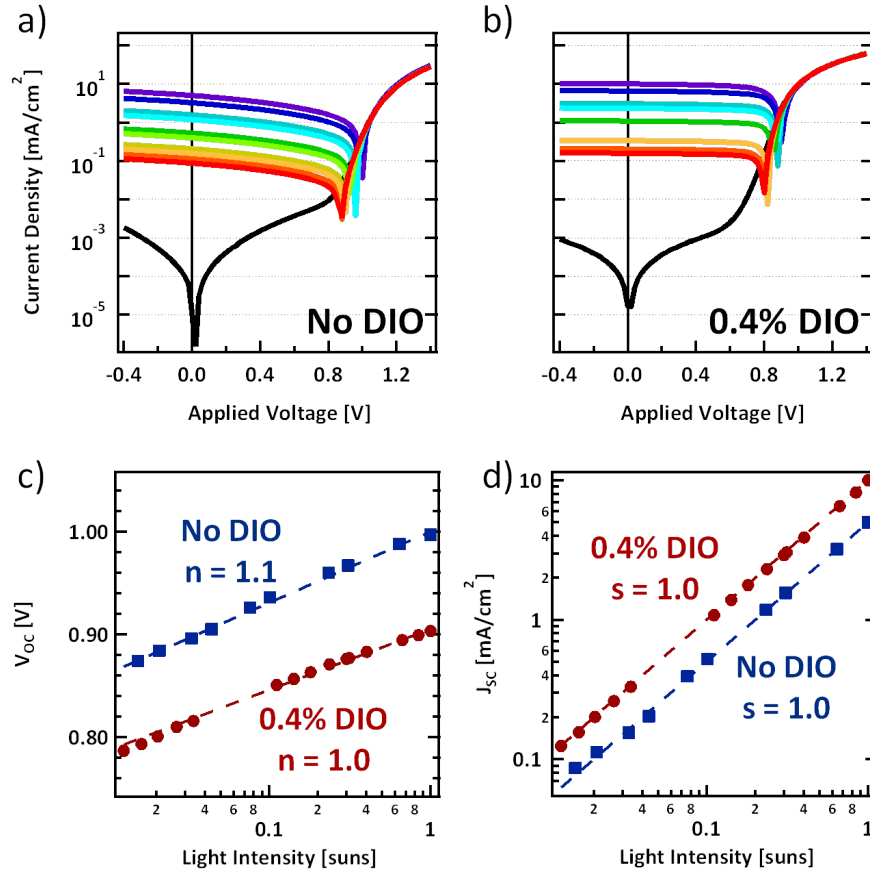
Figure 4.11. JV characteristics as a function of light intensity for devices cast a) without and b) with DIO along with extracted c) V_{OC} and d) J_{SC} values

For this type of study, devices must have sufficiently low dark current, such that it does not constitute a significant fraction of the total device current.[102] The dark current in these devices is at least an order of magnitude lower than the device current, even under only 0.015 sun illumination. From the V_{OC} and J_{SC} dependencies, there are no obvious differences between devise cast with and without DIO. Both follow the expected behavior. There are no clear signs of trapping, although from the same material, this is not unexpected.

To look more closely at the operation, to understand if space charge is playing a role in the performance differences, the photocurrent ($J_{photo} = J_{light} - J_{dark}$) is plotted against the effective voltage, that is, the voltage at which no photocurrent is generated less the applied voltage, V0 – V, at each intensity (Figure 4.12). The effective voltage determines the strength of the electric field within the device and thus the driving force for charge extraction.[35]
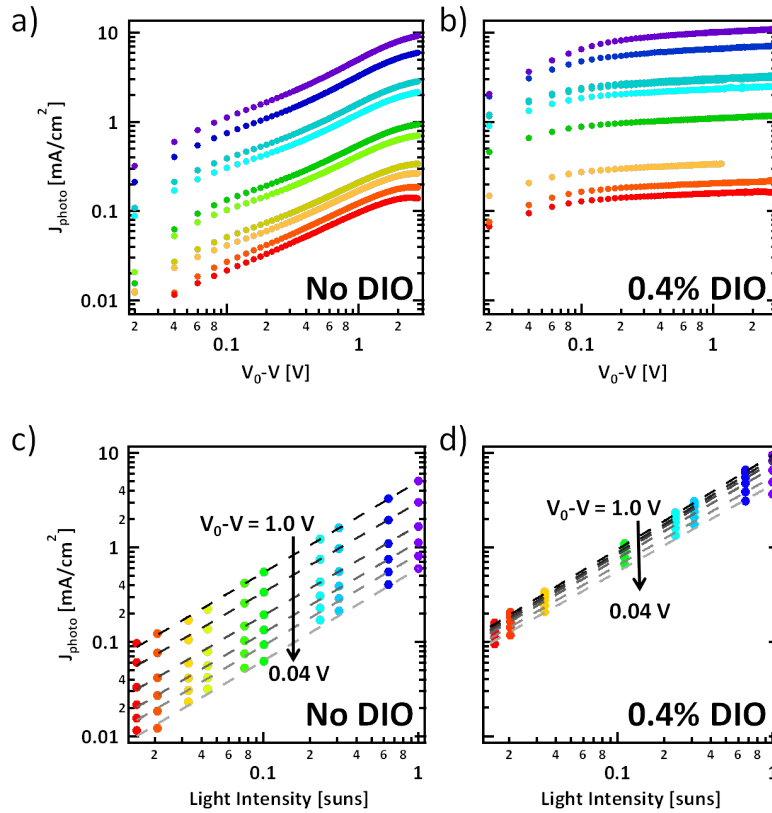
Figure 4.12 a,b) Photocurrent measurements as a function of effective voltage at various light intensities and c,d) photocurrent measurements as a function of light intensities at various effective voltages all fit to a slope of 1.0 for 50:50 p-SIDT(FBTTh$_2$)$_2$: PCBM blends processed without a,c) and with b,d) 0.4% v/v DIO.

The photocurrent in p-SIDT(FBTTh2)2:PCBM devices processed with additive quickly saturates at a low effective voltage of about 0.1 V (Figure 4.12b). This indicates the charge generation and extraction processes are relatively independent of the electric field.

90

For every intensity the behavior is the same; the photocurrent increases sharply at very low fields and plateaus starting at 0.1 V. Extracting the photocurrent values as a function of the light intensity at various effective voltages from 0.04 to 1.0 V, one observes that, even at low fields, the photocurrent always follows the light intensity, with a slope of s = 1.0 (Figure 4.12d). This suggests that, even at very low fields, charge buildup due to inefficient extraction is not a problem. This is consistent with the high mobility and *FF* for this device.

In contrast, the photocurrent in devices cast from pure chlorobenzene does not begin to saturate even up to 3 V (Figure 4.12a). Instead, the photocurrent continues to increase almost linearly as a function of the electric field. This is also reminiscent of a device that is limited by charge extraction, leading to the buildup of space charge. For a device limited by insufficient extraction, the high densities of charges lead to significantly increased bimolecular recombination and thus low *FF*. It is expected that, in a device limited by space charge, the maximum electrostatically allowed photocurrent that can be extracted should follow a 3/4 dependence on the generation rate, which we take to be directly proportional to the light intensity, or in other words, we should expect Jphoto to scale with the light intensity with a slope of s = 0.75.[80,81,103] However, from Figure 4.12c, it is clear that despite the extreme voltage dependence of photocurrent in the chlorobenzene cast device, this dependence does not change as a function of the internal field. Again, from 0.04 to 1.0 V of effective voltage, the device maintains a slope of s = 1.0. These results are not consistent with a buildup of space charge or an extraction-limited device. Together with the mobility results, these observations suggest that the strong field dependence of Jphoto and low *FF* might be due to a change in charge generation with applied bias rather than simply bimolecular recombination and inefficient charge extraction.[104–107]

91

4.6 Interplay of Thickness and Additive Concentration

In addition to its high efficiency, p-SIDT(FBTTh$_2$)$_2$ has favorable energy levels and absorption profile for incorporation into tandem solar cells; specifically, the relatively large absorption cutoff of 1.8 eV and large open circuit voltage (V_{OC}) of 910 mV make this materials system an ideal candidate for use in the blue-absorbing bottom cell in tandem solar cells.[56][55] However, there are a number of challenges associated with the stacked tandem architecture which must be addressed beyond choosing materials systems with complementary absorption, such as current matching the two sub-cells and maximizing the optical electric field distribution within the active layers.[108] There is then a great need for materials systems for which thickness of the active layer can be easily modulated without significant losses in efficiency.

One advantage of the central SIDT unit is that it incorporates four hexyl side chains which helps impart improved solubility in to p-SIDT(FBTTh$_2$)$_2$ over p-DTS(FBTTh$_2$)$_2$. The room temperature solubility of p-DTS(FBTTh2)2 with ethylhexyl chains is only 5 mg/mL in chloroform, while the solubility of p-SIDT(FBTTh2)2 is over 50 mg/mL in both chloroform and chlorobenzene. One would imagine that the improved solubility, would make available thicker active layers to help improve light absorption and thus Jsc. For many polymer systems, increasing thickness of the active layer has proved challenging though, often resulting in a decrease in *FF* and thus *PCE*. We sought to understand if we could overcome this challenge in a small molecule system, as

Active layer thickness was initially adjusted by starting with previously reported optimized solar cell conditions and only varying the total concentration of semiconductor material in solution. The optimized blend ratio of 50:50 wt% p-SIDT(FBTTh2)2:PCBM and

solvent condition of 0.4% DIO (v/v) in chlorobenzene (CB) were used for all films. Although spin rate can also be tuned to adjust thickness,[109] the viscosity of small molecule solutions is inherently much lower than that of conjugated polymers and therefore changing spin rate does not result in nearly as large film thickness variations as with conjugated polymers. Additionally, spin rate modifies drying kinetics of the thin film and can affect the self-assembly behavior and resulting nanostructure of the blend.[110] Thus, varying the solution concentration was deemed a more appropriate method to alter film thickness.

4.6.1 Constant Additive Devices

For solutions with concentrations ranging from 20–80 mg/mL, the active layer thickness increases linearly with solids concentration as shown in Figure 4.13, ranging from 50–200 nm. In dilute small molecule solutions, where the molecular weight of the molecules is relatively small, the viscosity remains nearly constant across the range of appropriate casting concentrations leading to this direct relationship between concentration and film thickness.[111] This is in contrast to polymeric systems, in which increased polymer concentration can lead to large changes in viscosity, resulting in a non-linear dependence of film thickness on polymer concentration.[109,112,113]
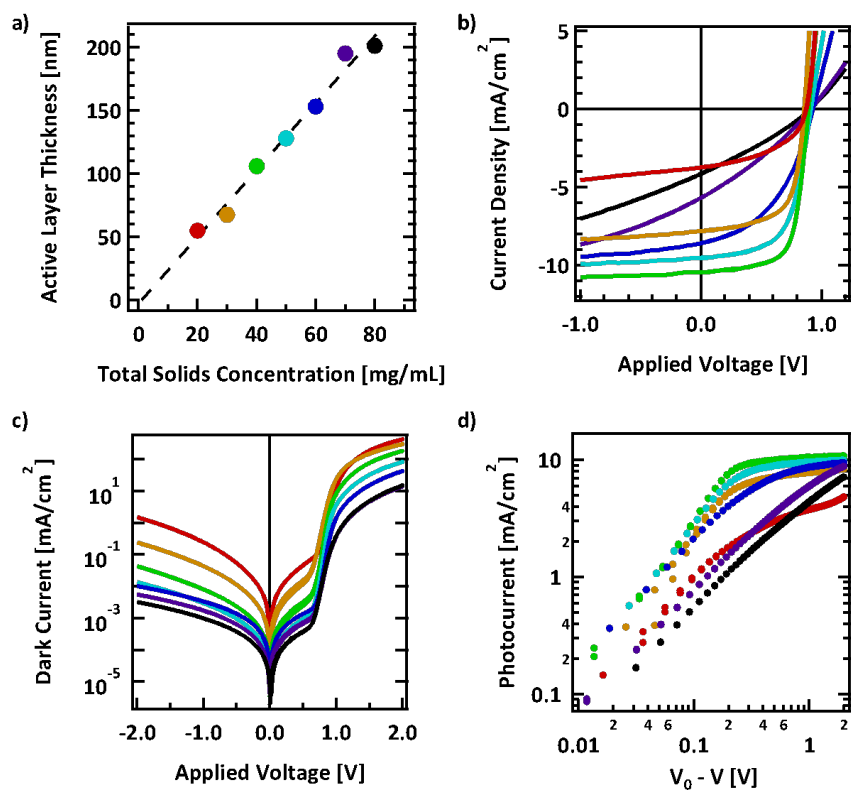
Figure 4.13. a) Active layer thickness dependence on solution concentration, with a linear fit and corresponding solar cell characteristics, including current-voltage characteristics b) under illumination and c) in the dark as well as d) photocurrent dependence on effective voltage. All solar cells were cast from chlorobenzene with 0.4% DIO (v/v), and spun at 1750 RPM.

Solar cells were fabricated as described previously in a standard architecture in which the active layer was sandwiched between an ITO/PEDOT:PSS (35 nm) anode and a Ca (15 nm)/Al (100 nm) cathode.[62] The solar cell characteristics of these devices are shown in Figure 4.13b. The optimized devices utilize 40 mg of total solids per 1 mL of solution, resulting in a 100 nm thick film (green). Decreasing the solid concentration, and thus thickness, results in a progressive reduction in J_{SC}. At a thickness of 50 nm (20 mg/mL) the J_{SC} is reduced to 3.8 mA/cm^2. It can be seen in the photocurrent plot (Figure 4.13d) that even at high effective field, the total photocurrent in these thinner devices never reaches that of the optimized 100 nm thick devices. The effective voltage, that is the voltage at which no photocurrent is generated minus the applied voltage, V_0-V, is divided by the active layer

thickness to determine the effective electric field within the device and thus the driving force for charge extraction.[35] It follows that at high internal fields photocurrent is not limited by extraction. For reference, an effective field of 107 V/m corresponds to 1 V over a 100 nm thick layer. In the thin devices however, even at a high effective electric field the current remains low. This can be rationalized by the reduced absorption of the thinner films; fewer photons are absorbed and thus fewer charges can be generated and extracted.[114]

As the concentration of the solution is increased beyond 40 mg/mL and devices become thicker, the J_{SC} also drops significantly with a concomitant loss in *FF*. This effect is drastic, leading to $J_{SC} = 3.0 \, mA/cm^2$ and $PCE = 0.7\%$ for devices with 200 nm thick active layers cast from an 80 mg/mL solution. This effect has previously been observed in polymer systems: thick devices lead to low *FF*.[114–117] As seen in Figure 4.13d, the photogenerated current of the 200 nm thick devices, shown in black, exhibits a large dependence on internal electric field. Even at an effective electric field of 1.5×107 V/m (V_0-V = 3V) the photocurrent continues to increase. The strong field dependence leads to the low *FF* and J_{SC}.[35,118] In polymer BHJ systems, the reduction in *FF* upon increasing active layer thickness is often ascribed to an increase in bimolecular recombination due to ineffective sweep out of free charges and a buildup of space charge.[114,119]

While indeed the voltage dependence of photocurrent of the thickest device is reminiscent of the characteristic shape of a space charge limited device,[80] the features of the thick device are also qualitatively similar to previously reported devices cast from pure CB, without the incorporation of DIO. The dissimilarity in field dependence between pure solvent and additive processed devices has been suggested to arise from field dependent charge generation (rather than bimolecular recombination) and is attributed to different

95

blend morphologies.[104–107] Specifically, the addition of DIO causes crystallization of p-SIDT(FBT2)2 within the blend leading to improved device operation. This observation may suggest that the increased field dependence, when moving from thin to thick devices, may also be due to a change in morphology and charge generation rather than simply the thick device being limited by mobility and increased bimolecular recombination. It follows that thicker devices may require different solvent and spin coating conditions to readjust morphology and improve efficiency.

4.6.2 Adjusting DIO Concentration

While the dynamics of spin coating are quite complicated, the simplest model breaks the film forming process down into two stages.[109,120,121] First, when a solution is cast and the substrate begins spinning, the droplet spreads such that the rotation rate and viscosity of the solution determine the initial thickness of the layer of solution on the surface, but evaporation during this initial process is ignored. The second stage is the evaporation of the solvent, the kinetics of which can be influenced by spin rate, concentration, vapor pressure, and the partial pressure of the evaporating solvent in the headspace above the rotating substrate.[109,120–123] This evaporation continues, concentrating the solution beyond its solubility, and a gel film is formed. Further drying can then be limited by diffusion of solvent through the film to the air interface. [124]

For a two-component BHJ solution, particularly one containing a mixed solvent system in the form of solvent additives, this process becomes more complex and convoluted.[122] Thus, an analytical treatment of this spin coating process is beyond the scope of this work. However, as a starting point for a very basic understanding of the dynamics of evaporation of this mixed solvent system, it is fruitful to simply begin with the

96

well known relationship of Raoult's law,[125] which states that for an ideal solvent mixture

the partial pressure, P_i, of a component, i, at a given temperature is given by:

$$P_i = P_i^{\circ} \chi_i$$

where P_i° image is the vapor pressure of the pure component i and χ_i image is the

mole fraction of component i in the mixture. It is clear that this is an oversimplification, as

this describes an ideal system at equilibrium, and not a real, dynamic system undergoing

evaporation. However, it serves to clearly highlight the importance of the vapor pressure of

each component during the evaporation process. At room temperature, CB has a reported

vapor pressure of 1300 Pa, [126,127] in contrast to DIO which has a reported vapor pressure of

only 0.01-0.04 Pa.[128,129] This difference of four to five orders of magnitude in vapor

pressure means that, when the film is initially cast, it is exclusively chlorobenzene that will

evaporate; DIO will behave more like a non-volatile solute than a co-solvent. Consequently,

as CB evaporates, the relative concentration of DIO will increase dramatically, along with

the concentration of semiconductor material. Once the film is formed, DIO allows for

continued molecular rearrangement over a much longer timescale compared with pure CB,

as has been demonstrated via in situ and time resolved X-ray studies.[130,131]

The optimum reported concentration of 0.4% DIO by volume (4 μL DIO in 1 mL

solution) can be equivalently expressed in terms of molarity, that is a DIO concentration of

20 μmolar. A total concentration of semiconductor material of 40 mg/mL in a 50:50 ratio of

p-SIDT(FBTTh2)2:PCBM corresponds to concentrations of p-SIDT(FBTTh2)2 and PCBM

of 14 and 19 μmolar, respectively. Therefore, in solution, there is on the order of only one

molecule of DIO for every p-SIDT(FBTTh2)2 or PC71-BM molecule. Again, this suggests

that the DIO does not affect the overall solvent properties during the initial drying, but

rather, only becomes important after much of the chlorobenzene has evaporated and the film has begun to form. The implication of such a rationale is that for thicker films, i.e. more semiconductor material initially in solution, additional DIO may be necessary to achieve the same effects as in thinner films, keeping the ratio of DIO molecules to PC71-BM and p-SIDT(FBTTh2)2 molecules fixed.

The interplay between film thickness and solvent additive concentration on device performance was examined through fabrication of an array of devices: DIO concentration was varied from 0-1.0% DIO (v/v) for solutions containing 20, 40, 60 and 80 mg/mL of total solids. The final dried film thickness was found to not vary significantly with DIO concentration, and always followed the linear dependence on concentration of solids shown in Figure 4.13a. Thus, films cast from 20, 40, 60, and 80 mg/mL solutions will herein also be referred to as 50, 100, 150, and 200 nm thick films, respectively. The complete results from this optimization process are shown in Table 4.4 with the optimized conditions for each thickness indicated in bold.

Table 4.4. Solar cell parameters for devices of various thicknesses cast from solutions with different concentrations of DIO

Solids [mg/mL]	DIO [v/v%]	J_{SC} [mA/cm^2]	V_{OC} [V]	FF [%]	PCE [%]
20	0	5.0	0.97	0.34	1.7
	0.2	6.0	0.90	0.65	3.5
	0.4	3.8	0.88	0.47	1.5
	0.6	1.7	0.74	0.38	0.5
	0.8	1.6	0.72	0.38	0.4
	1.0	1.6	0.44	0.33	0.2
40	0	5.7	1.00	0.29	1.7

	0.2	7.2	0.99	0.34	2.5
	0.4	11.0	0.91	0.64	6.4
	0.6	8.6	0.90	0.61	4.8
	0.8	6.1	0.87	0.44	2.4
	1.0	4.0	0.55	0.33	0.7
60	0	3.8	0.89	0.29	1.0
	0.2	7.9	0.92	0.37	2.7
	0.4	10.4	0.90	0.61	5.7
	0.6	10.0	0.87	0.72	6.2
	0.8	8.8	0.88	0.69	5.4
	1.0	5.6	0.87	0.59	2.8
80	0	2.9	0.93	0.28	0.8
	0.2	2.6	0.87	0.29	0.6
	0.4	3.0	0.86	0.28	0.7
	0.6	7.9	0.94	0.35	2.6
	0.8	10.7	0.89	0.58	5.5
	1.0	9.9	0.88	0.65	5.7

Though no thickness/DIO combination was able to improve upon the reported optimized efficiency of 6.4%, it is clearly beneficial to account for the change in initial semiconductor concentration by changing the concentration of DIO. Thicker devices require substantially more DIO to achieve their optimal performance while thinner films require a lower concentration of additive. The characteristics of the optimized devices are quite similar irrespective of active layer thickness. Though the optimized 50 nm thick devices

suffer from relatively low $J_{SC} = 6.0 \, mA/cm^2$ due to low photon absorption, the optimized 100, 150 and 200 nm devices are all able to achieve $PCE > 5.7\%$ and all optimized devices have $FF > 0.64$.

To establish a more quantitative relationship between optimized DIO concentration and film thickness, taking into account the expectation that at the initial time of film formation much of the DIO remains present, data from Table 4.4 is plotted as a function of DIO mole fraction (Figure 4.14). This refers to the number of moles of DIO present in solution compared to the total moles of solute (DIO, p-SIDT(FBTTh2)2, and PCBM) in solution. For example, the optimized 0.4% DIO solution with 40 mg/mL solids has a mole fraction of 0.38. In this way, we compare the amount of DIO relative to the amount of semiconductor material, and not to the amount of CB solvent.
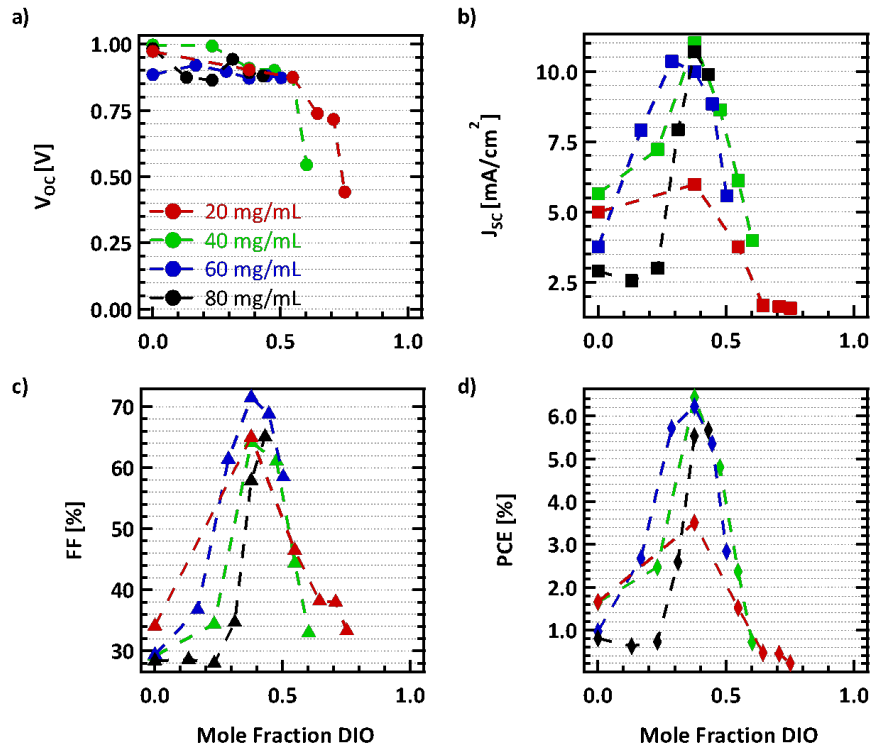

Figure 4.14. Extracted solar cell parameters, a)V_{OC}, b) J_{SC}, c) FF and d) PCE for devices cast from (red) 20, (green) 40, (blue) 60, and (black) 80 mg/ml solutions with 0-1.0% DIO where mol% DIO

When the solar cell parameters from each thickness and additive concentration are collapsed onto the same plots, general trends become quite apparent. As the concentration of DIO is increased, the V_{OC} tends to decrease, dropping sharply after ~0.50 mole fraction DIO. While this phenomenon remains unexplained, it is consistent with previous reports for structurally similar systems.[9,62] The effects of DIO on J_{SC} are also quite clear. While the absolute maximum in current varies with thickness, all devices have a maximum J_{SC} at a DIO mole fraction close to 0.40, regardless of film thickness. Too much or too little DIO results in significantly lower J_{SC} values. The similarity in the way FF is affected by DIO content at each thickness is even more blatant. Without DIO, all of the devices show very low FF, but show great improvements upon the introduction of additive. The maximum FF is achieved in each case at a mole fraction of DIO close to 0.40, while additional DIO results in a sharp decrease in FF. Devices processed with the same mole fraction of additive seem to have similar electrical characteristics regardless of thickness, suggesting they may also have similar morphological features. A thorough characterization of morphology using photoconductive atomic force microscopy (pc-AFM) and resonant soft X-ray scattering (R-SoXS) will be presented vide infra.

Such an array of conditions helps highlight how narrow the processing window is for achieving high PCE in solution processed small molecule BHJ solar cells. For all of the thicknesses, impressively high $FF > 64\%$ were achieved, but only in the optimized devices. This is contrary to previous work in polymer BHJ solar cells, which has suggested that thicker films inherently result in bimolecular recombination, and consequently lower FF.[114,117,119] Although such an argument may be true for extremely thick films or for

materials systems with low charge carrier mobilities, this work suggests an observed thickness dependence of *FF* may not inherently be attributed to transport limitations. Instead, the observed dependence may in fact be due to non-ideal processing, namely additive concentration. High *FF* is often related to more desirable morphologies resulting from appropriate phase separation within the BHJ. It stands to reason that these optimized devices may have similar morphologies characterized by similar domain size distribution, composition variation and degree of crystallinity.

Focusing on films of each thickness processed from pure solvent and the optimum concentration of DIO, shown in Figure 4.15, we can see that in each case, the DIO has the same fundamental effect on the shape of the J–V curve. Devices without any DIO all demonstrate very low *FF* and J_{SC}, though they do have high V_{OC}. The thickest devices give the lowest efficiencies with the lowest current. There is then a large, concomitant increase in *FF* and J_{SC} upon addition of DIO. Optimized devices cast from 40, 60, and 80 mg/mL solutions, with active layer thicknesses of 100, 150 and 200 nm respectively, all show remarkably similar *JV* characteristics, with *PCE* only ranging from 5.7 to 6.4% while the significantly lower J_{SC} in the 50 nm thick device (red) leads to a *PCE* = 3.5%.
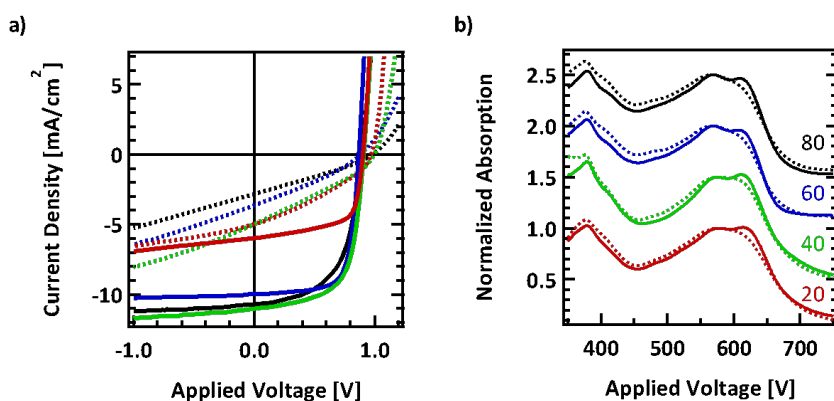

Figure 4.15. a) Current voltage characteristics of (red) 20, (green) 40, (blue) 60, and (black) 80 mg/ml solutions (dashed lines) without DIO and (solid lines) with optimum DIO concentrations

The efficiency of the optimized 50 nm device is limited by the low $J_{SC} = 6.0\ mA/cm^2$ despite the relatively high V_{OC} and *FF*. Doubling the thickness of the active layer to 100 nm gives an increase in J_{SC} to 11.0 mA/cm^2. This can be ascribed to the increase in absorption of the thin film. While one might expect J_{SC} to continue to increase with film thickness, in this system the current remains nearly constant for devices with 100–200 nm thick active layers. It has previously been shown that at 100 nm thickness, the device absorbs over 90% of incident photons over a large portion of the absorption range, thus the fractional gains in absorption upon increasing film thickness do not translate to increased current.[39] The J_{SC} can however, remain high (>9.9 mA/cm^2) across a large range in thicknesses, but only with appropriately scaled DIO content.

4.6.3 Morphology Characterization

We hypothesize that at each thickness, devices cast with the appropriate concentration of DIO have similar characteristics due to similarities in morphology. It was previously demonstrated via high resolution transmission electron microscopy (TEM) that DIO leads to crystallization of p-SIDT(FBTTh2)2 within the blend. However, TEM is not an appropriate characterization method for this study, as film thickness itself can cause changes in the imaging process.[15] Fortunately, as a result of the crystallization of p-SIDT(FBTTh2)2 there is an appearance of low-energy fine structure in the absorption profile of BHJ films. Thus, as an initial characterization, we examined the thin film absorption as a function of DIO concentration and thickness. The absorbance profiles of the devices from Figure 4.15a, that is, films of each thickness with the optimum additive

concentration and with no additive, are shown in Figure 4.15b. While it is clear that thicker films should result in increased absorption intensity, for the sake of examining the shape of the spectral features, we have normalized all absorbance profiles to the main peak at $\lambda = 575$ and displaced each spectrum for clarity. The raw absorption data is provided in Figure 4.16.
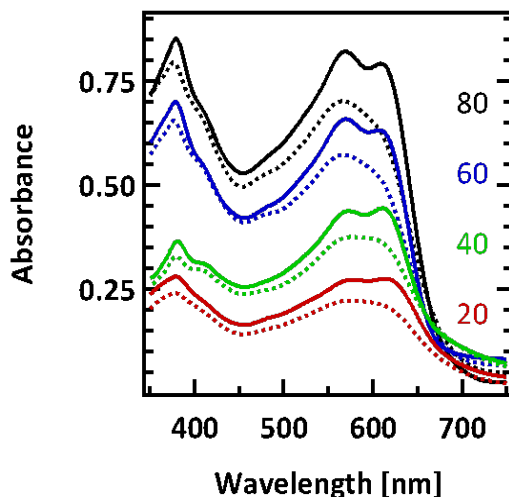
Figure 4.16. Thin film absorption profiles from the raw data for films cast from 20, 40, 60, and 80 mg/mL, (red, green, blue, black respectively) cast from either pure chlorobenzene (dashed) or the optimum DIO concentration (solid).

When cast without any DIO (dashed line), the absorption profiles of the blends look nearly identical regardless of thickness, with a relatively featureless peak centered at $\lambda = 575$ nm. For each thickness, upon introduction of DIO, a shoulder peak appears at $\lambda = 625$ nm. This vibronic structure is a characteristic of molecular order within the film. Simply comparing the optimized conditions, the absorption spectra for each thickness are remarkably similar.

As a further investigation of the nanoscale morphology, we employ pc-AFM.[132–135] In the pc-AFM technique, a sample is locally irradiated with light via an inverted microscope while a gold-coated, conductive AFM tip rasters across the surface of the film. The resulting image provides both spatially imaged surface topography and photogenerated

current, which gives information about the relative size of conductive domains in the BHJ film. At the condition of zero applied bias utilized in this experiment, the electric field distribution between the gold tip (~4.7 eV) and the PEDOT:PSS substrate (~5.2 eV) preferentially leads to the collection of photogenerated holes, expressed as positive current. The pc-AFM photocurrent images from the optimized devices of each thickness are shown in Figure 4.17.

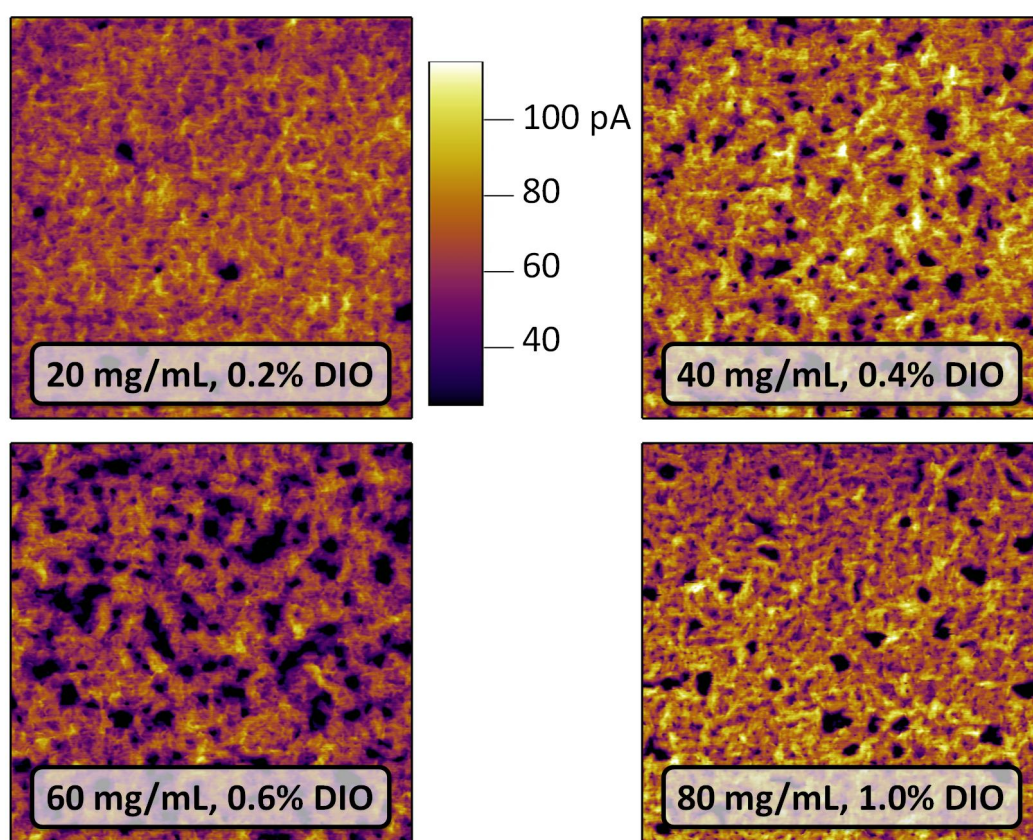*Figure 4.17. Pc-AFM images (5 μm x 5μm) collected under white light illumination at 0 V applied bias for films cast from (a-d) 20, 40, 60, and 80 mg/mL, respectively. The z-scale bar is the same for all four images.*

The pc-AFM images collected from the four optimized devices are quite similar. They show that a large fraction of the film generates high current (70–90 pA), denoted by

the bright regions, while there are regions of lower current (20–50 pA), denoted by the dark

areas of the images. It bears noting that in all four images, the current scale is the same. The

magnitude of the current and the size of the different high photocurrent domains remain

relatively similar in each image suggesting that in general the morphology of the four

different thickness films is quite similar.
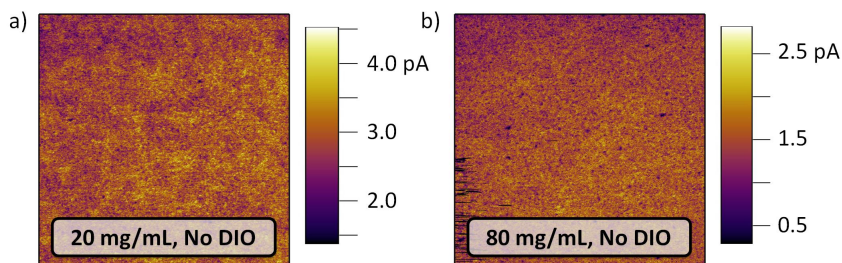
Figure 4.18. Photocurrent images of films as-cast from chlorobenzene from a) 20 mg/mL and b) 80 mg/mL solutions showing the nearly homogenous current across the film

This is in contrast to when devices are cast without additive (Figure 4.18). Without

additive, the nanoscale current in both the 50 and 200 nm thick films is over an order of

magnitude lower. The small current that is generated is relatively homogenous across the

film, with very small, ill-defined domains. Though there is a small difference in the

magnitude of the current, the 50 and 200 nm thick films cast from CB have similar

morphological features. This is consistent with the observation that processing without

additive results in an intimately mixed blend with little phase separation. On the other end of

the spectrum, when a 50 nm thick film is processed with 1.0% DIO, the phase separation is

massive (Figure 4.19). In the photocurrent image, large features on the order of microns can

be seen, while the surrounding film contributes almost no current. Comparing this with the

200 nm thick film processed with 1.0% DIO, reproduced in Figure 4.19b for easy

comparison, which shows much smaller domains with, improved current. It is clear that

keeping the mole ratio of additive constant is a much better approach to achieve similar morphology between films of different thickness than keeping the volume concentration consistent.
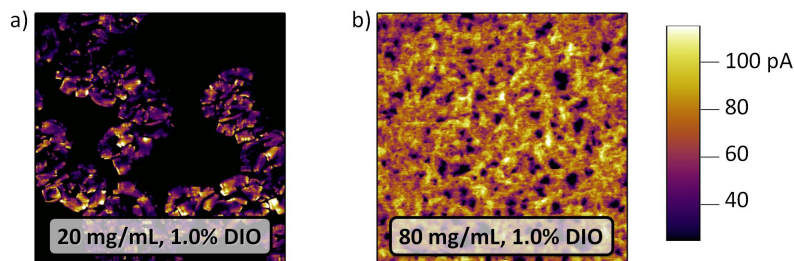
Figure 4.19. Photocurrent images of films cast from 1.0% DIO solutions with a) 20 mg/mL and b) 80 mg/mL total solids showing the drastically different morphologies that ensue.

To gain a more complete and statistically relevant picture of film morphology, the distributions of domain spacing along with the relative purities were assessed with R-SoXS, which quantifies in-plane composition variations over length scales spanning ~10–1000 nm.[136–139] This technique utilizes the unique optical contrast between the donor molecule and fullerene near the carbon 1s absorption edge. The real dispersive part of the refractive index, 1-δ, and the imaginary absorptive part, β, for the SIDT(FBTTh2)2 and PCBM are unique fingerprints of each material and provide scattering contrast that is proportional to $\Delta n^2 = \Delta \delta^2 + \Delta \beta^2$. Data were acquired below the absorption edge at 284.2 eV to optimize material contrast over the mass-thickness contrast and avoid damage[140] and fluorescence background. Figure 4.20a shows the scattering profiles for the optimized 20 mg/ml, 40 mg/ml and 80 mg/ml p-SIDT(FBTTh2)2:PCBM blends at a photon energy of 284.2 eV normalized for absorption and thickness.[139] The scattering profiles represent the distribution function of spatial frequency, $s = q/2\pi$ of the samples. The median of the distribution s_{median} corresponds to the characteristic median length scale, ξ, of the

corresponding distribution in real space with $\xi = 1/s_{median}$. For all three samples the scattering profiles have a similar shape with the dominant peak (long period) representing the domain spacing. The domain spacing calculated from the long period for all optimized samples was found to be in the range 25–30 nm.
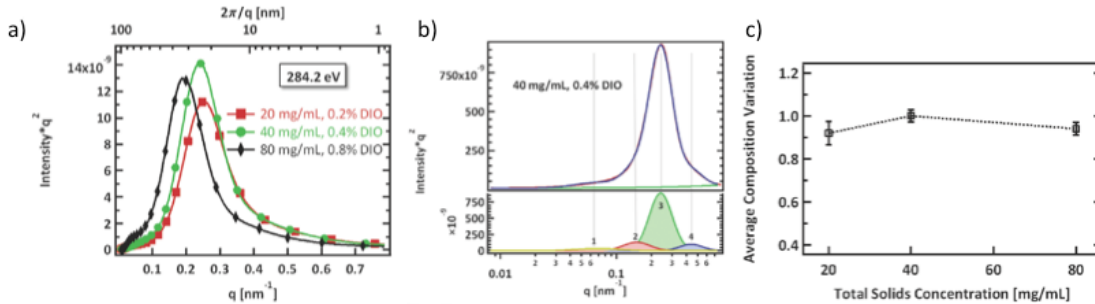
Figure 4.20. a) Lorentz-corrected and normalized R-SoXS scattering profiles (284.2 eV) from the optimized samples. Top axis is provided to aid conversion of long period to real-space values, b) Lin-log plot with log-normal fits for the 40 mg/ml 0.4% DIO sample. c) Average overall composition variation for the 3 samples obtained from integrations of the scattering profiles in (a).

In order to obtain further details regarding phase separation at multiple length scales,[139] the R-SoXS profiles were fitted by multiple log-normal peaks as shown in Figure 4.20b. A combination of four peaks was found to be necessary to obtain a good fit to the scattering profiles from the optimized samples. The fits reveal that the optimized samples do indeed have similar size scales with comparable median domain size ($\xi_i, i = 1,4$)corresponding to each peak as shown in Table 4.5. It is interesting to note that the size scale ratio (ξ_3/ξ_4) is close to 2 for all the optimized samples. This implies that the fits work well and that very similar morphologies are achieved for all optimized samples. Furthermore, this indicates the possible presence of either a similar hierarchical morphology or the results of a phase separation mechanism and kinetics that leads to a similar multiscale

morphology in all samples. Such a morphology, although with 4:1 ratio, has been recently

reported for a polymer-fullerene system[139] and is likely present in a number of systems.

Table 4.5. Median size scales (ξ) in nm and average composition variations <c> of the optimized 20, 40 and 80 mg/ml samples obtained from fits to R-SoXS scattering profiles shown in Figure 4.20a

Sample	Peak 1		Peak 2		Peak 3		Peak 4	
	ξ_1	$<c_1>$	ξ_2	$<c_2>$	ξ_3	$<c_3>$	ξ_4	$<c_4>$
20 mg/ml,	93.4	0.03	41.1	0.06	25.0	0.69	13.9	0.14
40 mg/ml	91.5	0.02	42.3	0.08	26.2	0.75	14.3	0.15
80 mg/ml	89.8	0.08	48.5	0.11	31.5	0.62	17.0	0.13

By integrating the scattering profiles and ensuring that scattering originates from

materials and not mass-thickness contrast, the total scattering intensity (TSI) reveals the

relative composition variations between the blends over the length scales probed.[137,138]

Mixed domains would result in lower scattering intensity (SI). The energy dependence of

the SI of peaks 2, 3 and 4 follows the scattering contrast of the p-SIDT(FBTTh2)2:PCBM,

demonstrating that these peaks measure the composition variations or volume fraction at the

respective two length scales. The average overall composition variations of the samples are

obtained by calculating the fractional SI of the fitted peaks and are shown in Figure 4.20c.

The fractional composition variations($\langle c_i \rangle, i = 1,4$), scaled to the average

fluctuation found for the 40mg/ml 0.4% DIO sample, corresponding to each fitted peak are

listed in Table 4.5. The nearly identical values observed demonstrate that not only do the

optimized devices have domains of similar size, but their purities, i.e. compositions, and/or

volume fractions are also very similar. It may be noted here that although the size scale

ratios of the phase separations as revealed by the peaks 3 and 4 might imply presence of

hierarchical or multiphase morphology a thorough investigation on the presence and origin of such structures is beyond the scope of this study.
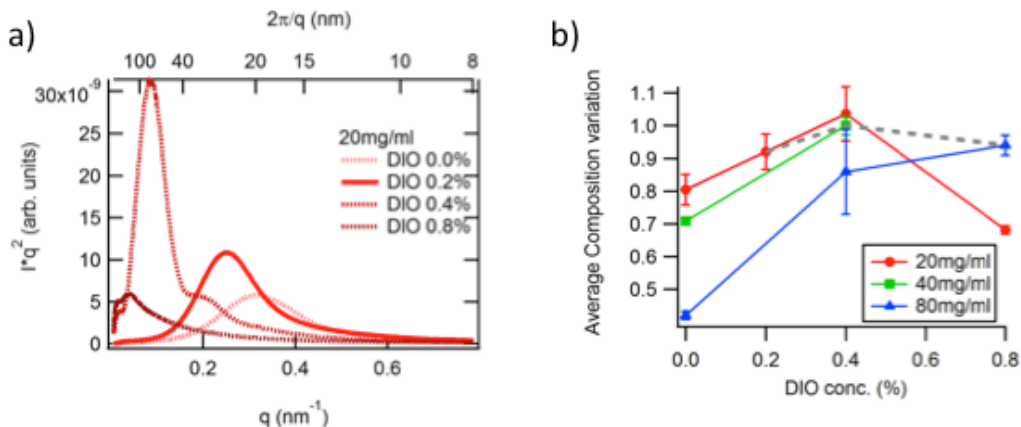

Figure 4.21. a) R-SoXS profiles at the photon energy of 284.2eV for 20mg/ml samples prepared with different DIO concentrations. The profiles were corrected for absorption following the Beer-Lambert law $I = I_0 e^{-\alpha t}$ where α is the linear absorption coefficient and t is the film thickness. Top axis is provided to aid conversion of long period to real-space values, b) relative composition variations (i.e., purity) extracted from R-SoXS for blends of different thickness and DIO content normalized to the most pure optimized device (40mg/ml, 0.4% DIO).

The non-monotonic trend observed for the *FF* for a given thickness and different DIO concentrations (Figure 4.13) can be explained from the R-SoXS data shown in Figure 4.21. From the scattering profiles for the each thickness at different DIO concentrations, we can extract the relative composition variation, or domain purity. It is clear that the devices with no DIO show small domains that are quite impure. Increasing the DIO concentration results in a larger domain size as well as increased purity. Additive concentrations beyond the optimum value result in domains that are too large, with decreased purity relative to optimum devices, thus resulting in lower J_{SC} and lower *FF*.

We have demonstrated that the p-SIDT(FBTTh2)2:PCBM system can achieve high efficiency across a broad range of thicknesses, though it is clear that thickness and additive concentration cannot be treated independently. For solvent additives to affect the BHJ

morphology, they must be at a concentration appropriate for the quantity of semiconducting material in the solution. While previously reduced efficiencies in thick devices were blamed on limitations in charge transport, we have shown these might instead be attributed to changes in morphology between thick and thin films. This also suggests a more straightforward approach to optimization: the mole fraction of additive should be the major consideration. In the case of the p-SIDT(FBTTh2)2:PCBM system, this mole fraction of DIO can be held at 0.4, which allows for the fabrication of efficient devices of various thicknesses.

These findings also help improve upon the general understanding of the working mechanisms of solvent additives. Due to differences in vapor pressure, it is fruitful to treat the solvent additive more like a non-volatile solute than a co-solvent. This helps explain why the additive concentration should scale with semiconductor content, and not be treated as a solvent property. Investigation by absorption, pc-AFM, and R-SoXS shows that keeping a constant mole fraction of DIO helps lead to nearly identical morphology (size and purity) across thicknesses. This work provides a straightforward method to adjusting active layer thickness in small molecule solar cells, an important consideration for fabrication of tandem cells and commercialization where active layers prepared via roll-to-roll processing or inkjet printing may require thicker films.

4.7 Conclusions

We set out to design a material with an increased bandgap compared with p-DTS(FBTTH$_2$)$_2$ in order to achieve improved V_{OC}. The somewhat less electron-rich central core, SIDT was incorporated to attain a deep HOMO level, but the rest of the material was identical to the structure of p-DTS(FBTTH$_2$)$_2$. With this new material, p-SIDT(FBTTH$_2$)$_2$,

the hope was that structural similarity to p-DTS(FBTTH$_2$)$_2$ would lead to similar molecular properties. Indeed, using conditions similar to those used in the optimized p-DTS(FBTTH$_2$)$_2$ system led to p-SIDT(FBTTH$_2$)$_2$ achieving 6.4% efficiency.

Throughout the optimization process, careful attention was paid to the effects of composition, additive concentration, and active layer thickness. The effects of processing on film structure and device behavior were studied in detail. It seems the best devices require small, highly crystalline, high purity domains. This leads to high charge carrier mobility in both the donor and acceptor phases, which is requisite for achieving high *FF* and *PCE*. The absorption profile of p-SIDT(FBTTH$_2$)$_2$, in combination with its high V_{OC} and *PCE* make it a perfect candidate for incorporation into tandem cells, and it is my hope that some day it may find commercial utility in such a device.

Chapter 5: Structural Modifications for Further Control Over Optoelectronic Properties

5.1 Introduction

The donor-acceptor approach, that is the coupling of alternating electron rich and electron deficient units has led to the fine tuning of molecular energy levels pushing the potential of OPV higher and higher. While increasing the open circuit voltage requires deep energy levels, the number of absorbed photons determines the maximum achievable current, and is set by the optical absorption profile and bandgap of the material. Thus donor materials with deep lying HOMO levels and relatively narrow bandgaps represent the Holy Grail for molecular design. Effectively this requires reducing the offset in LUMO levels between donor and acceptor materials as much as possible without losing the driving force for charge separation. While this has been understood for many years, the large library of conjugated moieties that has emerged, together with a more detailed understanding of the donor-acceptor approach has only recently made the synthesis of materials within this energy level sweet spot fairly routine. With the success of these D-A-D'-A-D framework, it was natural to attempt to further refine the optical and electronic properties of the materials, to either increase voltages, currents, or both. But while the molecular properties set the upper limit for potential OPV performance, actual performance, of course, depends heavily

on controlling morphology, and while molecular substitutions may seem small, re-optimizing processing can be quite a challenge.

The two previous chapters described new materials for which the changes in molecular structure were proved relatively innocent in affecting the casting process. Each required small amounts of DIO in chlorobenzene. Optimization required adjusting the additive concentration, semiconductor composition, spin speed, and total concentration, but these are relatively straightforward experiments. Neither required departure from the parameter space discovered for previous molecules, such as requiring new solvents or additives. In this chapter, we will examine some other, molecular manipulations, which, from an efficiency standpoint, were somewhat less successful.

5.2 Regiochemistry of the FBT unit of DTS(FBTTh$_2$)$_2$

Perhaps the simplest structural change to the p-DTS(FBTTh$_2$)$_2$ framework one can imagine is to simply change the regiochemistry of the fluorine atoms on the fluorinated benzothiadiazole (FBT) units. Instead of having the fluorines closest to the dithienosilole (DTS) core in the proximal positions, they could face "outward" being closest to the bithiophene endcaps, in the "distal" positions. Such investigations have been reported for similar molecules, and the changes have had profound effects on film formation and device performance.[69][141]

The distal regioisomer, d-DTS(FBTTh$_2$)$_2$, or T2, has previously been synthesized, and compared to the parent compound using density functional theory and natural bond orbital calculations as well as single crystal X-ray analysis. The difference in synthetic scheme to create the distal geometry versus the proximal version discussed in Chapter 3, simply requires coupling the FBT units to the DTS core first, and then adding the endcaps.[142] This

114

is allowed due to the regioselectivity of the Stille coupling imparted by asymmetry of the FBT unit. The resulting compounds are found to be quite similar both by theory and in single crystals with two possible confirmations each due to low barriers to rotation. This suggests they may behave similarly in films and devices

5.2.1 Molecular properties of distal vs. proximal

As a first insight into the properties of the new distal regioisomer, d-DTS(FBTTh$_2$)$_2$, or T2, solution phase cyclic voltammetry (CV) was used to determine the frontier molecular orbital levels. The traces and data are shown in Figure 5.1. By CV, the highest occupied molecular orbital (HOMO) and lowest unoccupied molecular level (LUMO) were determined to be -5.08 and -3.36 eV respectively, matching well with that of the parent proximal compound which had HOMO and LUMO values of -5.12 and -3.34 respectively. As the units in the conjugated backbone did not change, it is perhaps not surprising there is relatively little change in the energetics of the material. The CV data does however suggest a small change in bandgap.
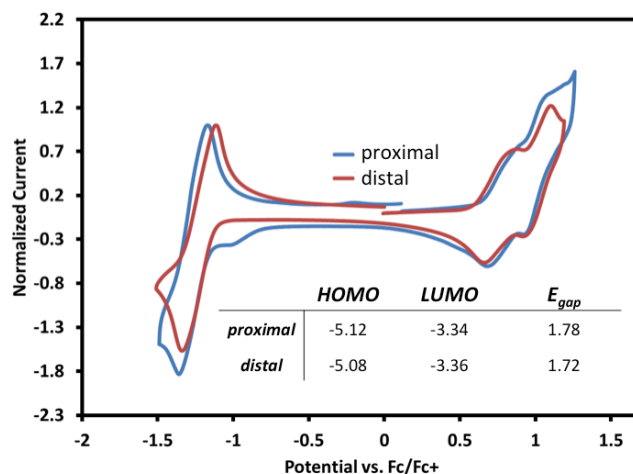

	HOMO	LUMO	E_{gap}
proximal	-5.12	-3.34	1.78
distal	-5.08	-3.36	1.72

Figure 5.1. Cyclic voltammetry traces and data for proximal and distal regioisomers

To further examine the electronics of the isomers, UV-visible absorption measurements were used on both solutions and films. The normalized absorbance traces are shown in Figure 5.2.
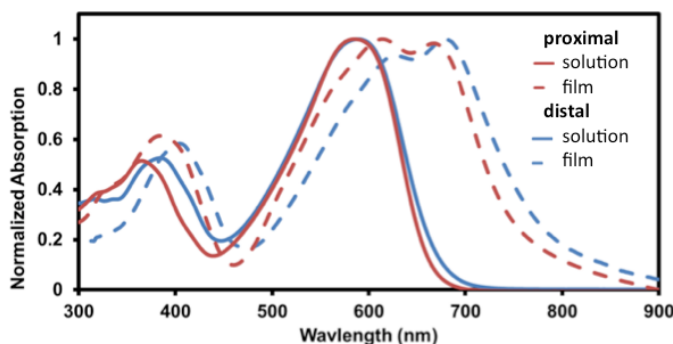
Figure 5.2. Solution (solid) and film (dashed) absorption profiles of proximal and distal regioisomers

In solution, there is very little change in absorption profile between the two isomers. The maximum absorption is at 590 nm for both materials, and the onsets are 670 and 660 nm for the proximal and distal isomers respectively. This confirms there is little difference in electronics caused by changing the region chemistry. In the solid state, electronics can be influenced by intermolecular interactions, so one might expect larger changes in the film absorption. Both materials show a significant redshift in the onset and maximum absorption upon moving to film. The proximal material shows a slightly larger shift in onset to 800 nm compared with 772 nm for the distal material. Furthermore, both show vibronic progressions suggesting order. The absorption values are shown below in Table 5.1

Table 5.1. Comparison of absorption parameters for proximal and distal DTS(FBTTh$_2$)$_2$ in both solution (chloroform) and film

	Solution			Film		
	λ_{max} (nm)	λ_{onset} (nm)	E_{gap}	λ_{max} (nm)	λ_{onset} (nm)	E_{gap}
proximal	590	670	1.85	678	800	1.55

| distal | | 590 | 660 | 1.88 | | 670 | 772 | 1.61 |

5.2.2 Solid state properties of distal vs. proximal

One of the surprising differences between the two materials is that the distal isomer has significantly better solubility in chloroform and chlorobenzene than the original proximal isomer. This might suggest weaker intermolecular interactions, which lead to aggregation or crystallization. Differential scanning calorimetry (DSC) was used to measure the melting and crystallization points of the two isomers as seen in Figure 5.3.
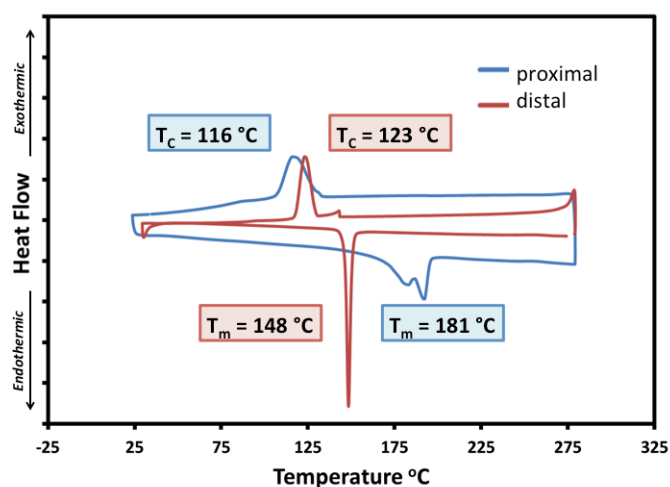
Figure 5.3. Melting and crystallization temperatures of DTS(FBTTh₂)₂ isomers using DSC

Indeed, the transition temperatures of the distal isomer are reduced. This suggests weaker solid-state intermolecular interactions. As was described in Chapter 3, it is necessary to induce molecular order and crystallization within the BHJ to achieve high performing solar cells. Thus, it is of vital importance to understand if the distal isomer crystallizes readily in a film like its isomeric partner does. For that investigation, we use x-ray scattering as shown in Figure 5.4.
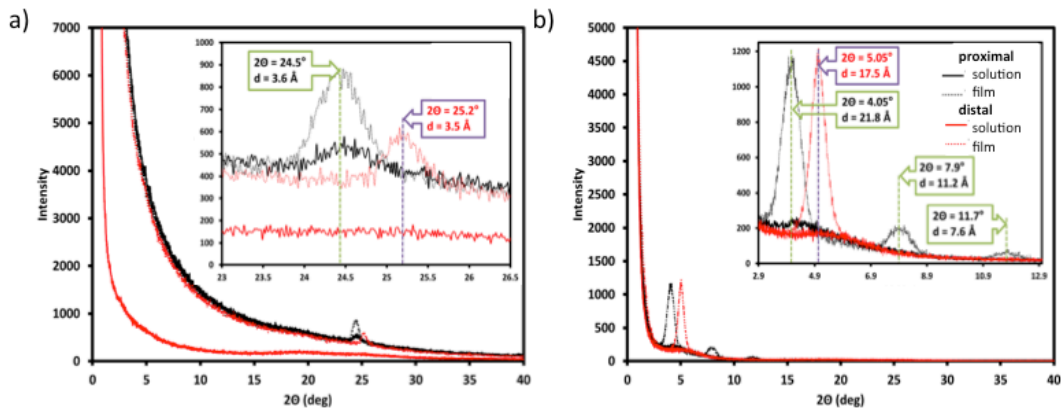
Figure 5.4. X-ray diffraction of films of DTS(FBTTh$_2$)$_2$ isomers showing a) in-plane and b) out-of-plane directions.

Without annealing, cast from chloroform, there are no strong peaks in-plane or out-of-plane for either of the two isomers. However, after annealing, a number of strong peaks begin to appear. As described in Chapter 3, the proximal isomer shows a strong in-plane peak at 24.5°, which corresponds to a real space distance of 3.6 Å. The distal isomer has a strong in-plane peak at 25.2°, which corresponds to a real space distance of 3.5 Å. There is thus a slight compression of the π-stacking distance. However, in both systems, annealing leads to crystallinity, and specifically, in an "edge-on" texture such that the π-stacking is in the plane of the film. There is no π-stacking peak in the out-of-plane-direction.

In the out-of-plane direction however, there are strong alkyl-stacking peaks. In the proximal isomer, there are three orders of diffraction at 4.1°, 7.9°, and 11.7° which corresponds to a real space distance of 2.2 nm. The distal isomer only has a single diffraction peak at 5.1°, which corresponds to a real space distance of 1.75 nm. The fact that there are not higher orders of diffraction suggests it may not be as well ordered as seen in the proximal system. Perhaps more importantly, though the distal isomer does have the tendency to crystallize, the film organization of the two isomers is different. Furthermore,

this information is all taken from pure films, and does not necessarily reflect what will happen in blends.

5.2.3 Device properties of distal vs. proximal

As described in Chapter 3, p-DTS(FBTTh$_2$)$_2$:PCBM devices cast from chlorobenzene show low performance in solar cell devices. However, annealing or the use of solvent additives greatly improves the current voltage characteristics, with maximum efficiencies in the devices made with diiodooctane (DIO) reaching 7.0 %. With that in mind, devices using the distal analogue with PCBM were made using the same three conditions as studied with the proximal isomer. The results are shown below in Figure 5.5 along with the best condition reported earlier. [61,62]
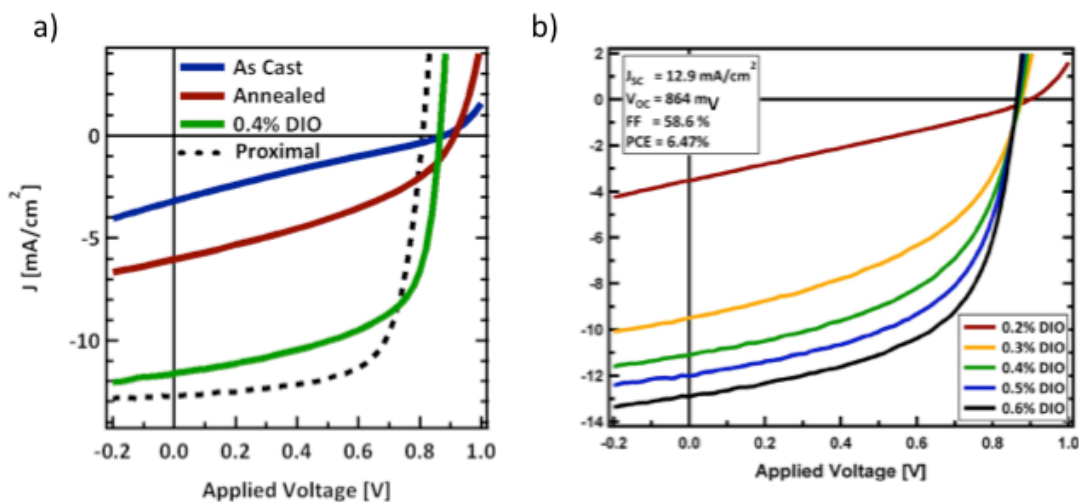
Figure 5.5. Current voltage characteristics of d-DTS(FBTTh$_2$)$_2$:PCBM devices cast a) under the three conditions studied for the proximal analogue (optimized devices shown in dashed line) and b) thicker devices optimized for DIO content

Looking at the devices prepared according to the three conditions studied in Chapter 3, the distal analogue behaves quite similarly to its proximal analogue. Efficiencies of devise cast from chlorobenzene showed very low performance with a notably low *FF* and

$PCE = 0.76\%$. Annealing the device helps improve the shape of the curve, and the J_{SC}. In the blends with distal material, annealing is not nearly as effective as with the proximal analogue. This might be due to a lack of crystallization, as X-ray diffraction studies showed that the distal material had less of a tendency to crystallize when subjected to annealing. However, adding the solvent additive DIO again gave large improvements in device performance. The FF and J_{SC} both improve dramatically, resulting in a $PCE = 6.1\%$. The full details of the solar cell parameters are given in Table 5.2.

Table 5.2. Solar cell characteristics of distal isomer with PCBM under three typical conditions as well as optimized DIO condition

	J_{SC} [mA/cm^2]	V_{OC} [mV]	FF [%]	PCE [%]
As Cast	3.19	900	23.6	0.68
Annealed	6.04	946	37.1	2.12
0.4% DIO	11.6	876	59.8	6.09
0.6% DIO	12.9	864	58.6	6.47

As was noted previously, the distal isomer shows better solubility, and thus there was an effort to make thicker blend films. Devices utilizing 45 mg/mL (125 nm films) were made and optimized by varying blend ratio, spin speed, and additive concentration. The results of the DIO optimization process are shown in Figure 5.5b. The optimum device was found at 0.6% DIO and gave a $PCE = 6.5\%$ with $J_{SC} = 12.9 \ mA/cm^2$, $V_{OC} = 0.86 \ V$ and $FF = 0.59$. This overall performance is quite close to what was seen for the proximal isomer, though suffers from a lower FF. In fact, the device has improved V_{OC} due to slightly deeper energy levels and yet also an improved J_{SC}. The thicker film allows for an improved short circuit current and saturation current in reverse bias despite a slight blue shift in absorption edge. This gives the distal isomer a somewhat higher potential for performance, but would require an improvement in FF.

In the previous systems studied, it was shown that *FF* can be highly dependent on processing, and specifically, that the donor material must have adequate phase separation. Bright field transmission electron microscopy (TEM) images of the as cast and optimum blend films are shown in Figure 5.6.
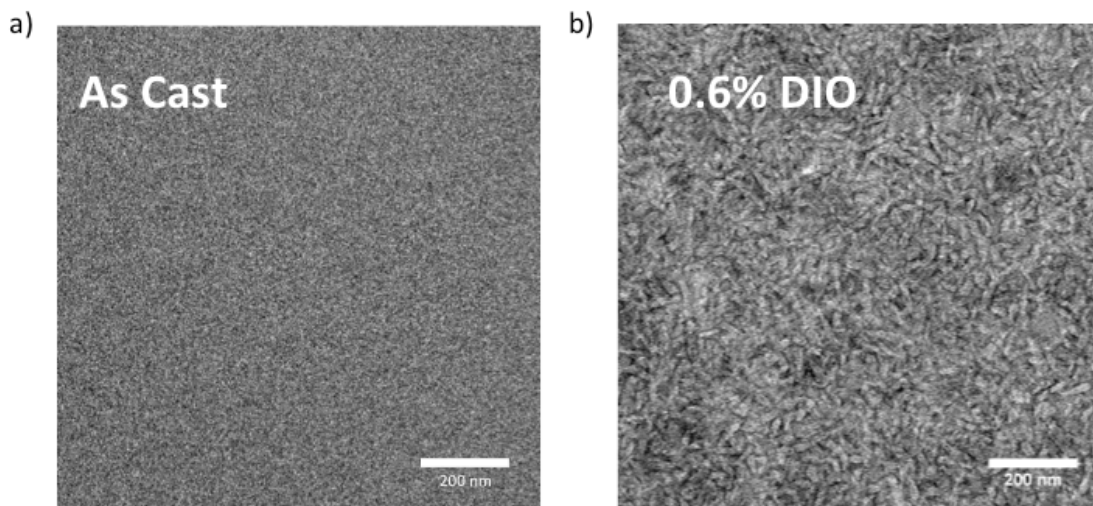
Figure 5.6. Bright field TEM of d-DTS(FBTTh$_2$)$_2$:PCBM blends cast from a) chlorobenzene and b) with 0.6 % DIO

The images from d-DTS(FBTTh$_2$)$_2$:PCBM blends look remarkably similar to those described previously for the proximal analogue. Without additive, blends look well mixed, with no contrast or apparent phase separation. In the blends cast with 0.6% DIO in the solvent, clear grain-like structures can be seen. The bright nature of these features suggests they are donor material, while the darker regions are likely aggregated PCBM regions. It is likely that to improve the *FF* in this system, a finer tuning of the optimization process might be needed; improved crystallinity might be needed as this material has less of a tendency to order. However, in general, the differences between the distal and proximal analogues seem to be quite small and the molecular substitution was relatively innocent. It also suggests that

while solubility and the ability to make thicker films is desirable, it may be in opposition to the tendency to aggregate and crystallize in a film, which is also necessary for good device performance.

5.2.4 Difluorinated FBT

A logical extension to looking at the proximal vs. distal regiochemistry of the fluorine atoms is to also look at devices without fluorines and to add fluorines in both positions. The material with only a benzothiadiazole (BT) unit and no fluorine atoms, that is $DTS(BTTh_2)_2$, has been reported previously. Junxiang Zhang in the Marder group at Georgia Tech synthesized the material in which both positions are fluorines, that is, a difluorobenzothiadiazole unit (F_2BT). The two structures are shown below in Figure 5.9.
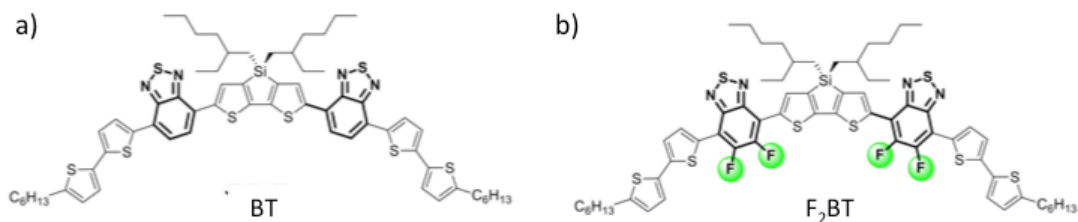
Figure 5.7. Molecular structures of BT and F_2BT highlighting differences in acceptor unit

Removing the fluorine and simply using a BT unit significantly changes the electronic structure of the material. The BT unit has a lower accepting strength than the FBT unit. This is because the C-F bond withdraws electron density from the benzothiadiazole rings, leading to a more electron poor environment. The weaker acceptor character gives rise to a larger bandgap, there is less intermolecular charge transfer, quinoidal character. This can be seen by the blue shifted absorption as seen in Figure 5.8.
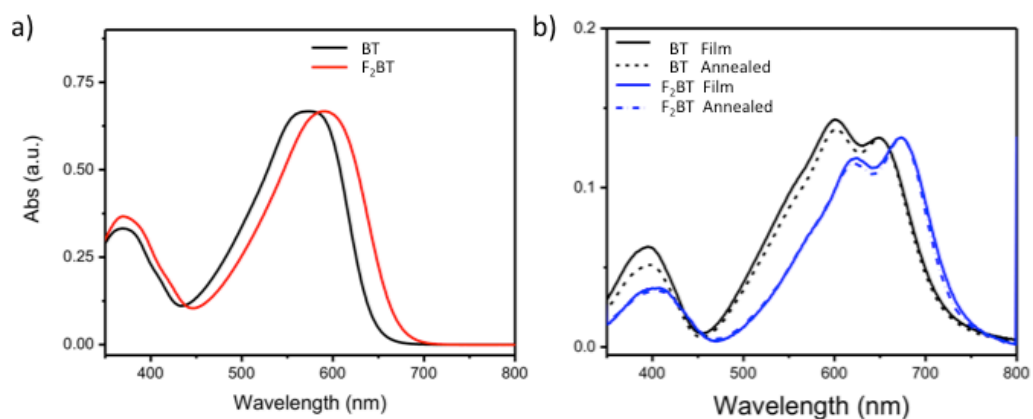
Figure 5.8. a) Solution and b) film absorption of BT and F_2BT molecules

The onset of absorption in solution for the BT molecule shows an increase in bandgap of 50 mV compared to the FBT material as seen in Table 5.3. This phenomenon is exacerbated in film, in which the BT absorption does not show as significant a redshift as the FBT material and the bandgap is 150 mV larger. One might assume that adding a second fluorine unit would increase the acceptor strength of the unit and significantly decrease the bandgap of the material. However, as seen there is little difference in energies between the materials made with FBT and F_2BT units.

Table 5.3. Absorption data of BT, p-DTS(FBTTh$_2$)$_2$ (FBT) and F$_2$BT molecules

	Solution			Film		
	λ_{max} (nm)	λ_{onset} (nm)	E_{gap}	λ_{max} (nm)	λ_{onset} (nm)	E_{gap}
BT	573	653	1.90	600	728	1.70
FBT	590	670	1.85	678	800	1.55
F_2BT	592	680	1.82	673	782	1.58

In fact, the F_2BT material shows very similar absorption characteristics to the FBT based material in the solid state. The absorption onset in solution suggests a 30 mV decrease in bandgap, but in the solid state it is slightly less red-shifted, giving a bandgap of 1.58 eV,

compared with 1.55 eV for the FBT material. There is a strong red-shifted vibronic peak, likely indicating molecular order in the film, much like in the FBT material as well. While the electronics in the solid state for the BT material looks quite different from FBT, the F_2BT shows almost no change, suggesting it may also behave similarly in devices.
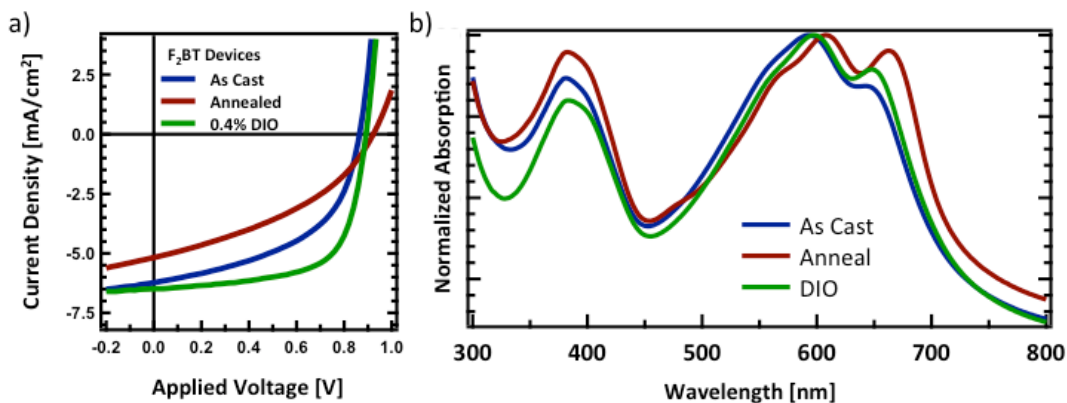
Figure 5.9. a) Current voltage curves of $F_2BT:PCBM$ devices at the same three casting conditions (As cast, annealed, and 0.4% DIO) studied for p-DTS(FBTTh$_2$)$_2$ and b) normalized absorbance curves for the three blend films

Solar cells were again fabricated utilizing PCBM under the same conditions used for the FBT material. The blends were cast from chlorobenzene and left as cast or annealed at 130 °C, or cast with 0.4% DIO. The *JV* curves are shown in Figure 5.9 and device parameters in Table 5.4. As seen, the As Cast device has relatively low performance with a $PCE = 2.7\%$. Casting instead with 0.4% DIO improves the shape of the *JV* curve and improves efficiency to give a $PCE = 3.8\%$. Phenomologically, this is similar to FBT:PCBM devices. However, the initial as cast device with the F_2BT start with higher performance, yet the improvement upon addition of additive is much smaller. Specifically, there is not nearly as large an increase in current with additives as was seen in the FBT devices. This low J_{SC} limits efficiency. Annealing the F_2BT devices actually decreases performance, which might be due to over aggregation based on the large red shift in film absorption. It is encouraging

that the F$_2$BT:PCBM devices show a larger V_{OC} compared with the FBT analogues (892 mV vs. 809 mV) yet have nearly identical bandgaps. However, clearly, the same processing conditions are not quite transferable and would need to be further optimized to achieve high efficiency.

Table 5.4. Solar cell characteristics of three relevant conditions

	J_{SC} [mA/cm^2]	V_{OC} [mV]	FF [%]	PCE [%]
As Cast	5.47	868	48.8	2.68
Annealed	5.13	917	38.8	1.87
0.4% DIO	6.45	892	65.9	3.80

5.2.5 Conclusions

Starting with the high efficiency system, p-DTS(FBTTh$_2$)$_2$:PCBM, two molecular analogues, one in which the fluorine regiochemistry of the FBT unit is changed from "proximal" to "distal" and one in which the FBT unit is changed to a F$_2$BT unit were synthesized and studied. In both cases the materials had similar energy levels, with little change to the absorption profile in solution or film. Both materials seemed to aggregate in the solid state, though not necessarily to the same extent or in the same crystal configuration as in the parent system.

Devices were fabricated under the same conditions as studied with the p-DTS(FBTTh$_2$)$_2$:PCBM system, casting from chlorobenzene, annealing, and adding DIO suing each of the two systems. In each case, additives help in much the same way across all three systems. Both new systems show slightly higher V_{OC} compared with the original system, but do not perform quite as well, being limited by J_{SC} and *FF*. Further optimization

led to a $PCE = 6.5\%$ for the d-DTS(FBTTh$_2$)$_2$ system, while the DTS(F$_2$BTTh$_2$)$_2$ was not optimized further.

5.3 Substitution of a Benzodithiophene Core

As shown, replacing the central electron rich donor unit moving from p-DTS(FBTTh$_2$)$_2$ to p-SIDT(FBTTh$_2$)$_2$, we were able to increase the open circuit voltage and maintain high efficiency. Based on this success, it was thought that insertion of a benzodithiophene (BDT) based core in place of the DTS or SIDT unit could also lead to high efficiencies. BDT is a less electron rich unit than SIDT and thus should push the HOMO level deeper. This unit has been used in high efficiency polymer systems and is know to lead to high open circuit voltages. It also has the benefit of adjustable side chains. In particular, the side chains can be conjugated with the chromophore backbone, leading to additional absorption bands and a broader spectral response.

5.3.1 Two BDT Based Molecules

The two materials described in Chapters 2 and 3 can be defined by the architecture p-[*Donor*](FBTTh$_2$)$_2$ where the [*Donor*] core unit was either DTS (Chapter 2) or SIDT(chapter 3). Two new materials were synthesized in which the [*Donor*] unit was a benzodithiophene (BDT) moiety, each with different side chains. The structures of BDT1 and BDT2 are shown in Figure 5.10.
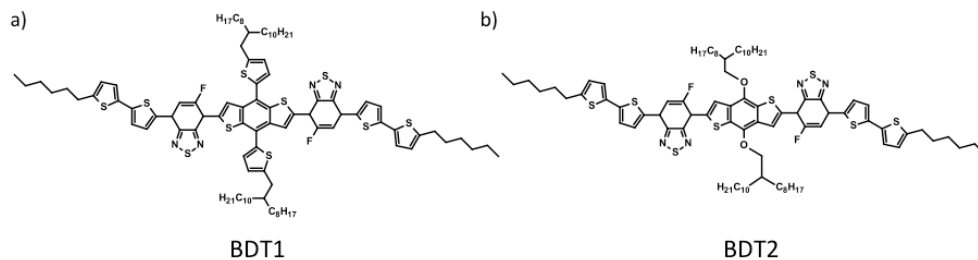

Figure 5.10. Molecular structures of BDT1 and BDT2

126

One of the interesting features of the materials described above are that the side chains are not simply saturated alkyl chains but have conjugation with the BDT core. This is particularly true with BDT1, with conjugation from the thiophene of one side chain, through the core, to the thiophene on other side chain. It was thought that this might lead to broadened absorption by creating an additional absorption band. The absorption of the two materials is shown in Figure 5.11.
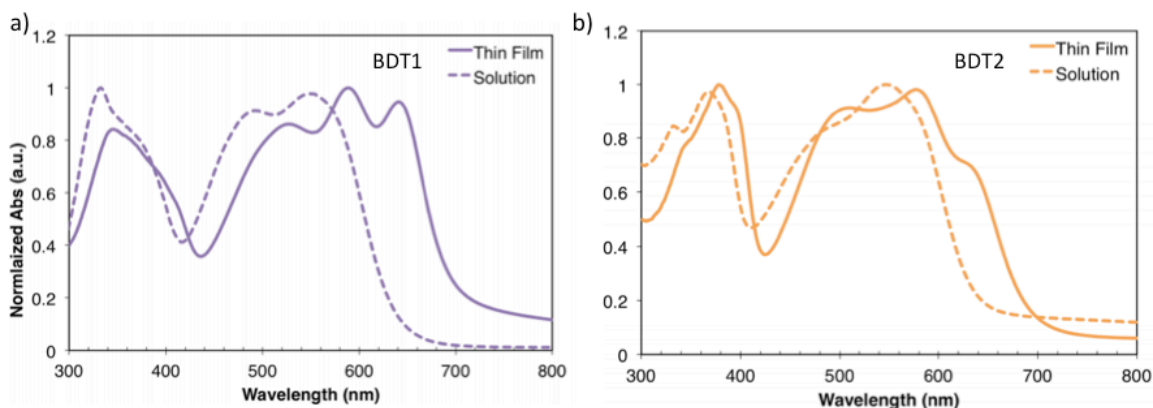
Figure 5.11. Absorption of a) BDT1 and b) BDT2 in solution (dashed) and film (solid)

The two materials show very similar absorption characteristics with solution absorption maxima close to 550 nm and onsets near 650 nm which redshift significantly upon forming a film. In the solid state BDT1 and BDT2 have absorption onsets of 720 nm and 695 nm meaning optical bandgaps of 1.72 eV and 1.78 eV respectively. These are quite similar to what is seen for p-SIDT(FBTTh$_2$)$_2$. This suggests the BDT core does increase the bandgap compared with DTS as expected, and should lead to improved V_{OC}.

In the solution absorption of BDT1 in Figure 5.12a, there are two clear low energy overlapping transitions with peaks close to 550 and 480 nm. There also seem to be overlapping high-energy transitions, which can not be resolved. The multiple transitions are not typical of the other materials studied, and are likely a result of electronically coupled

127

side chains. Upon moving to film, the absorption shifts, and a third low energy vibronic peak emerges; this is likely indicative of order. The result is an incredibly broad, absorption profile. A similar phenomenon is seen for BDT2, in Figure 5.11b.

5.3.2 Blends of BDT1:PCBM

With broad absorption and ordering in the solid state, BDT1 and BDT2 seemed like strong candidates for high efficiency solar cells. Following the work described in Chapters 2 and 3, the material was blended with PCBM and cast from chlorobenzene according to the previously described conditions. Initially, the concentration of DIO solvent additive was adjusted to try to improve performance. The *JV* curves from this optimization are shown in Figure 5.12.
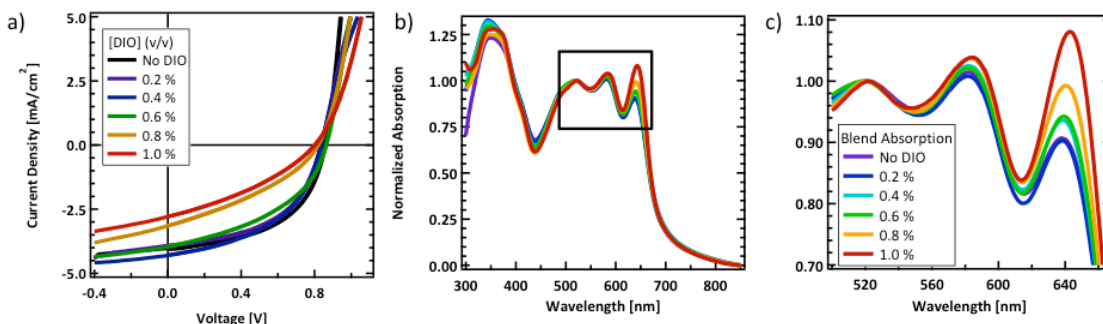
Figure 5.12. a) JV characteristics of blends cast from chlorobenzene with DIO, b) corresponding absorption traces from blend films with a box indicating c) zoomed in absorption showing progression with increasing DIO

Devices cast from pure chlorobenzene showed the best performance with $PCE = 1.8\%$. They show relatively modest $J_{SC} = 4.1\ mA/cm^2$ and $FF = 0.53$ but have a $V_{OC} = 0.86\ V$ showing that the BDT core substitution does improve V_{OC} by almost 100 mV. Adding small amounts of DIO resulted in little change to the *JV* curve and higher concentrations resulted in a reduction in performance.

As opposed to previously studied systems, the absorption of the blend cast from pure chlorobenzene showed the vibronic peak in absorption described in the neat film. This suggests there is ordering and aggregation in the film. Adding DIO does progressively increase the intensity of the peak, suggesting it still helps to crystallize the BDT1 molecule, much like what has been shown previously in the other related systems. To understand what is limiting this system, we employ atomic force microscopy (AFM) to study the morphology of the blend films.
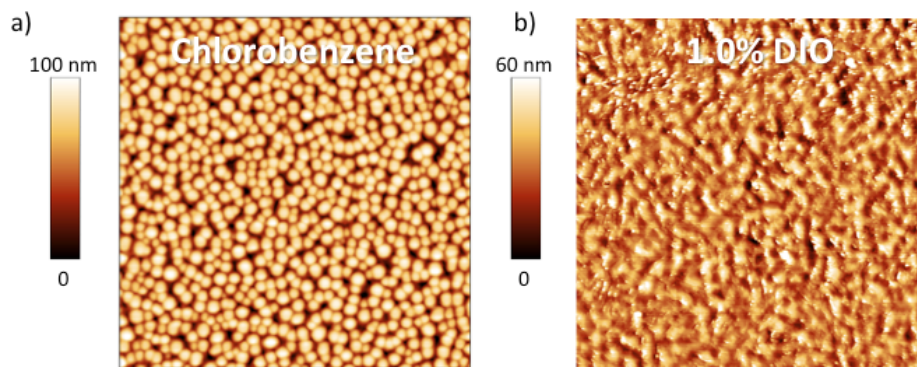
Figure 5.13. Topography images (10 x 10 μm) of BDT1:PCBM blends cast a) from pure chlorobenzene and b) with 1.0% DIO

The AFM of the blend cast from pure chlorobenzene reveals small glob-like structures on the order of 100 nm in radius and 75 nm in height. These domains are not well connected. The low points in the topography scan must be nearly through the entire 120 nm thick film or may indeed be the substrate. When DIO is added to the film, the roughness decreases dramatically. The blobs seem to coalesce quite a bit. However the features remain quite large. It is not surprising these cells do not make good solar cells.

While AFM cannot be used to definitively identify phase separation, it may well indicate a tendency for large-scale aggregation. With that in mind, we sought to make devices using chloroform as the casting solvent. Chloroform has higher volatility than

chlorobenzene and thus allows the film to dry quicker. In the past, systems cast from chloroform have resulted in well-mixed, non phase separated films. The *JV* behavior of devices with blends cast from chloroform is shown in Figure 5.14.
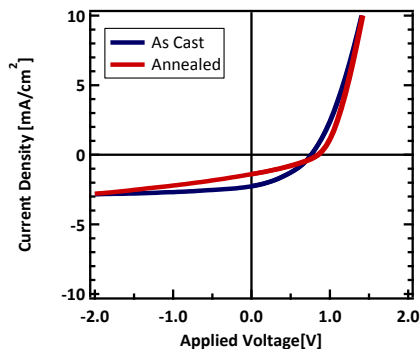
Figure 5.14. JV characteristics of BDT1:PCBM blends cast from chloroform a) as cast and b) after annealing at 110 °C

The blend cast from chloroform made quite bad devices. The device had a $PCE = 0.9\%$. The current was extremely low, with a $J_{SC} = 2.5\ mA/cm^2$. One might imagine that the low current and *FF* could be due to the films having very little phase separation as desired, but also low mobility. This has been seen in other small molecule blends cast from chloroform. In these cases, thermal annealing can lead to vast improvements in efficiency by coarsening the phases, and crystallizing the material. When the BDT1:PCBM blends cast from chloroform were thermally annealed at 110 degrees, the performance became even worse, with a $FF = 0.27$. This suggests there must be something else happening morphologically than what was expected. The morphology of the films before and after annealing was examined by AFM as shown in Figure 5.15.
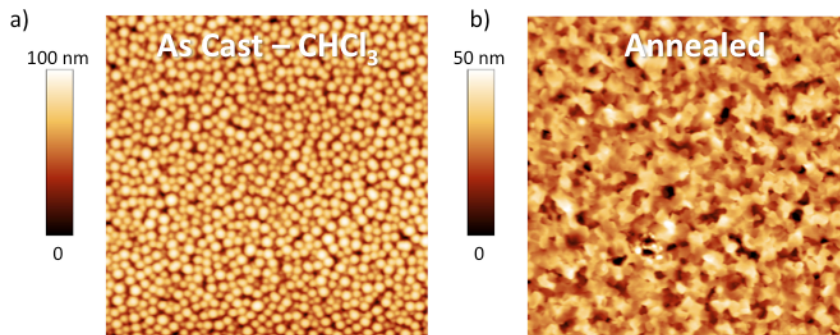
Figure 5.15. Topography images (10 x 10 μm) of BDT1:PCBM blends cast a) from chloroform and b) thermally annealed at 110 degrees

The AFM of the blend cast from chloroform reveals small glob-like structures on the order of 100 nm in radius and 75 nm in height. These domains are not well connected. Although switching solvents changes the drying time of the blend, the size and shape of the features cast from chloroform or chlorobenzene seems to remain the same. When the film is annealed, the features seem to coalesce, forming large, plate-like features that are hundreds of nm large. It is not surprising these films do make good solar cells.

A feature of BDT1, which may jump out as a problem, is the length of the alkyl side chains that adorn the chromophore for solubility. The BDT1 structure uses two octyl-dodecyl branched side chains in addition to the thiophene rings off of the main backbone. This is significantly more alkyl "grease" than in p-DTS(FBTTh$_2$)$_2$, which uses two ethyl-hexyl groups, or p-SIDT(FBTTh$_2$)$_2$, which uses four hexyl chains. One might imagine this increase in non-electronically active material might lead to a loss in charge carrier mobility, which would explain all of the low performance. The mobility measurement of BDT1 is shown in Figure 5.16 and described below.
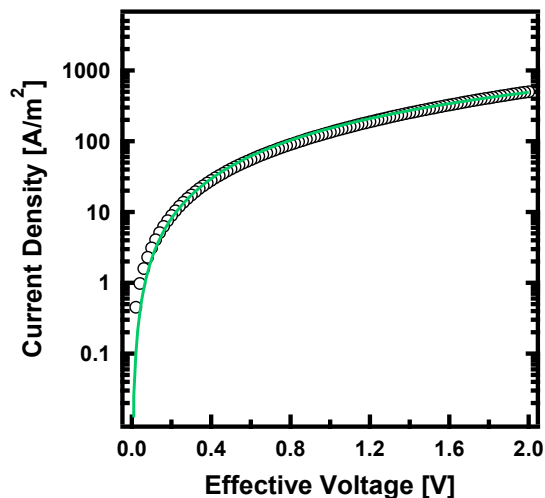
Figure 5.16. JV characteristics of a BDT1 hole only diode fit with a Poole-Frenkel relation

Hole only diodes of BDT1 were fabricated using the structure ITO/BDT1/MoO$_3$/Al in which the MoO$_3$ makes good contact with the HOMO level while the ITO forms a non-injecting contact. The current does not seem to quite fit the space charge limited current model

$$J = \frac{9}{8}\varepsilon_r\varepsilon_0\mu\frac{V^2}{L^3}$$

which is typically used to describe the current flow in a single carrier diode. There seems to be a slight voltage dependence to the mobility such that it does not fit perfectly. To account for this, we invoke the Poole-Frenkel relation, which adds a field dependent term

$$J = \frac{9}{8}\varepsilon_r\varepsilon_0\frac{V^2}{L^3}\mu_0 e^{(\gamma/\sqrt{F})}$$

where F is the electric field and γ is an empirically fit field dependence term. Using this relation and a very small $\gamma = 0.0003$, the mobility is found to be 4.8 $*10^{-4}$ cm^2/Vs. This is similar to what was seen for p-DTS(FBTTh$_2$)$_2$, so this is likely not a problem. It is possible though, that these long alkyl chains help contribute to the tendency for large-scale phase separation.

132

5.3.3 Blends of BDT2:PCBM

When blends of BDT2:PCBM (50:50, 35 mg/mL in chlorobenzene) were cast atop PEDOT:PSS, it was very difficult to make continuous films. Four different solvent additives, diiodooctane, octanedithiol, chloronaphthalene, and diphenyl ether were tested, yet none helped significantly with the dewetting problems; they did not form continuous films. The morphology of the section of film that were left on the substrate and did not dewet, were studied by AFM as seen in Figure 5.17.
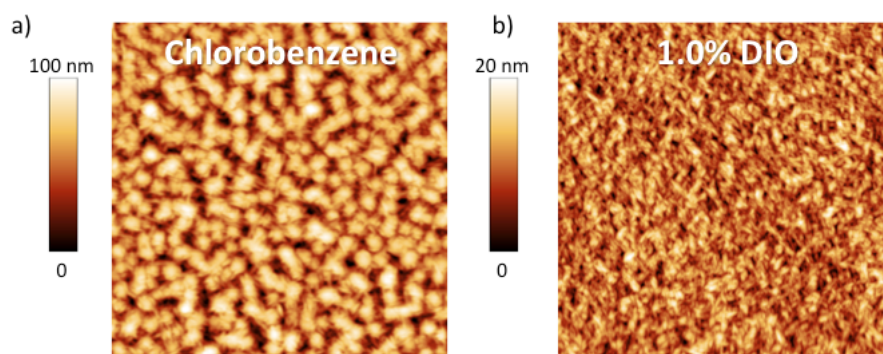
Figure 5.17. Topography images (10 x 10 μm) of BDT2:PCBM blend films cast from a) pure chlorobenzene and b) with 1.0% DIO

The film cast from chlorobenzene shows large, glob-like structures similar to what was seen in the BDT1 system. These are hundreds of nm wide and as high as 100 nm. Using 1.0% DIO results in a much flatter film, though there is are still features on the order of hundreds of nm. These features are examined in more detail via TEM shown in Figure 5.18.
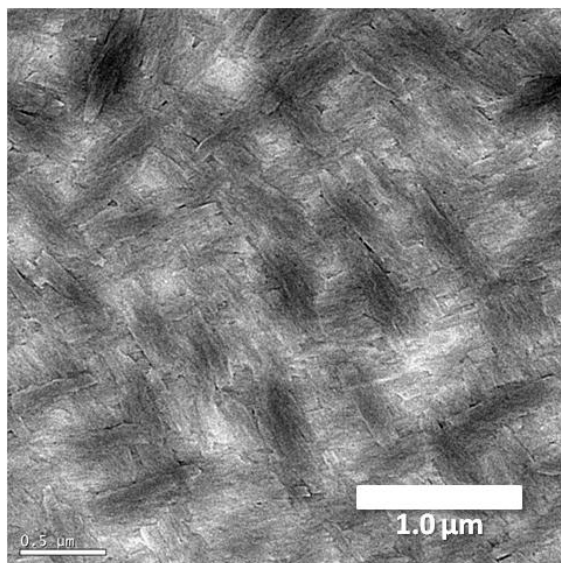
Figure 5.18. Bright field TEM image of BDT2:PCBM blend films cast with 1.0% DIO

The bright field TEM (using a relatively large amount of defocus and a 50 μm aperture) reveals remarkable structure in the BDT2:PCBM films cast with DIO. The dark regions of the film presumably correspond to aggregates of PCBM. The aggregates seem to form oblong shapes. Overlaid with the gross phase separation is the appearance of crosshatched structures. These seem to be crystals of BDT2. They look almost liquid-crystal-like in their large-scale order. The shapes suggest that when the crystals form, they expel PCBM, which aggregates between and next to the high aspect ratio crystals. The crosshatched order extends over microns of film, suggesting a high tendency towards order. This may contribute to the dewetting problems of the film.

5.3.4 Conclusions

This section serves to highlight some of the major challenges with organic solar cells. The two materials described here on first glance, have very similar structures to either p-DTS(FBTTh$_2$)$_2$ or p-SIDT(FBTTh$_2$)$_2$ and make the same type of moiety substitution. The resulting optical and electronic properties seem quite desirable, with broad absorption,

nearly ideal bandgaps and deep lying energy levels. However, high efficiencies were never reached as the morphology of the films proved difficult to control.

The BDT unit has been used in high efficiency polymer systems, and has recently been incorporated into a number of small molecule systems. In fact, the highest performing small molecule to date utilizes a BDT core just like the one used in BDT1.[60,11,143,144] Thus, there are not specific rules as to which units should or should not be used; the combination results in materials properties, which are nearly impossible to predict. There is very likely a set of processing conditions which would lead to high efficiency for these materials systems, or a different acceptor material which may work better than PCBM, but this likely requires a large trial-and-error effort, and cannot be known *a priori*. Such predictive powers could lead to improved materials optimization in the future.

5.4 Use of Electron Withdrawing End caps for Deep Energy Levels

Tremendous multidisciplinary research efforts have led to the ever-increasing efficiency of organic solar cells and have made the technology a bright prospect in the quest for alternative energy.[59,145,146] In particular the rapid development of novel small molecule materials over the last several years has led to great improvements in state of the art efficiency and understanding of structure property relationships.[79,147,148] Their amenability to purification, batch-to-batch reproducibility and monodispersity with well-defined molecular structures make them an attractive alternative to their polymeric counterparts. Also of import are the modular, highly adjustable structures, which lead to energy levels and optical properties that can be finely tuned through molecular design.[18,149]

Most electron donor materials are configured such that the conjugated backbone consists of alternating electron-rich donor (D) and the electron-deficient acceptor (A)

moieties so as to facilitate efficient photo-induced charge transfer and harvest a broad spectral response. One novel push-pull architecture of SMOSCs is linear A-D-A molecular framework prepared by Chen et al., featuring oligothiophene derivatives as central electron-push D units with a variety of electron-pull A units including rhodanine,[10] dicyanovinyl,[150] pyrimidinetrione,[151] indanedione[152] and cyanoacetate (CA).[143] A number of materials based on this concept have achieved high efficiency by tuning the strength and character of these terminal electron-withdrawing groups (EWGs), improving absorption, energetics and molecular interactions.

A second successful molecular architecture introduced by Bazan and coworkers can be described as a D1-A-D2-A-D1 system,[8] where D1 is 5-hexyl-2,2'-bithiophene, (Th2) A is either pyridyl[2,1,3]thiadiazole[9] or 5-fluorobenzo[c] [1,2,5]- thiadiazole (FBT)[61] and D2 can be one of two different electron-rich planar cores, dithienosilole (DTS) or silaindacenodithiophene (SIDT)[153]. Utilizing this push-pull molecular approach, efficiencies up to 9.0% have been achieved.[63] However, there remains room for improvement in these materials, by improving open circuit voltage with deeper energy levels, and reducing the band gap as much as possible to maximize the number of absorbed photons.

To this end, we have modified the previously reported p-SIDT(FBTTh2)2 molecular structure to include electron-poor octyl-cyanoacetate (CA8) end groups, essentially forming a "A1-π-A2-D-A2-π-A1" molecular skeleton. Such substitutions, adding EWGs to the ends of a chromophore, have been shown to effectively reduce the band gap by modulating the position of the LUMO.[18,154] This is the best approach to increasing the light-harvesting

ability of the material while maintaining a deep-lying highest occupied molecular orbital (HOMO) attributed with the high V_{OC}.[34]
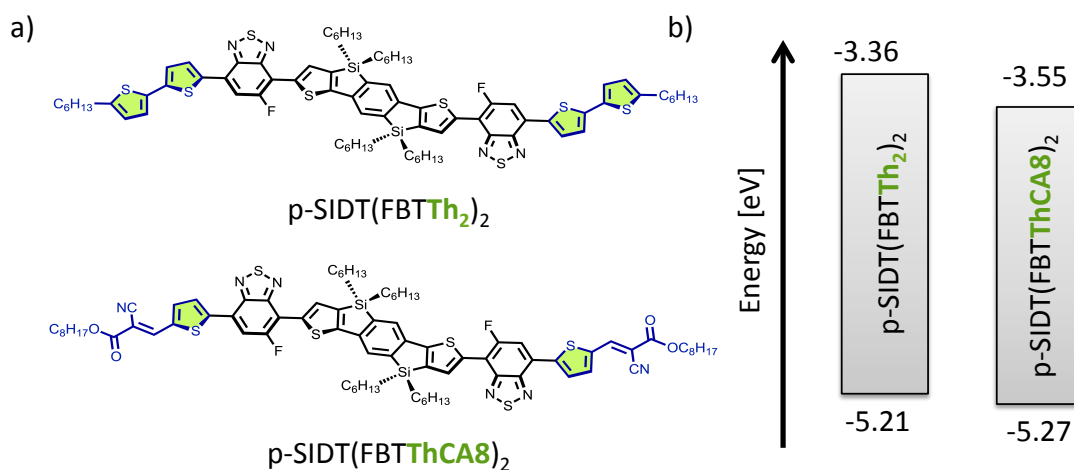
Figure 5.19. a) Molecular structures and b) energy levels of p-SIDT(FBTTh₂)₂ and p-SIDT(FBTThCA8)₂ highlighting the modification of the endgroups

As a starting point, p-SIDT(FBTTh₂)₂ has a relatively wide bandgap (1.8 eV), and shallow lowest unoccupied molecular orbital (LUMO) (-3.4 eV) leading to significant voltage losses upon electron donation to PCBM despite the large V_{OC}; there is much to be gained by reducing this LUMO-LUMO offset. Furthermore, p-SIDT(FBTTh₂)₂ has the desirable tendency to aggregate in the solid state while maintaining good solubility; we attribute this to the presence of the central SIDT fragment, which is highly planar, yet has four hexyl side chains which impart solubility.[66,67,72] Inclusion of the SIDT fragment into the target should retain these properties but with improved electronics.

5.4.1 Molecular properties of p-SIDT(FBTThCA8)₂

The thermal transitions of p-SIDT(FBTThCA8)₂ were evaluated by differential scanning calorimetry (DSC) and compared to p-SIDT(FBTTh₂)₂. A significant impact on thermal behaviors was observed upon substituting 2-hexylthiophene with octyl-

cyanoacetate. As compared to p-SIDT(FBTTh$_2$)$_2$, the melting (Tm) and crystallization (Tc) temperatures of p-SIDT(FBTThCA8)$_2$ are increased by 76.9 and 117.1 °C, respectively (Figure 5.20), which implies an enhancement of the intermolecular interaction in the solid state. This improved rigidity of p-SIDT(FBTThCA8)$_2$ is correlated to a noticeable decrease in solubility, which was measured to be 32 mg/mL for p-SIDT(FBTThCA8)$_2$ compared with over 50 mg/mL for p-SIDT(FBTTh$_2$)$_2$ in chloroform at room temperature.
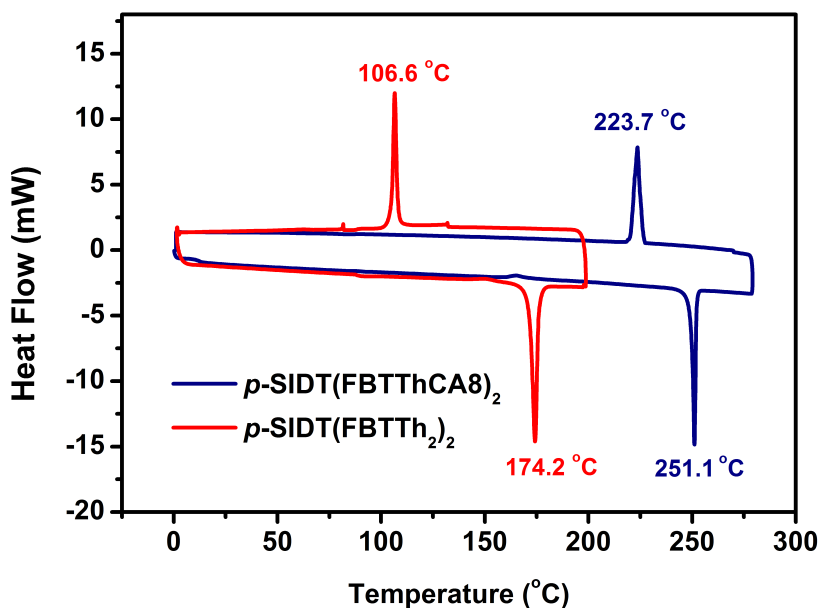
Figure 5.20. DSC thermograms showing melting (T$_m$) and crystallization (T$_c$) temperatures.

Frontier molecular energy levels were estimated by cyclic voltammograms (CV) in dichloromethane and calculated theoretically by density functional theory (DFT). In the CV measurement, energy levels of HOMO and LUMO were calculated from the onsets of oxidation and reduction potentials. The HOMO level (EHOMO, CV: -5.27 eV, E$_{HOMO}$, DFT: -5.43 eV) is quite deep, even compared to that of p-SIDT(FBTTh$_2$)$_2$ (E$_{HOMO,}$ CV: -5.21 eV, E$_{HOMO}$, DFT: -4.97 eV). We anticipate this should provide a high V_{OC}. The band gap of p-SIDT(FBTThCA8)$_2$ is also reduced with respect to p-SIDT(FBTTh$_2$)$_2$ as determined by CV

(1.72 eV and 1.85 eV respectively) and by DFT (1.9 eV and 2.01 eV respectively) suggesting that substituting 2-hexylthiophene with octyl-cyanoacetate on both wing-ends does noticeably reduce the bandgap while maintaining a deep HOMO level.

The normalized solid state absorption profile of p-SIDT(FBTThCA8)$_2$ is shown as the dotted line in Figure 5.21. The film has strong absorption in the visible range, with an onset at 740 nm corresponding to an optical bandgap of 1.7 eV. This is consistent with the bandgap determined electrochemically. The primary absorption band shows vibronic progression, suggesting ordering in the solid state, with peak absorption at 650 nm. The red-shifted absorption of p-SIDT(FBTThCA8)$_2$ with respect to p-SIDT(FBTTh$_2$)$_2$, whose absorption onset in the solid state is at 670 nm, is further confirmation that the addition of electron withdrawing endgroups narrows the bandgap of the chromophore. The shift in absorption onset represents a 28% increase in the number of photons in the AM 1.5 solar spectrum available for absorption. If p-SIDT(FBTThCA8)$_2$ maintains high internal quantum efficiencies and *FF* like its predecessor, and achieves a high V_{OC} as expected, the improved absorption imparts p-SIDT(FBTThCA8)$_2$ with a great potential for high efficiency
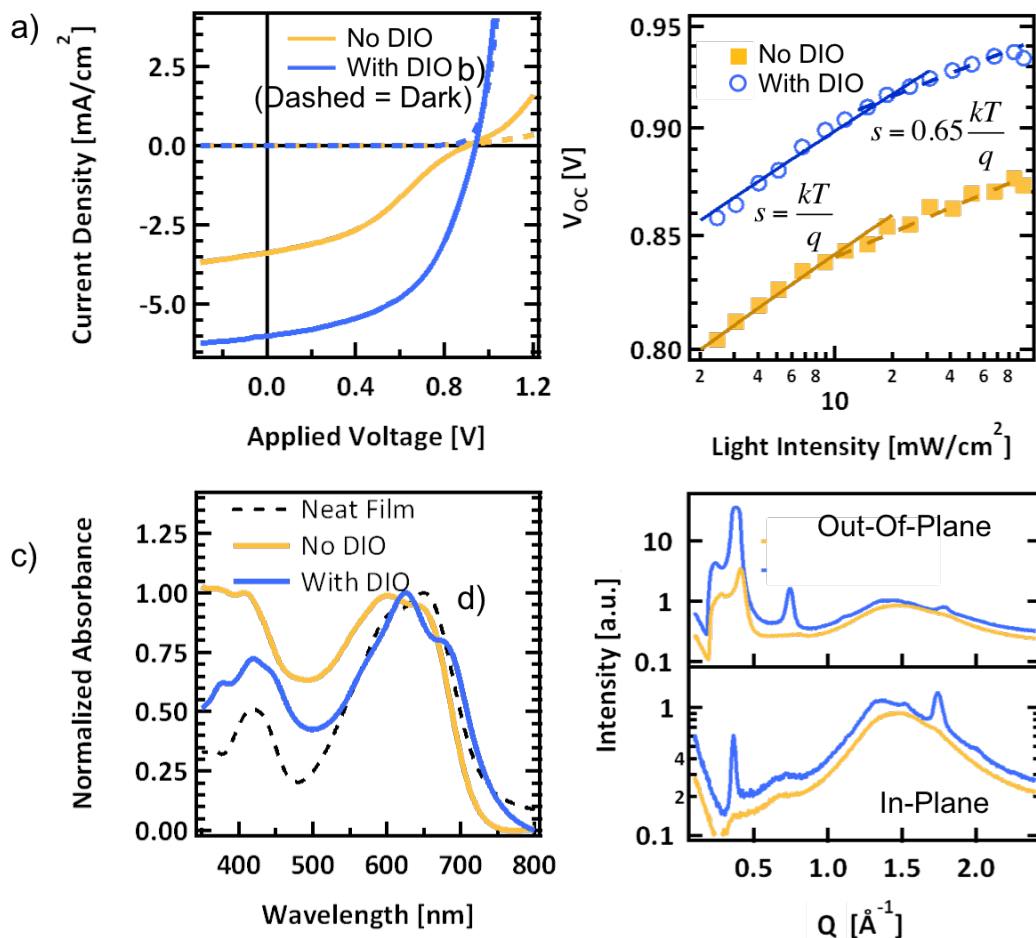
Figure 5.21. a) Photovoltaic performance of p-SIDT(FBTThCA8)$_2$:PCBM solar cells cast from pure chlorobenzene (yellow) and with 1.5% DIO (blue) with b) corresponding light intensity open circuit voltage measurements where the empirically fit solid lines have a slope of kT/q and dashed lines indicate a slope of 0.65 kT/q c) solid state absorption profiles with that of neat p-SIDT(FBTThCA8)$_2$ (dashed line) and d) blend film x-ray diffraction line cuts from crystallites oriented out-of-plane (top) and in-plane (bottom)

5.4.2 Device performance of p-SIDT(FBTThCA8)$_2$:PCBM solar cells

For initial photovoltaic device fabrication, conditions were chosen according to the previously reported protocols of structurally similar small molecule systems. Specifically, p-SIDT(FBTThCA8)$_2$ was mixed with PCBM and cast to form a bulk heterojunction (BHJ) atop poly(3,4-etheylenedioxythiophene) polystyrene sulfate (PEDOT) resulting in an architecture of ITO/PEDOT/p-SIDT(FBTThCA8)$_2$:PCBM/Ca/Al. The ratio of p-

SIDT(FBTThCA8)$_2$:PCBM was held at 50:50 and cast from a chlorobenzene solution containing 40 mg/mL total solids, giving 120 nm thick active layers. Such devices show modest performance ($J_{SC} = 5.0\,mA/cm^2$, $V_{OC} = 0.88\,V$, $FF = 0.35$, $PCE = 1.0\%$). Though the performance is low, it gives a similar efficiency compared to other systems cast from pure chlorobenzene. Furthermore, the high V_{OC} of 875 mV is encouraging, as it further suggests a deep lying HOMO level of p-SIDT(FBTThCA8)$_2$. However, a clear kink in the *JV* curve is visible near the V_{OC} giving the curve a dramatic "s-shape" (Figure 5.21a).

In literature, it has been shown that incorporation of small amounts of the solvent additive 1,8-diiodooctane (DIO) into the casting solvent can vastly improve device performance. Accordingly, initial optimization required adjusting the concentration of DIO. It was found that at a concentration of 1.5% DIO (by volume) in chlorobenzene, the *PCE* was increased to 2.9% ($J_{SC} = 6.0\,mA/cm^2$, $V_{OC} = 0.90\,V$, $FF = 0.55$). Device characteristics are shown in Table 5.5. While the improvements in device performance are relatively modest compared to the dramatic increases that have been observed in some small molecule systems, incorporation of the DIO into the solution reduces the s-shape of the curve leading to a greatly enhanced *FF*. While the use of additives has been shown to have a number of consequences on film formation and device operation, such a dramatic change in curve shape has, to the best of our knowledge, not been demonstrated previously using solvent additives. Thus, while these devices have not yet reached the full the potential of this materials system, we have focused herein on understanding the origin of this improvement in curve shape to gain a better, fundamental understanding of the nature of small-molecule solar cell devices and the role of solvent additives in their operation.

Table 5.5: Device characteristics when cast with and without DIO, before and after treatment with MeOH in a standard architecture as well as in an inverted cell.

Condition		Solar Cell Characteristics			
		J_{SC}	V_{OC}	FF	PCE
No DIO	Standard	3.4	0.91	0.37	1.1
	w/ MeOH	3.4	0.95	0.37	1.2
	Inverted	4.5	1.09	0.51	2.5
w/ DIO	Standard	6.0	0.94	0.52	2.9
	w/ MeOH	6.1	1.02	0.52	3.2
	Inverted	7.0	0.73	0.47	2.4

As a first insight into the origin of the shape change between device with and without DIO, we examined the light intensity dependence of the two devices. Varying the intensity of the incident light serves to proportionally change the number of absorbed photons and thus generation of free charges. Of particular interest is the effect of light intensity on V_{OC}, since at the open circuit voltage carriers are created, but nearly none of the charges are extracted, $J = 0$; all charges must therefore recombine. Thus the relation of V_{OC} with the incident light intensity for bimolecular, free charge recombination has been shown to depend only on temperature and light intensity, given by

$$V_{OC} \propto \frac{kT}{q} \ln (I)$$

Where I is light intensity, k is the Boltzman constant, T is temperature and q is the elementary charge. Thus, in a system dominated by bimolecular recombination, on a semi-log plot of V_{OC} vs. I we expect a linear relationship with a slope of kT/q. It is worth noting that proper analysis of low light intensity data requires sufficiently low dark current, such that it does not constitute a significant fraction of the device current in the voltage regime close to V_{OC}. In both the devices cast with and without additive, even at only 0.02 suns, the dark current remains at least two orders of magnitude lower than the device current (Figure

5.22). The extracted V_{OC} for devices without and with DIO are shown as a function of intensity in Figure 5.21b.
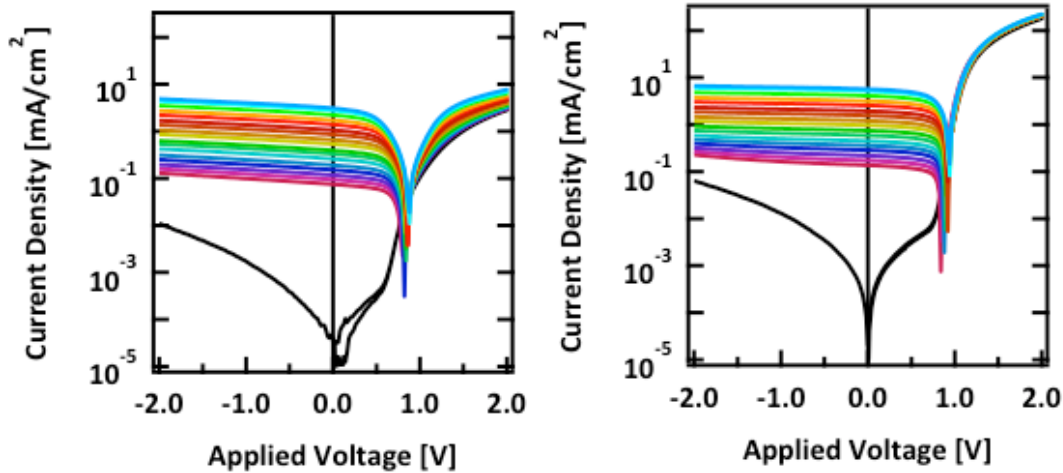
Figure 5.22. JV characteristics as a function of incident light intensity for devices a) without and b) with DIO showing low dark current

It is immediately clear that the V_{OC} in devices without additive do not follow a single linear relationship across all light intensities. Instead it seems to follow a slope of kT/q closely at low light intensities less than 10 mW/cm^2 but then has a shallower, linear dependence with a slope of ~0.65 kT/q at higher intensities. The slope of 0.65 kT/q was fit empirically and does not fit the data unequivocally, but is displayed to show at the very least, that at higher light intensities the V_{OC} has a dependency that is less than the expected kT/q. This suggests that at high charge densities, the dominant recombination mechanism may change. Specifically, a sub-kT/q dependence of the V_{OC} is most often ascribed to the effects of space charge buildup within the film. The device cast with DIO has shows similar behavior but to a much lesser extent. The V_{OC} only deviates significantly at intensities close to 100 mW/cm^2.

To further inspect the effects of light intensity on device operation, the photocurrent, J_{Ph}, defined as the current upon illumination with the dark current subtracted, was examined as a function effective voltage. The effective voltage is the voltage at which no photocurrent is generated minus the applied voltage, $V_0 - V$, and determines the strength of the electric field within the device, and thus the driving force for charge extraction. The J_{Ph} at each intensity is shown for devices cast without and with DIO in Figure 5.23a and 5.23b respectively. At low effective voltages, ($V_0 - V < \sim 0.1V$) implying a small electric field, the photocurrent of both devices linearly increases with voltage. This is due to the competition between drift and diffusion of photogenerated charges to the contacts. In the device processed with DIO, beyond $V_0 - V = 0.2V$ the JPh reaches a regime, where it increases much less significantly with voltage. In this saturation regime, the larger electric field can effectively sweep out charges and bimolecular recombination does not play as significant a role. The voltage at which this rollover point occurs is independent of intensity.
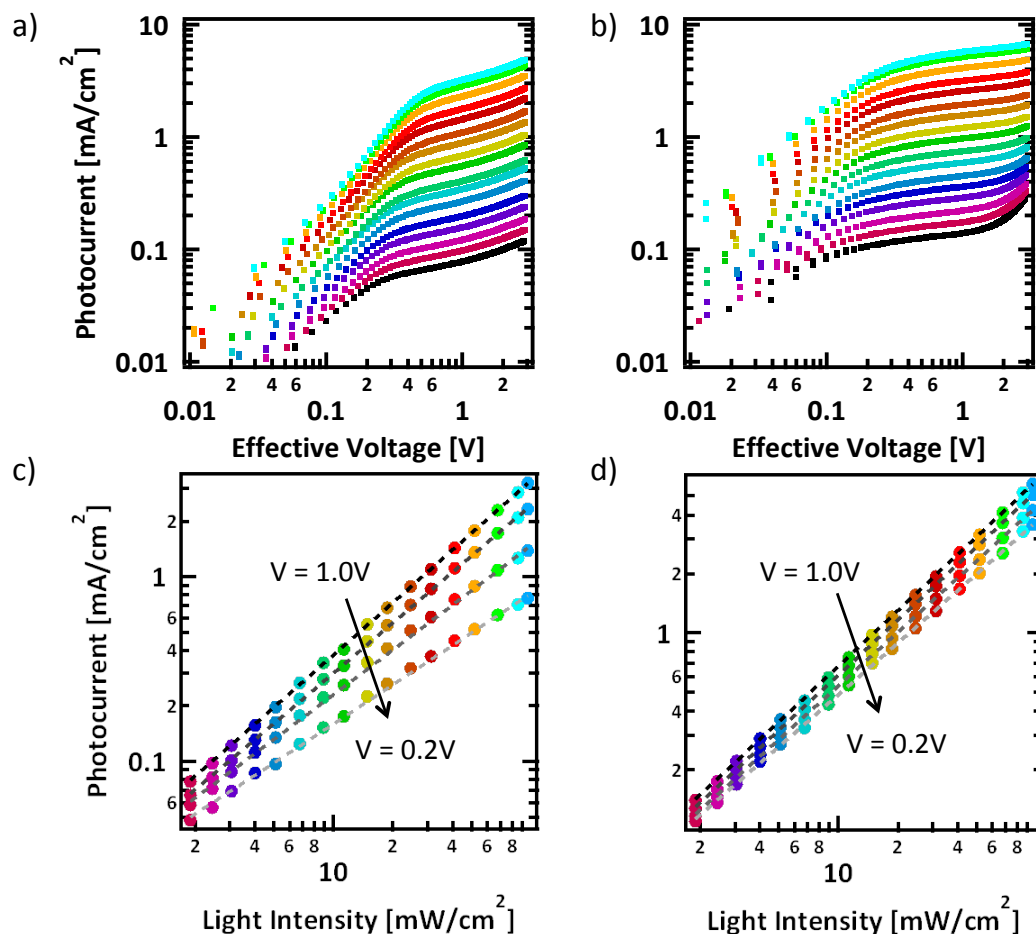
Figure 5.23: Light intensity dependence of photocurrent as a function of the effective voltage, V0-V, for devices cast a) without DIO and b) with DIO and the extracted photocurrent at effective voltages of 1.0, 0.5, 0.3, and 0.2 V (from black to grey respectively) as detailed in Table 5.6 for devices cast c) without DIO and d) with DIO

As shown in Figure 5.23a, JPh has a much stronger dependence on voltage in devices processed without the incorporation of DIO. Even at high effective voltages, there remains a strong voltage effect and the J_{Ph} continues to increase, rather than truly saturate. There are two clear regimes with two different voltage dependencies, but in contrast to devices processed with DIO, in this case the voltage at which JPh switches from one regime to the other does depend on light intensity. At higher intensities, a higher voltage is required to

reach the "saturation" regime. This has also previously been associated with a build up of space charge in the film.

It is expected that for devices not limited by extraction, J_{Ph} at each and every effective voltage, should scale linearly with intensity, $J_{Ph} \propto I$, while devices limited by space charge build-up have been shown to characteristically have a sub-linear dependence, where $J_{Ph} \propto I^{0.75}$. At $V_0 - V = 0.2V$, close to short circuit conditions, in both the devices with and without additive, JPh scales nearly perfectly linearly, following a power law where $s = 0.95$. This relation deviates from linearity when moving to lower fields particularly in the devices cast without DIO. As seen in Table 5.6, at an effective voltage of 0.3V, $s = 0.81$ and by 0.2V, $s = 0.71$. This is quite close to scaling as 0.75, the value one would expect for a device limited by space charge.

Table 5.6: Power law dependences of photocurrent on light intensity at specific effective voltages for BHJ devices from Figure 5.23.

Condition	Power Law Dependence			
	0.2 V	0.3 V	0.5 V	1.0 V
No DIO	0.71	0.81	0.91	0.95
With DIO	0.88	0.91	0.94	0.95

At low fields, the device processed without DIO suffers from space charge build up, while at higher fields, there is sufficient driving force to overcome these effects and extract the charges. A similar effect can be seen in the device processed with DIO, albeit to a lesser extent. At $V_0 - V = 0.2V$ in the optimized device, $s = 0.88$. This suggests again that while the DIO does not completely remove the problems associated with charge extraction, it significantly reduces the magnitude of the effects, removing the dramatic s-shape of the curve.

5.4.3 Morphology Characterization of p-SIDT(FBTThCA8)$_2$:PCBM films

Changes in device performance upon addition of solvent additives are typically ascribed to improvements in the BHJ nanostructure. Often this is related to controlling the crystallization and phase separation processes within the blend; additive helps induce crystallinity in the donor material. Grazing incidence wide-angle x-ray scattering (GIWAXS) was used to probe the crystallization behavior of the blend system with and without additive. The full 2-dimensional GIWAXS spectra from the two blends are shown in Figure 5.24, while line cuts showing Q_z ("out-of-plane") and Q_{x-y} ("in-plane") are shown in the top and bottom plots of Figure 5.21d respectively.
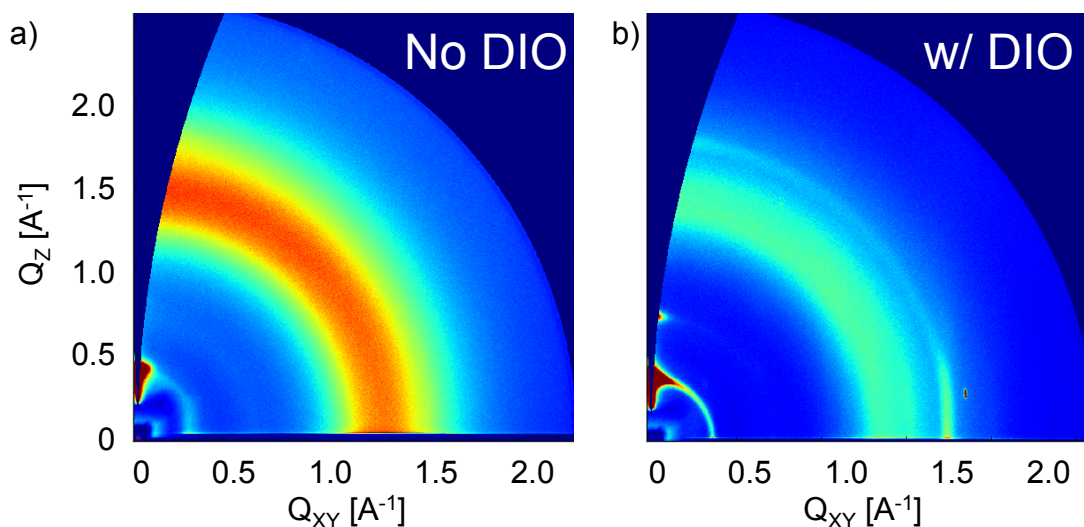
Figure 5.24. Grazing incidence wide angle x-ray scattering profiles of BHJ films cast with and b) with DIO showing intensity as a function of both reciprocal distance, Q and angle, χ.

The broad feature centered at $Q = 1.5\ \text{Å}^{-1}$ which is seen at all orientations in both films is attributed to the isotropic scattering of PCBM. Looking first at the out of plane diffraction in the top panel of Figure 5.21, the BHJ film cast with no DIO shows a prominent peak at $0.37\ \text{Å}^{-1}$. This corresponds to a real-space distance of 1.7 nm. While attempts to grow single crystals of this material have thus far been unsuccessful, by convention we

attribute this to an "alkyl stacking peak," that is a spacing arising from molecules separated by alkyl chains analogous to the lamellae stacking in P3HT (i.e. (100) planes). In the film cast with DIO, this peak is more prominent suggesting a greater degree of crystallinity. There is also a peak at 0.74 Å^{-1}, which corresponds to the second order reflection. There is even a small bump at 1.11 Å^{-1}, which likely corresponds to third order reflection, suggesting a quite well ordered film. Additionally, there is a small peak at 1.79 Å^{-1}, corresponding to a spacing of 3.5 Å, which we attribute to π - π stacking.

Looking next at the traces from the Q_{x-y} direction, that is from crystallites oriented in the plane of the substrate, there are no discernible features from p-SIDT(FBTThCA8)$_2$ in the BHJ film cast without DIO. In the film processed with DIO, the alkyl stacking peak is again visible at 0.37 Å^{-1}, though not as intense as in the out-of-plane direction. The π-stacking peak is more prominent in-plane at $Q = 1.74$ Å^{-1}, or a slightly expanded spacing of 3.6 Å^{-1}. Assuming the alkyl and π-stacking directions are perpendicular, this suggests the material primarily adopts an edge-on orientation. This is in contrast with the preferential "face-on" orientation adopted by p-SIDT(FBTTh$_2$)$_2$, demonstrating how sensitive molecular self-assembly can be to relatively small molecular design choices. However, consistent with previous reports of related molecules, DIO does seem to improve crystallinity.

Despite the differences in crystallization, this does not give a clear indication as to the root cause of why one device shows signs of space charge and a resultant s-shape in *JV* curve while the other does not. The phenomenon of DIO inducing crystallization has been observed before. One might expect that the increase in crystallinity has a profound effect on the hole mobility in the blends, and space charge buildup may occur due to imbalanced carrier mobilities in the device processed without DIO. However, the hole mobilities for

blends processed without DIO and with 1.5% DIO are 4.5×10^{-5} and 9.2×10^{-5} cm^2/Vs respectively, each slightly lower than the neat hole mobility of p-SIDT(FBTThCA8)$_2$, which is found to be 2.0×10^{-4} cm^2/Vs. Although the mobility indeed increases with DIO processing, a mobility increase by a factor of two is not particularly significant and should not lead to such drastic changes in curve shape. These mobilities are lower than what is found for related high performance systems, which will likely always limit the system to a relatively low *FF*.
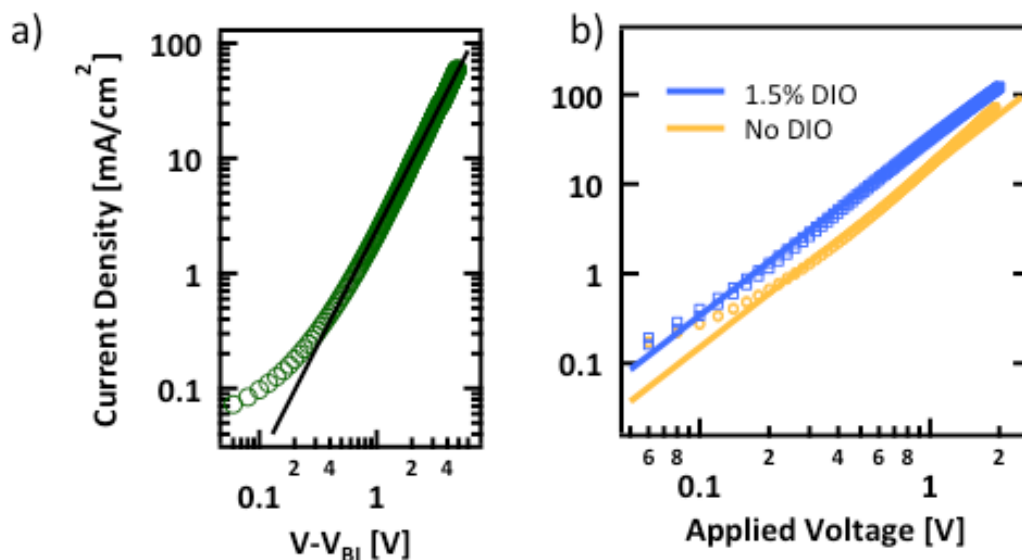
Figure 5.25. Mobility measurements of a) neat p-SIDT(FBTTh$_2$)$_2$ and b) blends of p-SIDT(FBTTh$_2$)$_2$:PCBM cast without (gold) and with (blue) DIO

Despite the relatively high V_{OC}, based on the CV data, one would expect to achieve voltages that are even higher compared with p-SIDT(FBTTh$_2$)$_2$, as p- SIDT(FBTThCA8)$_2$ seems to have an even deeper HOMO level. However, a HOMO of -5.27 eV is close to the work function of the PEDOT interfacial layer, which is used. Thus, it may be limiting the voltage, making non-ohmic contact with the active layer. It has recently been shown that in some cases, when PEODOT limits the voltage in solar cells, casting methanol on top of the

layer will improve efficiency. The methanol has been show to effectively deepen the work function of the anode layer while not significantly disrupting the morphology. It was thought that this non-ohmic contact may lead to an extraction barrier, which could lead to the s-shape in the curve. We employed this technique to improve the voltages in p-SIDT(FBTThCA8)$_2$:PCBM cells and look at the effects on curve shape.
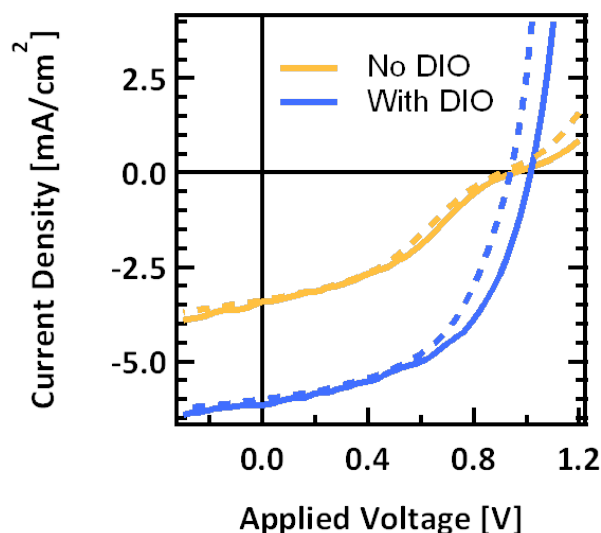
Figure 5.26: Current voltage curves for devices cast from pure chlorobenzene (gold) and with 1.5% DIO (blue) with (solid) and without (dashed) methanol treatment

After treatment with methanol, the V_{OC} increases to 1.01 V for devices processed with DIO. A similar improvement in V_{OC} is also seen for devices cast from chlorobenzene, though the s-shaped kink in the *JV* curve near open circuit remains. Treatment with methanol has little effect on J_{SC} or *FF* thus we suspect there is no significant change in morphology but strictly an improvement in electrical contact due to a deeper work function.

5.4.4 Vertical Phase Separation in p-SIDT(FBTThCA8)$_2$:PCBM solar cells

Non-ideal vertical phase separation, that is to say, enrichment of donor material at the cathode or acceptor at the anode has also been identified as a potential cause of s-kinks in *JV*

curves. Acceptor material at the PEDOT interface, for instance, can act as a barrier to hole extraction, leading to ineffective sweep out and a buildup of holes. To examine the vertical separation behavior of the two blends dynamic secondary ion mass spectrometry (DSIMS) was employed. In DSIMS, a sample is bombarded with ions, ablating ionized material, which is analyzed using a mass spectrometer. The composition of the ablated material is monitored as the beam mills through the thin film, resulting in a depth profile. To improve contrast between the two materials, Deuterated fullerene PC61BM-d5 was used as a surrogate for PCBM to establish a unique mass signal for the fullerene component. Thus detection of deuterium in the mass spectrum implicitly signifies PCBM in the film. Likewise, the amount of p-SIDT(FBTThCA8)$_2$ was monitored by the occurrence of nitrogen atoms in the mass spectrum. Unique signatures for each material help make discerning relative concentrations simple and accurate. The DSIMS profiles of the two systems are shown in Figure 5.27.
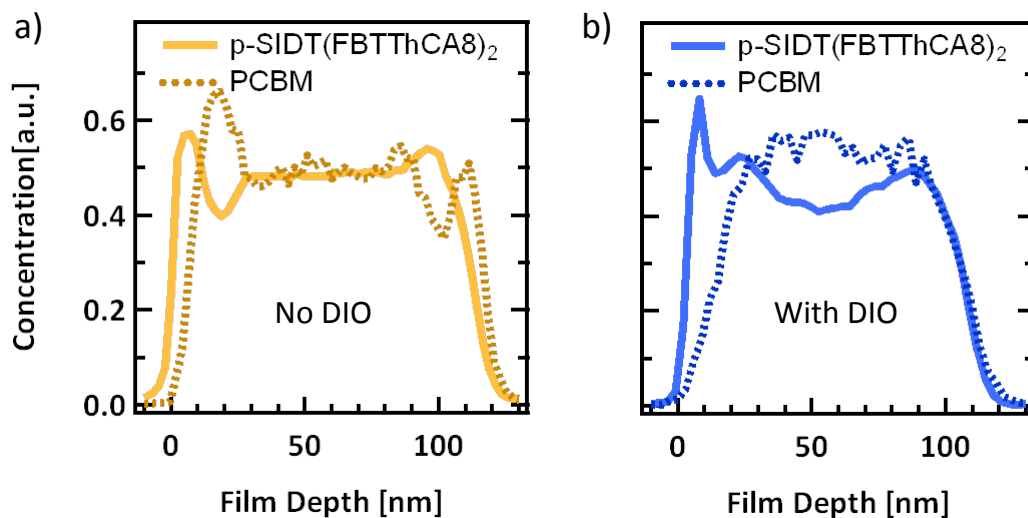

Figure 5.27: DSIMS profile showing scaled nitrogen (solid) and deuterium (dashed) signals for films cast a) with no DIO and b) with 1.5% DIO

As the DSIMS profile is collected, time corresponds to film depth, as the beam ablates material at a constant rate. Thus the x-scale is a measure of depth into the film, and has been scaled for film thickness. The turn-on of the nitrogen and deuterium signals corresponds to the top surface of the films, what would be the cathode interface in a device, the turn-off of the signals thus corresponds to the BHJ/PEDOT interface. The absolute intensity of the two signals given by the instrument cannot be compared directly due to different instrumental sensitivity, thus each signal is scaled to an average composition of 50% based on the weight ratio used in the blend solutions. It is important to monitor how the signals evolve relative to each other as the beam penetrates into the film.

Looking first at the BHJ processed without additive, when the signals first turn on, there is initially an enrichment of p-SIDT(FBTThCA8)$_2$ immediately followed by a depletion of donor and an enrichment of PCBM. This corresponds to donor material preferentially accumulated on the top surface. Throughout the bulk of the trace the concentration of the two materials remains nearly constant. At the PEDOT interface, x = 115 nm, the PCBM signal has a small peak while the p-SIDT(FBTThCA8)$_2$ signal begins to drop off. This suggests there is an enrichment of PCBM at the anode surface. Such an arrangement, with donor at the top surface and acceptor at the bottom, is non-ideal for the standard device architecture.

Processing with DIO has a significant effect on the vertical phase separation. At the top surface there is again an enrichment of the p-SIDT(FBTThCA8)$_2$, evidenced by a faster turn on than the PCBM signal. There is a slight depletion of the p-SIDT(FBTThCA8)$_2$ through the bulk of the device. At the bottom surface, the two signals overlap, suggesting an even distribution of p-SIDT(FBTThCA8)$_2$ and PCBM. The vertical phase separation is not ideal,

as there remains an enrichment of p-SIDT(FBTThCA8)$_2$ at the cathode interface, however, DIO helps overcome the problem of PCBM concentrated at the anode interface.

The high concentration of PCBM at the anode helps explain the s-shape behavior of the *JV* curve for the devices processed without additive. The low concentration of p-SIDT(FBTThCA8)$_2$ near that interface reduces the surface recombination velocity of holes within the device; reduced surface recombination results in a piling up of charges near the anode, which creates a space charge effect in the device. This helps explain the anomalous V_{OC} and J_{Ph} light intensity data. The effect is most apparent at low fields and high carrier concentrations i.e. near open circuit conditions and at high light intensities.

If the s-shape seen in devices cast from chlorobenzene is in fact due to an enrichment of PCBM at the bottom interface, an inverted device architecture should result in an improvement in curve shape. The inverted architecture has the cathode as the bottom contact and anode on top. Thus if the vertical separation in the BHJ remains in an inverted structure, the PCBM-rich phase would be at the cathode interface, and p-SIDT(FBTThCA8)-rich phase at the anode interface. However, it is not necessarily true that the observed phase separation will remain in inverted devices, as fabrication requires casting atop a different substrate with different surface energetics, which may play a role in determining film formation.

While the active layers were cast in the same way, the inverted devices employed the architecture ITO/ZnO/PEIE/p-SIDT(FBTThCA8)$_2$:PCBM/MoO3/Al where PEIE refers to polyethylenimine ethoxylated. The cathode was cast from a sol-gel of zinc acetate, and thermally converted to ZnO in air as described in literature. A thin (10 nm) layer of PEIE has been shown in the past to improve contact by reducing the work function of a ZnO

surface, and was prepared as reported. The *JV* characteristics of the inverted devices are shown in Figure 5.28.
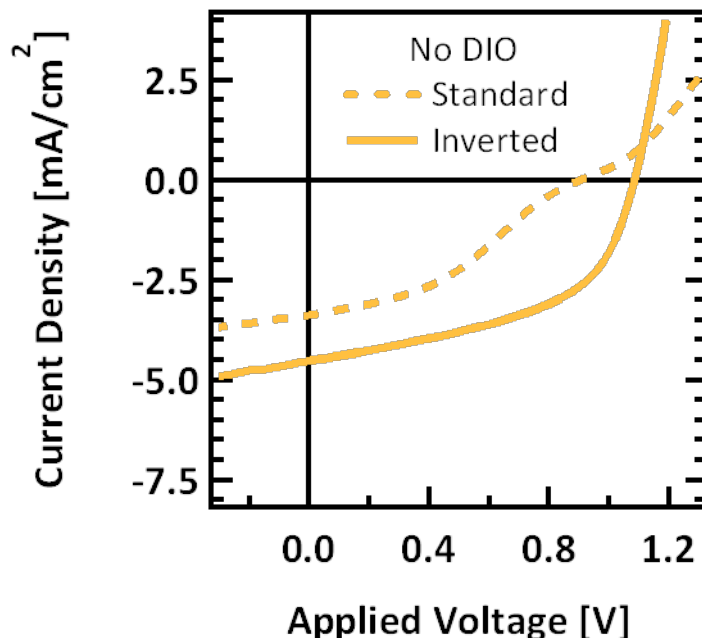

Figure 5.28. As Cast device in standard (dashed) and inverted (solid) architecture

It is clear, using an inverted architecture does indeed fix the s-shape of the curve for films cast from pure chlorobenzene without DIO. They achieve much higher efficiency ($J_{SC} = 4.5\ mA/cm^2$, $V_{OC} = 1.09\ V$, $FF = 0.51$, $PCE = 2.5\%$) than in the standard architecture. While the performance is still modest, there is a marked improvement in the shape of the *JV* curve. The device achieves a high open circuit voltage with no sign of space charge buildup. All device parameters improve. While we cannot be completely sure the morphology of this film is identical as when it is in a standard architecture, as the film is indeed thinner (70 nm), in conjunction with previous data, this is a strong indication that the primary cause for the s-shape is indeed non-ideal vertical phase separation. While there was not a strong s-shape to the curve when devices were cast with DIO, one still might expect

the non-ideal phase separation seen by DSIMS would result in improved performance in the inverted architecture (Figure 5.29).
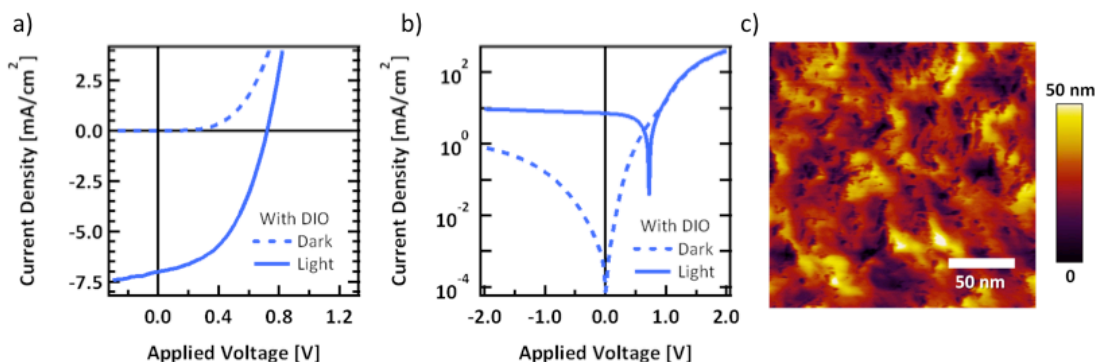

Figure 5.29. JV characteristics on a a) linear and b) log scale showing inverted devices cast with DIO in the dark (dashed) and under illumination (solid) showing the high leakage current due to a very rough film as determined by c) AFM topography of a 70 nm thick film

Unfortunately, when the optimized 1.5% DIO condition was used they showed very high dark current in the inverted structure, leading to low performance. This leakage current is likely due to a change in morphology when casting atop ZnO instead of PEDOT. The film is quite rough (Figure 5.29c) with some pinholes reaching nearly all the way to the bottom of the 70 nm thick film. The high dark current results in the decrease in V_{OC} and FF and thus a lower overall efficiency. However, near short circuit conditions (when the leakage current is low) there is in fact significantly more photocurrent in the inverted devices than standard, suggesting the vertical profile may still exist in the inverted structure. This also provides hope that through further optimization using the inverted architecture, we may be able to improve the top efficiency.

5.4.5 Conclusions

In conclusion we have developed a new molecular donor material p-SIDT(FBTThCA8)$_2$ based on the inclusion of electron withdrawing endcaps within a

155

previously reported high performance material. The structural modification had the desired effect of reducing the band gap for extended absorption spectrum while maintaining a low-lying HOMO level to achieve very high V_{OC}. It was necessary to cast methanol atop the active layer to deepen the work function of PEDOT and fully access the high V_{OC} up to 1.01 V. The energy levels are nearly ideal for incorporation into BHJ devices with PCBM, maximizing voltage and spectral coverage, but despite the structural similarity to previously reported materials, blends of p-SIDT(FBTThCA8)$_2$ and PCBM did not have device performance akin to its predecessors when processed in the same manner. Specifically, when cast from chlorobenzene, the resulting JV curve gives rise to a significant s-shape, resulting in extremely low FF and PCE. Through light intensity studies, the s-shape in the curve has been attributed the build-up of space charge due to reduced surface recombination. The use of DIO as a solvent additive helped remove the s-shape character from the JV curve and improve performance up to $PCE = 3.2\%$.

Analogous to what has been reported in literature, DIO helps to induce crystallinity of the p-SIDT(FBTThCA8)$_2$ in the blend as evidenced by GIWAXS and a commensurate red-shift in absorption. However, lack of crystallinity is not typically associated with the s-shape in the JV curve seen when cast without additive. Blends cast from chlorobenzene still have reasonably high mobility, so a build-up of space charge due to an imbalance in carrier mobilities can be ruled out. Instead, the differences in curve shape are ascribed to changes in the vertical phase separation. Without additive there is a enrichment of PCBM at the PEDOT:BHJ interface as evidenced by DSIMS. Subsequently, the low concentration of p-SIDT(FBTThCA8)$_2$ at the anode likely leads to reduced surface recombination, a build-up of space charge and ultimately, and s-kink in the JV curve. The inclusion of DIO helps

reduce the concentration of PCBM at the anode improving surface recombination, and *JV* characteristics. Although the performance of this materials system is not on par with the state of the art without further device engineering, this drastic change in curve shape is important in understanding the nature of solvent additives and their effects on solution processed BHJ devices

5.5 Instability Using a PT Acceptor Unit with a SIDT Core

As described in Chapter 2, p-DTS(FBTTh$_2$)$_2$ was designed based on a structurally similar molecule containing a pyridylthiadiazole (PT) unit in place of the FBT unit Although the overall efficiency improved moving from PT to FBT, the slightly weaker electron accepting character of the FBT unit led to a blue shift in absorption compared to p-DTS(PTTh$_2$)$_2$ but had a similar V_{OC}. Thus, it is reasonable to imagine that starting with p-SIDT(FBTTh$_2$)$_2$, the high V_{OC} material that was the focus of Chapter 4, replacing the FBT units with PT units should lead to a red-shifted absorption while maintaining the high V_{OC}. This reasoning led to the synthesis of the molecule p-SIDT(PTTh$_2$)$_2$ which is shown below in Figure 5.30 with the PT units highlighted in blue.
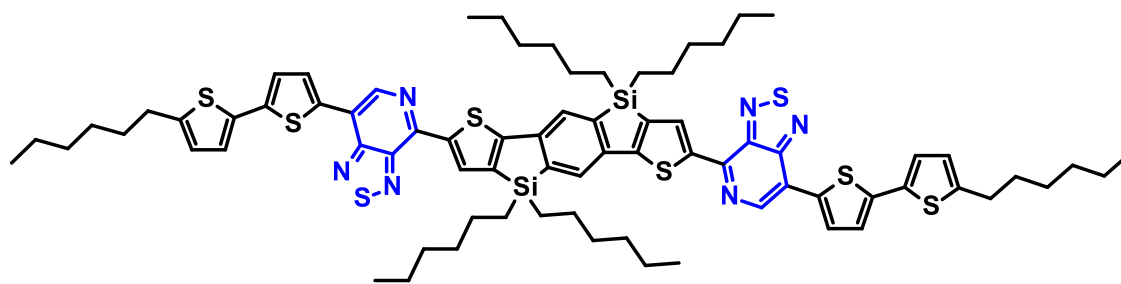

Figure 5.30. Molecular structure of p-SIDT(PTTh$_2$)$_2$ highlighting the PT acceptor moieties

157

5.5.1 Initial Screening of p-SIDT(PTTh$_2$)$_2$ For Solar Cell Applications

The absorption of the PT containing molecule is compared in Figure 5.31 with the absorption of the FBT containing material described previously. Indeed, substitution to the PT unit does induce a red-shifted absorption with an onset of $\lambda = 720\ nm$ in solution and $\lambda = 720\ nm$ in film. This indicates a solid-state bandgap of 1.63 eV, a nearly 200 mV reduction compared with the FBT analogue. In this region of the solar spectrum, such a redshift represents a nearly 30% increase in the number of available photons and thus great potential for high efficiency, if indeed a high V_{OC}, FF, and EQE are maintained.
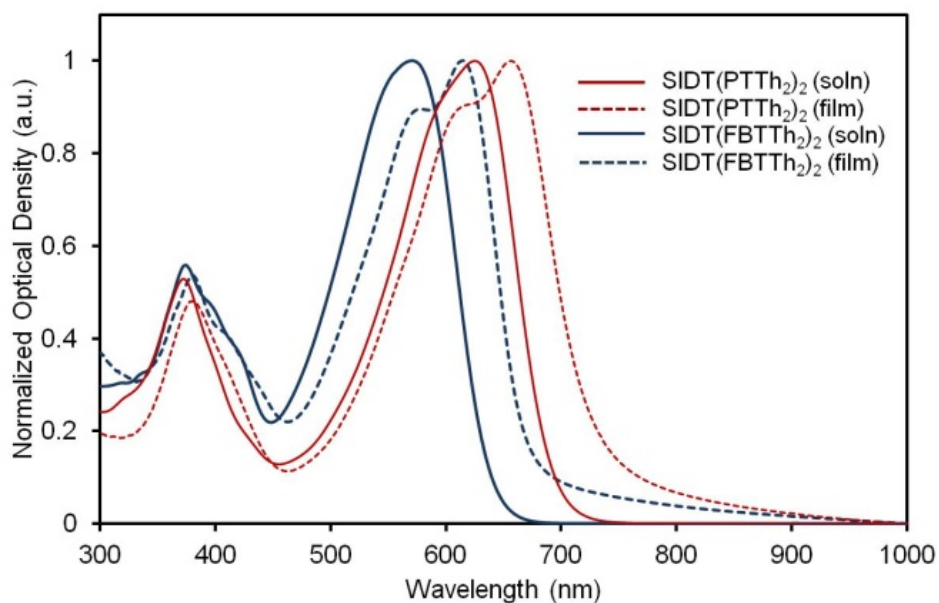
Figure 5.31. Optical density of solutions and films of PT and FBT analogues

Despite the extreme structural similarity to p-SIDT(FBTTh$_2$)$_2$ and p-DTS(PTTh$_2$)$_2$, in initial screenings p-SIDT(PTTh$_2$)$_2$ did not show any promise as a donor material in bulk heterojunction solar cells. Cells were made using MoO$_3$ bottom contacts to prevent interaction of the PT unit with the PEDOT interlayer, but were fabricated in the same way as with previous materials. Cast from pure chlorobenzene in a blend with PCBM, the cells

behaved much like in other systems, with low FF and J_{SC}, and a $PCE = 0.7\%$. The low performance in other systems has been attributed to a lack of phase separation. With previous molecules, addition of the solvent additive DIO drastically improved the efficiency by inducing crystallization and phase separation. However, in p-SIDT(PTTh$_2$)$_2$:PCBM blends, addition of DIO did not help. All devices showed extremely low FF and J_{SC}. It is worth noting that the V_{OC} of the PT based material is quite similar to that of the FBT analogue, which further confirms that this moiety substitution does result in a reduced bandgap but maintains deep energy levels. The JV curves are shown in Figure 5.32 along with the equivalent conditions using p-SIDT(FBTTh$_2$)$_2$ blends.
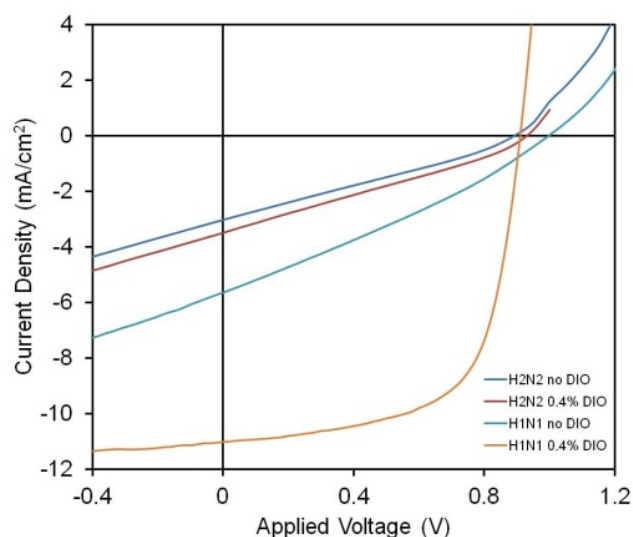
Figure 5.32. Current voltage characteristics of devices cast with and without 0.4% DIO for both PT and FBT containing analogues

The low performance could be due to unfavorable morphology, which may be corrected through processing, or unfavorable electronics, which may be inherent to the molecule or blend. Due to the extremely low performance, regardless of processing, it seemed likely there might be a fundamental problem with the donor material rather than simply an unfavorable morphology.

159

5.5.2 Hole transport in p-SIDT(PTTh$_2$)$_2$

One common explanation for low FFs in solar cells is poor charge carrier mobility in the blend, leading to increased bimolecular recombination. Typically, PCBM has relatively high electron mobility, and does not limit devices to such low *FF*. The hole mobility of small molecule blends however, can vary greatly, depending on processing and molecular structure. The upper limit for mobility in a blend with small molecules is typically set by the mobility in the neat material. Thus we first looked at the hole mobility of neat p-SIDT(PTTh$_2$)$_2$ in the diode configuration ITO/ p-SIDT(PTTh$_2$)$_2$/MoOx/Al. As described previously the development of space charge within a diode leads to current having a squared dependence on voltage and a cubic inverse dependence on layer thickness; that is

$$J \sim V^2/L^3$$

However, the diode mobility data of neat p-SIDT(PTTh$_2$)$_2$ does not fit the simple SCLC model. The *JV* characteristics of three p-SIDT(PTTh$_2$)$_2$ devices of different thicknesses are shown in Figure 5.33 along with a p-SIDT(FBTTh$_2$)$_2$ device for comparison, which does fit SCLC, and has a mobility of $\mu_p = 1.2 \times 10^{-3} \, cm^2/Vs$. The three p-SIDT(PTTh$_2$)$_2$ devices showed extremely low current and had a much stronger voltage dependence than $J \sim V^2$. The p-SIDT(PTTh$_2$)$_2$ devices showed almost no built in voltage, and the current had a stronger thickness dependence than $J \sim 1/L^3$. Thus, the SCLC model is clearly not appropriate to describe hole transport in p-SIDT(PTTh$_2$)$_2$.
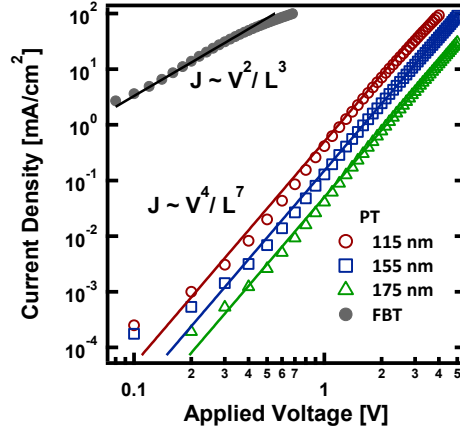
Figure 5.33. Current voltage characteristics of three hole-only diodes of p-SIDT(PTTh₂)₂ of various thicknesses with a device made with the FBT analogue for comparison

The SCLC model assumes trap-free transport. It has been shown by Blom and coworkers among others, that if trap states are introduced within the bandgap, the current in a diode will be reduced, and adopt a stronger voltage and thickness dependence. The magnitude of the effects depends on the trap density and energetic depth of the trap states.

$$J = N_C q\mu \left(\frac{\varepsilon_0 \varepsilon}{q N_t e^{E_{tc}/kT_t}}\right)^r \left[\left(\frac{2r+1}{r+1}\right)^{r+1} \left(\frac{r}{r+1}\right)\right] \frac{V^{r+1}}{L^{2r+1}}$$

where N_C is the effective density of states (DOS), N_t is the total concentration of trap states, E_{tc} is the energy difference between the trap level and characteristic energy related to the DOS that mimics the role of the conduction band edge, T_t is the trap temperature which is a characteristic parameter describing the shape of the trap distribution, and $r = T_t/T$. Thus, without knowing the number, nature, or depth of the trap states, the trap-limited current can still be expressed more simply as

$$J \sim V^{r+1}/L^{2r+1}$$

Using this equation, the data from Figure 5.33 was fit empirically with $r = 3$. This gives a voltage dependence of $J \sim V^4$ and a thickness dependence of $J \sim 1/L^7$. This seems to fit all three thicknesses, though could be refined if devices of larger thickness were made.

161

However, it is clear that the material shows trap limited transport. This is likely what is limiting the solar cell devices in *FF* and J_{SC}. In solar cells, traps lead to a trap-assisted recombination mechanism first described by Shockley Reed and Hall in which one charge is stuck in a trap and recombination depends on an opposing charge encountering it. These traps seen in p-SIDT(PTTh$_2$)$_2$ likely are leading to an increase in recombination, which explains the extremely low performance.

5.5.3 Nature of traps and breakdown of p-SIDT(PTTh$_2$)$_2$

Electronic trap states within a material are often attributed to synthetic defects or impurities present in materials. Studies have shown that even at impurity levels as low as 1:10,000, traps can significantly affect *JV* characteristics. Thus purification of material is incredibly important. One major advantage of small molecules is that they can be purified using common organic chemistry protocols such as flash chromatography or recrystallization; polymers due not have such a luxury. However, such stringent purity requirements necessitate sensitive analytical instrumentation. It has been shown previously that some side products that are present in such small quantities so as to be below the limit of detection by ^{1}H NMR can still cause large harm to device performance.

Field desorption ionization mass spectrometry (FDI-MS) provides an incredibly sensitive technique for analyzing material. The FDI-MS spectrum of p-SIDT(PTTh$_2$)$_2$ upon initial synthesis and after months of storage are shown in Figure 5.34. In the initial spectrum the only masses seen are 1400.4 and 700.2 m/z corresponding to the M^{1+} and M^{2+} ions of H2. However, in the spectrum taken of the material actually used to make devices, that is, after months of storage in air, there are additional mass peak at 1017.9 and 1085.4 m/z. It seems this material had degraded over the months since it was initially synthesized.
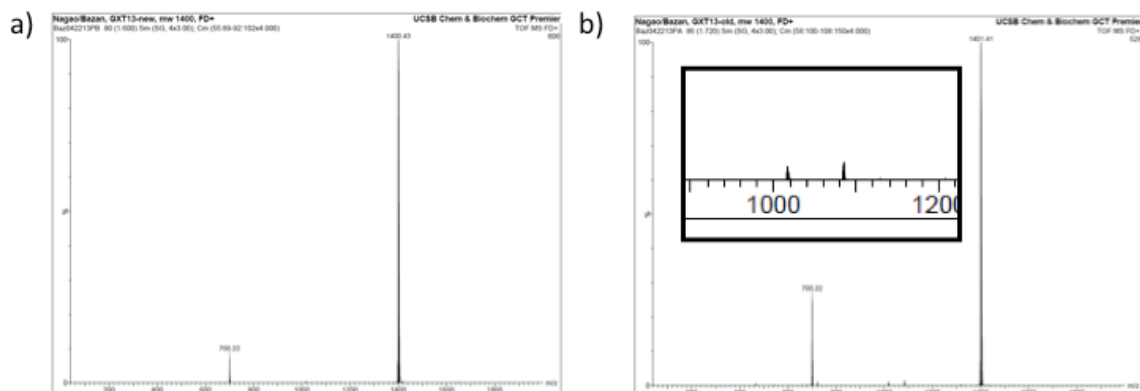
Figure 5.34. Mass spectrum of p-SIDT(PTTh₂)₂ a) upon initial synthesis and purification, and b) after several months of storage with inset showing additional peaks

The m/z ratio of 1018 could be attributed to a fragment in which one of the PT-SIDT bonds is cleaved, leaving the core with only one "wing." The proposed degradation product is shown below.

exact mass = 1017.4
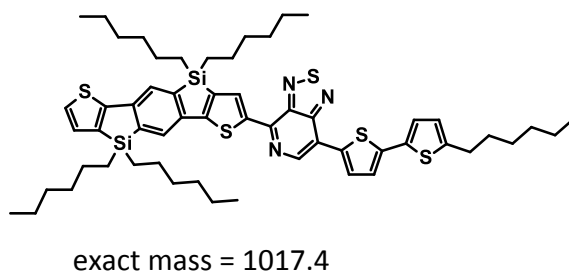
Figure 5.35. Possible degradation product in which SIDT-PT bond is cleaved

While this by no means definitively identifies the degradation product, there is clearly a degradation product that occurs, and unless it is a multiple charged species, has a lower mass than the initial molecule. Furthermore, it seems reasonable that the PT-SIDT bond may lead to the degradation, as neither the FBT for PT substituted analogue or the DTS for SIDT containing analogue show any stability issues. The PT-SIDT bond is the only bond unique to this material. Finally, for an impurity to act as a hole trap, it must have an electronic state within the bandgap of the host material. This means an upward shift in HOMO level towards

the vacuum level, despite a likely increase in bandgap due to reduction in conjugation length. This would indeed occur when reducing the intermolecular charge transfer characteristics by removing a donor–acceptor bond.
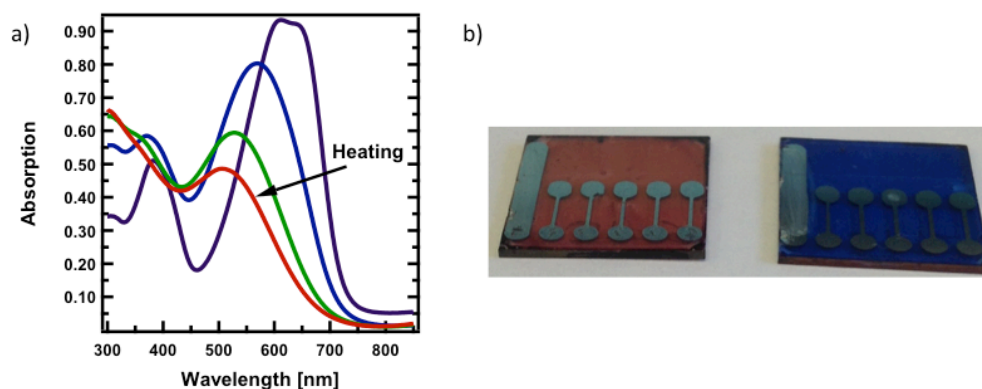

Figure 5.36. a) Absorption spectra of p-SIDT(PTTh$_2$)$_2$ films as a function of heating at 200 degrees b)photograph showing color difference

One would expect that cleaving a bond in the molecular backbone would reduce the conjugation length, and likely result in a change in color. Heating a film of p-SIDT(PTTh$_2$)$_2$ in air indeed results in a large blue shift in absorption and change in spectral shape, suggesting the backbone is susceptible to oxidation. This is still, of course, very indirect proof of what might have happened in the material, but may give some insight into what molecular design choices are to be avoided.

5.5.4 Conclusions

A new molecule, p-SIDT(PTTh$_2$)$_2$ was synthesized in order to combine the deep HOMO level instilled by the SIDT unit and the reduced bandgap which comes with incorporation of the PT unit. The two directly related materials in which the PT unit is replaced with an FBT unit or where the SIDT unit has been replaced by a DTS unit have both been reported and show high efficiency. Such substitutions are the basis for Chapters 3

and 4 and previously worked quite well, so it was not bizarre to think this material would be successful following similar protocols.

The absorption properties of p-SIDT(PTTh$_2$)$_2$ are quite red-shifted compared to the FBT containing analogue, making available 30% more photons, making the material quite promising. When blended with PCBM in solar cell devices, the V_{OC} was indeed high, suggesting deep energy levels, but efficiencies were incredibly low due to low current and *FF*.

Using hole only diodes, we were able to determine that the material had electronic traps present. These mid-gap states cause trap-assisted recombination, and can limit the performance of a solar cell. Traps are often a result of impurities, so FDI-MS was used to analyze the p-SIDT(PTTh$_2$)$_2$ material. Indeed, in the months between final purification and device fabrication, the material had degraded. Based on the mass to charge ratio, we suggest it might come from cleavage of the PT-SIDT bond, the only bond unique to this material. While further analysis of the degradation is needed, this may suggest certain pairs of functionalities be avoided in molecular design.

5.6 Designing a Donor Material with Multiple Absorbing Units

While most of the previous studies have focused on improving the energetics to get a better tradeoff between optical band gap and V_{OC}, a second methodology to improve *PCE* is simply absorbing more light via broadband absorption, as most small molecules have relatively narrow, discrete absorption bands. Broad absorption may be achieved by coordinating different chromophores within a single molecule. This strategy has been successfully applied to oligothiophenes, with dye units as end caps.[11,148,10] In these examples, the dye units extend the conjugation length, and therefore adjust the electronic

165

structure of the entire molecule. In this contribution we examine a different design strategy, which is based on integrating independent absorbing units at two ends of a symmetric core. Figure 5.37 shows the specific molecule p-DTS(FBTTh$_2$FBTTh)$_2$ or AT1 for short.

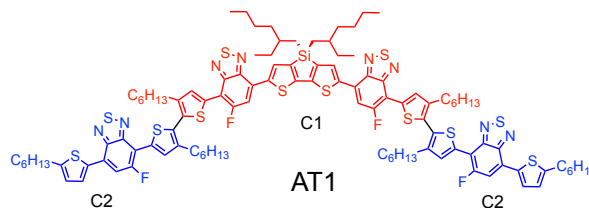*Figure 5.37. Chemical structure of p-DTS(FBTTh$_2$FBTTh)$_2$, referred to as AT1*

The central chromophore C1 (red) is linked on both sides with chromophore C2 (blue). Although C1 and the two C2 units appear on paper to be conjugated, it was anticipated that they would absorb nearly independently as a result of the molecular topology, namely the twist in the conjugated backbone from steric interference between the hexyl side chains on the internal thiophene units. It also seemed reasonable that the internal core of AT1 would have the lowest energy transition and would determine the highest occupied molecular orbital (HOMO) energy level, due to the extended conjugation length and the presence of the electron-rich DTS unit.

5.6.1 Molecular properties of AT1

Thin film cyclic voltammetry (CV) measurements show oxidation and reduction waves from which we estimate that the HOMO and lowest unoccupied molecular orbital (LUMO) energies are −5.29 and −3.14 eV, respectively, corresponding to a band gap of 2.1 eV (Figure 5.38). These data indicate that the frontier molecular orbitals of AT1 are very similar to those of p-DTS(FBTTh2)2, suggesting that the levels are primarily determined by the C1 core.[61]
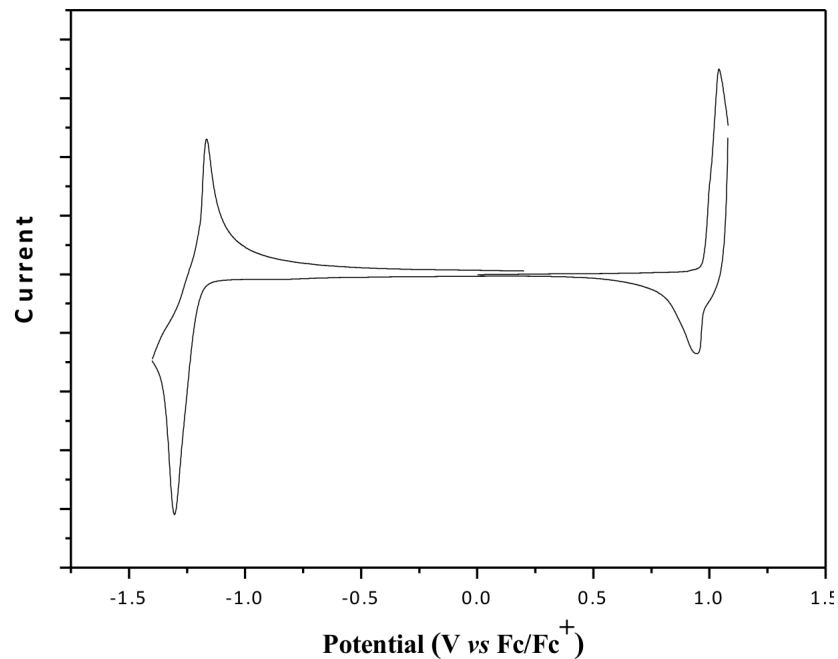
Figure 5.38. Thin film cyclic voltammetry plot of AT1.

Figure 5.39a shows that the absorption spectrum of AT1 in chlorobenzene (CB) exhibits an onset of absorption (λonset) at 664 nm, corresponding to an optical band gap of 1.9 eV, and a broad absorption maximum (λmax) at ~575 nm. These features are similar to those of p-DTS(FBTTh2)2; however, in AT1 a second absorption band is discernible as a shoulder at ~475 nm. This second band is reasonably attributed to absorption of the C2 chromophores, effectively broadening the range of absorption, compared with C1 alone.
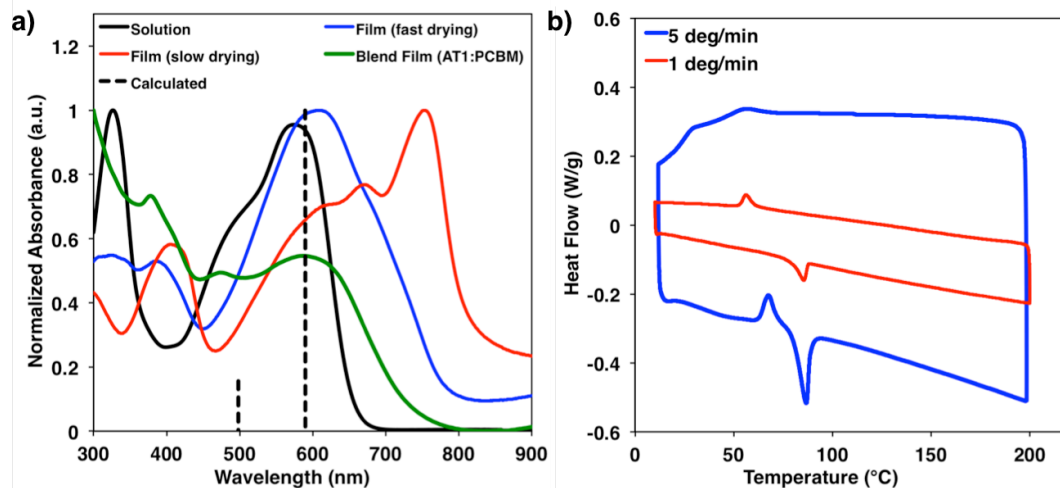
Figure 5.39. (a) Absorption spectra of AT1 in solution and films at different drying rates. Dotted vertical lines represent calculated transitions. Also shown is the spectrum from a 60:40 AT1:PCBM blend film cast from CB and DIO. (b) DSC scans at two different speeds

Density functional theory (DFT) calculations were employed using CAM-B3LYP/6-31G(d,p).[155,156] The minimum energy structure of AT1 was calculated to have a dihedral twist angle of 57° between the two internal thiophenes.

Figure 5.40. Top-down and side-on view of the lowest energy conformation of AT1.

Time-dependent DFT studies were completed using a dielectric similar to CB to determine excitation energies, and the calculated spectrum matches well with the

168

experimentally determined spectrum (Figure 5.39a).[157] Natural transition orbitals show that the transition around 480 nm is mainly from C2 groups and the transition at 590 nm arises from C1 almost exclusively. Therefore, the twist angle of 57° effectively breaks electronic communication between C1 and C2.
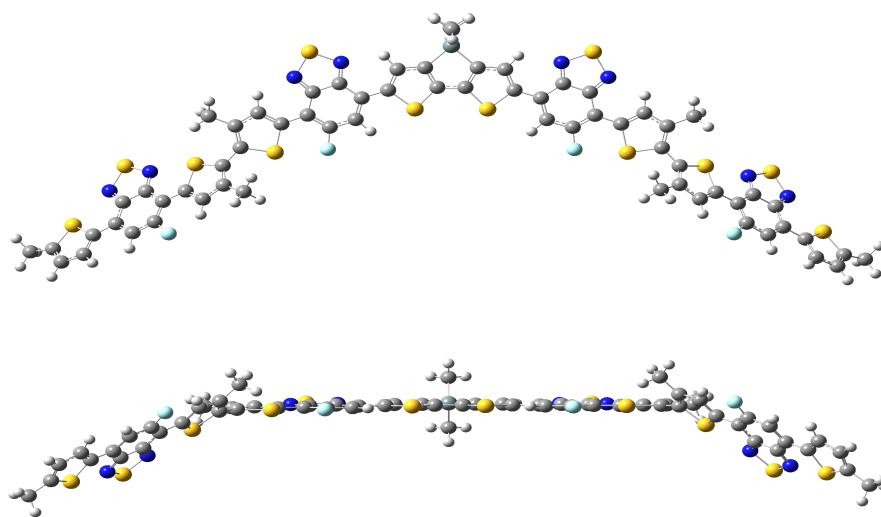
5.6.2 Kinetic drying of AT1

Figure 5.39a also shows that the absorption of AT1 films exhibits a large red shift compared to solution. The features are dependent on the evaporation rate of the CB. When spin-cast for 60 s and allowed to dry under nitrogen, λ_{max} = 620 nm. A broad, ill-defined shoulder peak appears at low energies that shifts λ_{onset} to 775 nm. A significantly different absorption is observed if the film is allowed to dry slowly in a closed Petri dish containing CB vapor. These conditions lead to shifts of λmax to 760 nm and of λonset to 825 nm (band gap = ~1.5 eV). The sharpness of these features suggests increased molecular order relative to the as-cast samples and highlights the influence of processing history.[31]

Differential scanning calorimetry (DSC) measurements of AT1 were performed at different heating rates (Figure 5.39b). At a rate of 5 °C/min, a cold crystallization is observed at 67 °C during the heating cycle, followed by a melting transition at 87 °C. No recrystallization peak is observed upon cooling. At the slower rate of 1 °C/min, a distinct melting temperature of 85 °C is observed with no indication of cold crystallization. However, upon cooling at the slower rate, the emergence of an exothermic peak at 56 °C was observed, identified as crystallization from the melt. Both the UV–visible absorption and DSC data therefore indicate that AT1 has a substantial resistance to crystallization.
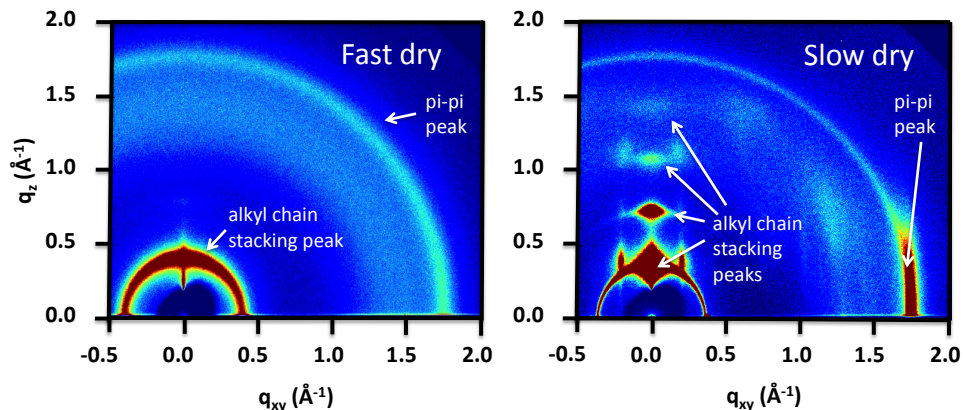
Figure 5.41. GIWAXS profiles of as-cast films of AT1 spin coated from CB solution for 10 seconds (a) slow drying (b) fast drying.

Grazing incidence wide-angle X-ray scattering (GIWAXS) was used to probe changes in AT1 ordering; see Figure 5.41. The GIWAXS pattern of the fast-dried film exhibits two isotropic peaks at approximately q = 0.37 and 1.77 Å–1, corresponding to d-spacings of 17.0 and 3.5 Å, respectively. We assign the higher q reflection as the π–π stacking peak and the lower q reflection as an "alkyl chain stacking peak", or arising from π-stacked units separated by alkyl side chains.[70,73,74] These spacings are consistent with structurally similar molecules[8,62,153] and common conjugated polymers.[158–160] The slow-dried film exhibits the same reflections, as well as additional reflections at q = 0.74, 1.09, and 1.46 Å–1. These additional reflections are attributed to higher order alkyl chain stacking peaks. The π–π stacking peak in the slow-dried film is highly anisotropic, appearing primarily in the in-plane direction. This suggests AT1 preferentially π-stacks in the plane of the substrate, though a more specific understanding of molecular orientation is not possible at this stage, as attempts to grow a suitable single crystal were unsuccessful. The presence of higher order reflections and a preferred orientation of crystallites indicate that AT1 films are able to achieve a greater degree of order when evolved more slowly.

Atomic force microscopy reveals that slow versus fast drying leads to considerably different surface topographic features; see Figure 5.42. Specifically, coarser and blockier features are observed for the slow dried film, compared to a fiber-like morphology when the film dries more quickly.
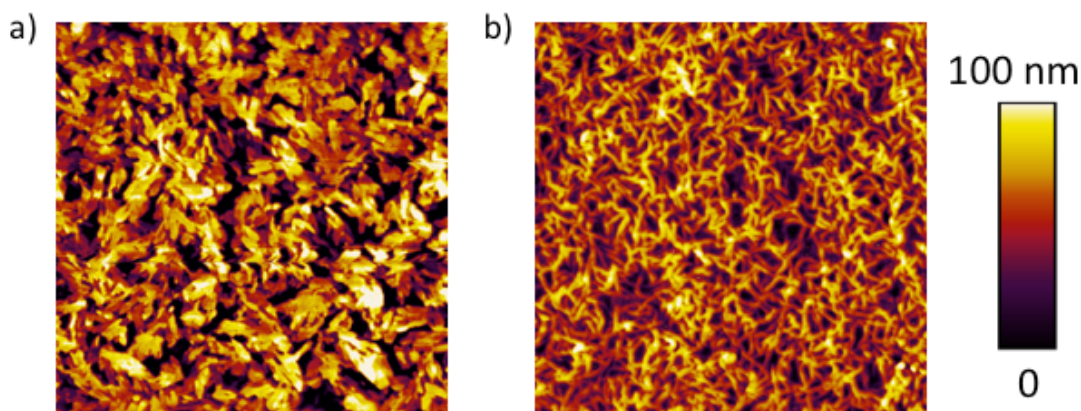
*Figure 5.42. AFM images of AT1 **a)** Slow drying **b)** Fast drying. Images are 5 x 5 μm.*

Charge transport was examined by using a hole-only diode structure in which a film of AT1 was sandwiched between an ITO/poly(3,4-ethylenedioxythiophene)poly(styrene sulfonate) (PEDOT:PSS) bottom electrode and an evaporated Au top contact. Devices containing slow dried films were all electrically shorted, presumably because of the inhomogeneous surface features. Diodes fabricated with the quickly dried films were fit with the space charge limited current model described by the Mott–Gurney law to give a hole mobility of $\mu_p = 2.5 \times 10^{-4} \ cm^2/Vs$ comparable with other BHJ donor materials.[147,161]

5.6.3 Device performance of AT1:PCBM solar cells

Using solution casting conditions which have been successful for structurally similar molecules[9,61] (35 mg/mL chlorobenzene, 50:50 AT1:PCBM), the initial examination of solar cells utilized the device architecture of glass/ITO(~150 nm)/PEDOT:PSS(~35

nm)/BHJ(~80 nm)/Al(~100 nm). Blends were cast from pure solvent, as well as with small amounts of the solvent additive diiodooctane (DIO); see Figure 5.43. As-cast from CB, AT1:PCBM solar cells show negligible performance ($PCE = 0.3\%$, $V_{OC} = 0.59\ V$, $J_{SC} = 1.8\ mA/cm^2$, $FF = 0.26$). Addition of 0.4% DIO by volume to the casting solution enhances the PCE to 1.3% ($V_{OC} = 0.75\ V$, $J_{SC} = 6.4\ VmA/cm^2$, $FF = 0.27$). This increase in V_{OC} begins to approach what would be expected empirically based on the energy levels of AT1.
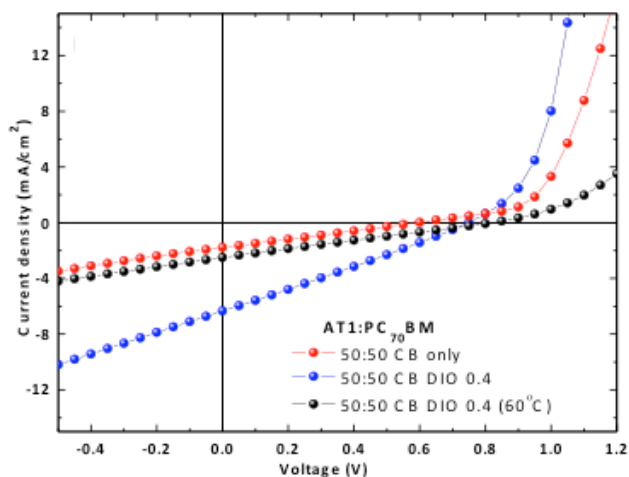
Figure 5.43. JV curves of the AT1/PCBM BHJ solar cells

Crystallization of the donor within the BHJ blend has proven paramount to providing effective molecular OPVs.[9,62,92] We therefore examined the order within any AT1 phase in the BHJ blend films first by examining the absorption profiles of AT1:PCBM films obtained from a number of conditions (Figure 5.44).
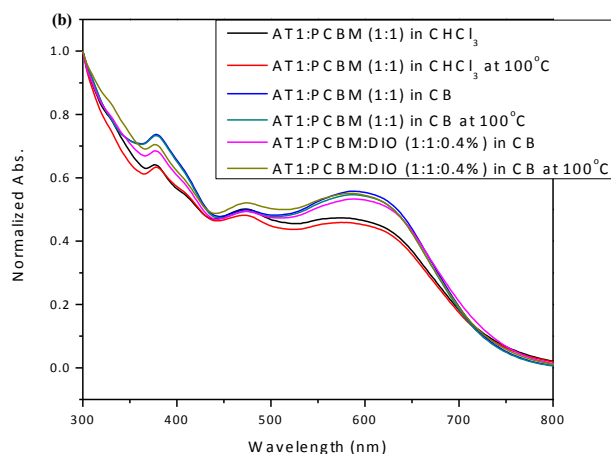
Figure 5.44. Absorption of blend films prepared using different conditions

Despite different solvent, additive, and thermal annealing conditions, the absorption of the blends exhibit no evidence of the vibronic structure related to AT1 crystallization; see the green trace in Figure 5.39a for a representative example. GIWAXS spectra for blend films with and without DIO, provided in Figure 5.45, appear almost identical.
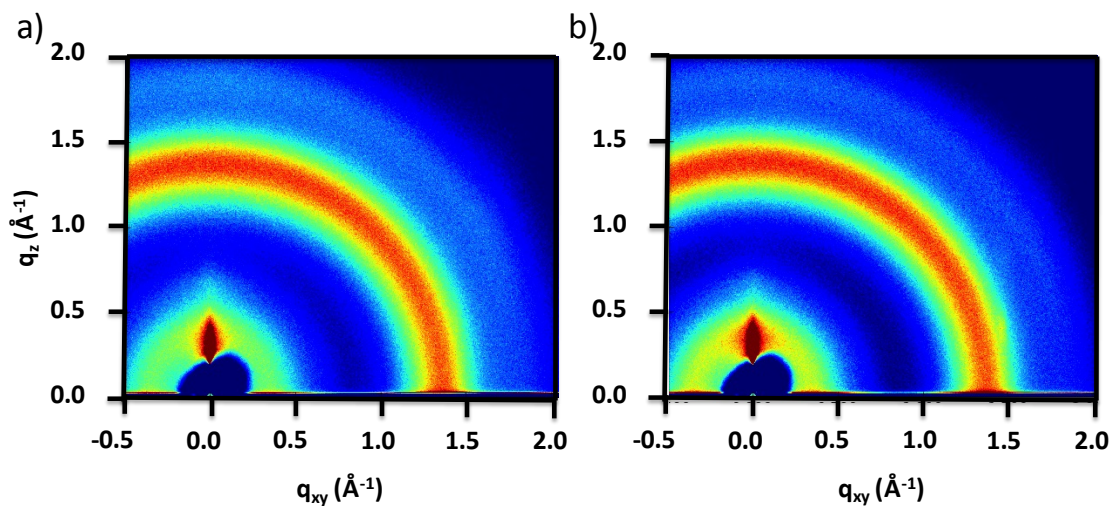
*Figure 5.45. GIWAXS of the blend films of AT1 and PCBM cast from chlorobenzene **a)** without DIO and **b)** with 0.4% DIO.*

173

Although there is some scattering in the region where one would expect alkyl chain stacking reflections from AT1, there are no clear features. There is also no apparent indication of any π–π stacking peak. It is evident that the incorporation of PCBM prevents AT1 from overcoming the kinetic barrier to crystallization resulting in a very poorly organized BHJ blend.
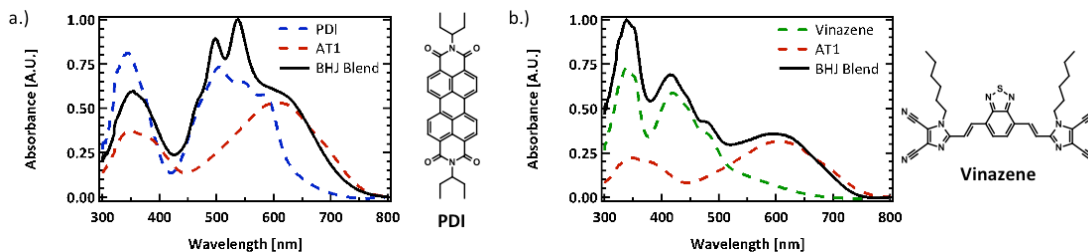
Figure 5.46. Absorption of BHJ films prepared using AT1 blended with a) perylenediimide (PDI) and b) a vinazene derivativeacceptor material with corresponding structures shown to the right.

Additionally, blends of AT1 with two other common acceptor molecules, a perylenediimide and vinazene derivative, showed no evidence of vibronic structure in the absorption traces either (Figure 5.46) indicating that difficulties in crystallization are specific to the structure of the donor material.

5.6.4 Conclusions

In conclusion, AT1 is a single molecule with nearly independent chromophores. The key structural feature is the breakup of delocalization between the C1 and C2 absorbing units via the nonplanar relationship between the two internal thiophene heterocycles. While this feature achieves the desirable objective within the context of the molecule's electronic structure, as inferred from absorption characteristics and DFT analysis, it provides AT1 with an overall nonplanar topology; see Figure 5.40. This "awkward" structure is reminiscent of spiro-type and tetrahedral multichromophore systems that are resistant to crystallization and

174

often provide amorphous thin films.[162,163] A combination of GIWAXS and absorption spectroscopy shows that it is possible to find growth conditions through slow solvent evaporation that yield ordered films of pure AT1. However, the introduction of PCBM exacerbates the kinetic barriers for AT1 crystallization from solution. This absence of crystallization likely impedes achieving the BHJ morphology necessary for achieving high *PCE*. Looking forward, the work highlights the need for developing new processing strategies that allow different film growth profiles of BHJ blends and for design strategies that allow incorporation of multiple absorbing units within a planar molecular topology.

5.7 Conclusions

In Chapters 3 and 4 of this dissertation, it was shown that molecules employing similar architectures required similar processing conditions to achieve high performance. Choosing particular moieties to substitute into the same modular molecular framework served to change the optoelectronic properties but did not disrupt the film-forming process. However, as demonstrated throughout this chapter molecular design is not always quite so simple.

Each of the molecules described in this chapter were designed with specific goals in mind. While changing the regiochemistry of the fluorine atom showed little effect on the devices or the necessary processing conditions, substituting BDT core units disrupted the whole film forming process, resulting in low performance. Furthermore, using a PT acceptor unit with an SIDT core causes instability whichleads to degradation of the material, charge trapping, and thus low performance as well. Adding electron withdrawing moieties to the end of the molecule can quite effectively optimize frontier molecular energy levels, it casues non ideal vertical phase separation and an s-kink in the *JV* curve. Adding DIO helps improve the shape of the curve, but it does not match the performance of its predecessors.

Finally, adding additional decoupled absorbing units to the end does effectively broaden the absorption profile of the material, but disrupts packing such that performance is quite low as well. While such studies did not result in improved performance, in aggregate they emonstrate how subtle changes in structure have pround ramifications with respect to processing and performance.

Chapter 6: Summary and Outlook

In this dissertation, we explore the design of new molecular materials for application as electron donating materials in bulk heterojunction (BHJ) solar cells. Chapters 3 and 4 introduce and examine two important small molecule structures that found success in BHJ devices. They detail the effects of the casting conditions and processing on morphology, that is the nanostructure formed by phase separation, and then relate morphology to device operation. Through physical and electrical characterization we were able to shine light on what is required to achieve high efficiency; a careful balance of crystallinity and phase size. In the final chapter of this dissertation, we explore a number of other structurally similar materials that were targeted synthetically for improved optical and electronic properties, but were less successful in BHJs due to other materials challenges. Despite not achieving high efficiency, each of these materials provided valuable findings and will help guide future synthetic endeavors. They also serve to highlight how difficult it can be to properly manage nanoscale morphology and produce high efficiency BHJ devices.

Although this concludes the research covered in this dissertation, it is encouraging that research with small molecule based BHJs will continue. While much was accomplished over the last five years to help lead to this dissertation, there remains quite a bit of research left before the commercial realization of small molecule organic solar cells. As highlighted in the final chapter, every system seems to require a specific set of empirically determined processing conditions, and creates a bottleneck of the optimization step. A more generalized understanding of processing, and in particular the role of additives, is necessary to streamline the materials screening process. More fundamentally, the role of morphology on

charge generation and extraction is not yet fully understood. While crystallinity and order have clearly been demonstrated to be important, the precise interactions at the donor-acceptor interface remain largely unexplored. Such ideas are being explored with ongoing research using p-SIDT(FBTTh$_2$)$_2$ bilayer devices.

Upon entering the field of organic photovoltaic research in 2010, there was a commonly stated goal of reaching 10% efficiency, which seemed quite challenging at the time. However that milestone came and went, and now there are a number of materials that now reach over 10% in a single cell structure. However, over that same timeframe the price of other solar technologies have pushed forward the target efficiency, with a goal of 15% now seeming necessary. Such a feat would have seemed unattainable a few years ago. Now though, it has become quite routine to hear about new materials and processing methods leading to higher and higher efficiencies, so it seems quite possible that the innovations will continue to come, pushing the field past this $PCE = 15\%$ barrier.

One paradigm shift that has occurred over the last five years, which may help lead the field to commercialization, has been swing in focus towards solution processable small molecule based devices. Although the Nguyen group has been studying small molecules for quite some time, when I first arrived at UCSB, it remained a relatively obscure idea, the vast majority of groups focusing on the higher performing polymer counterparts. Along with work by a number of other people, the work in this thesis has helped garner significant attention for small molecules, which now have broken the 10% barrier themselves. It is quite possible that the work presented here may help pave the way towards small molecule organic solar cells one day being a major source of renewable energy.

References

[1] C. W. Tang, *Applied Physics Letters* **1986**, *48*, 183.

[2] H. Bässler, A. Köhler, *Top Curr Chem* **2012**, *312*, 1.

[3] G. Yu, J. Gao, J. C. Hummelen, F. Wudl, A. J. Heeger, *Science* **1995**, *270*, 1789.

[4] F. Gao, O. Inganäs, *Phys. Chem. Chem. Phys.* **2014**, *16*, 20291.

[5] L. G. Kaake, D. Moses, A. J. Heeger, *J. Phys. Chem. Lett.* **2013**, *4*, 2264.

[6] S. Gélinas, A. Rao, A. Kumar, S. L. Smith, A. W. Chin, J. Clark, T. S. van der Poll, G. C. Bazan, R. H. Friend, *Science* **2014**, *343*, 512.

[7] B. Walker, A. B. Tomayo, X.-D. Dang, P. Zalar, J. H. Seo, A. Garcia, M. Tantiwiwat, T.-Q. Nguyen, *Adv. Funct. Mater.* **2009**, *19*, 3063.

[8] G. C. Welch, L. A. Perez, C. V. Hoven, Y. Zhang, X.-D. Dang, A. Sharenko, M. F. Toney, E. J. Kramer, T.-Q. Nguyen, G. C. Bazan, *J. Mater. Chem.* **2011**, *21*, 12700.

[9] Y. Sun, G. C. Welch, W. L. Leong, C. J. Takacs, G. C. Bazan, A. J. Heeger, *Nature Materials* **2012**, *11*, 44.

[10] Z. Li, G. He, X. Wan, Y. Liu, J. Zhou, G. Long, Y. Zuo, M. Zhang, Y. Chen, *Adv. Energy Mater.* **2012**, *2*, 74.

[11] J. Zhou, X. Wan, Y. Liu, Y. Zuo, Z. Li, G. He, G. Long, W. Ni, C. Li, X. Su, Y. Chen, *J. Am. Chem. Soc.* **2012**, *134*, 16345.

[12] *Compendium of Chemical Terminology, Gold Book*, International Union Of Pure And Applied Chemistry, **2014**.

[13] D. A. Skoog, F. J. Holler, S. R. Crouch, *Principles of Instrumental Analysis*, Thomson Brooks/Cole, **2007**.

[14] J. Pommerehne, H. Vestweber, W. Guss, R. F. Mahrt, H. Bässler, M. Porsch, J. Daub, *Adv. Mater.* **1995**, *7*, 551.

[15] David B. Williams, C. Barry Carter, *Transmission Electron Microscopy*, **n.d.**

[16] G. Binnig, C. F. Quate, C. Gerber, *Phys. Rev. Lett.* **1986**, *56*, 930.

[17] J. Loos, X. Yang, M. M. Koetse, J. Sweelssen, H. F. M. Schoo, S. C. Veenstra, W. Grogger, G. Kothleitner, F. Hofer, *Journal of Applied Polymer Science* **2005**, *97*, 1001.

[18] Z. B. Henson, G. C. Welch, T. van der Poll, G. C. Bazan, *J. Am. Chem. Soc.* **2012**, *134*, 3766.

[19] N. Blouin, A. Michaud, D. Gendron, S. Wakim, E. Blair, R. Neagu-Plesu, M. Belletête, G. Durocher, Y. Tao, M. Leclerc, *J. Am. Chem. Soc.* **2008**, *130*, 732.

[20] J. W. Tilley, S. Zawoiski, *J. Org. Chem.* **1988**, *53*, 386.

[21] A. Ernst, L. Gobbi, A. Vasella, *Tetrahedron Letters* **1996**, *37*, 7959.

[22] S. T. Handy, T. Wilson, A. Muth, *J. Org. Chem.* **2007**, *72*, 8496.

[23] E. L. Ratcliff, R. C. B. Ii, G. C. Welch, T. S. van der Poll, A. Garcia, S. R. Cowan, B. A. MacLeod, D. S. Ginley, G. C. Bazan, D. C. Olson, *J. Mater. Chem. C* **2013**, *1*, 6223.

[24] Y. Zhang, S.-C. Chien, K.-S. Chen, H.-L. Yip, Y. Sun, J. A. Davies, F.-C. Chen, A. K.-Y. Jen, *Chemical Communications* **2011**, *47*, 11026.

[25] Q. Peng, X. Liu, D. Su, G. Fu, J. Xu, L. Dai, *Adv. Mater.* **2011**, *23*, 4554.

[26] H.-Y. Chen, J. Hou, S. Zhang, Y. Liang, G. Yang, Y. Yang, L. Yu, Y. Wu, G. Li, *Nat Photon* **2009**, *3*, 649.

[27] H. J. Son, W. Wang, T. Xu, Y. Liang, Y. Wu, G. Li, L. Yu, *Journal of the American Chemical Society* **2011**, *133*, 1885.

[28] B. C. Schroeder, Z. Huang, R. S. Ashraf, J. Smith, P. D'Angelo, S. E. Watkins, T. D. Anthopoulos, J. R. Durrant, I. McCulloch, *Advanced Functional Materials* **2012**, *22*, 1663.

[29] M. Sharif, M. Zeeshan, S. Reimann, A. Villinger, P. Langer, *Tetrahedron Letters* **2010**, *51*, 2810.

[30] J. Gierschner, M. Ehni, H.-J. Egelhaaf, B. M. Medina, D. Beljonne, H. Benmansour, G. C. Bazan, *The Journal of Chemical Physics* **2005**, *123*, 144914.

[31] O. Ostroverkhova, S. Shcherbyna, D. G. Cooke, R. F. Egerton, F. A. Hegmann, R. R. Tykwinski, S. R. Parkin, J. E. Anthony, *Journal of Applied Physics* **2005**, *98*, 033701.

[32] T. Johansson, W. Mammo, M. Svensson, M. R. Andersson, O. Inganäs, *J. Mater. Chem.* **2003**, *13*, 1316.

[33] B. P. Rand, D. P. Burk, S. R. Forrest, *Phys. Rev. B* **2007**, *75*, 115327.

[34] M. C. Scharber, D. Mühlbacher, M. Koppe, P. Denk, C. Waldauf, A. J. Heeger, C. J. Brabec, *Advanced Materials* **2006**, *18*, 789.

[35] V. D. Mihailetchi, L. J. A. Koster, J. C. Hummelen, P. W. M. Blom, *Phys. Rev. Lett.* **2004**, *93*, 216601.

[36] N. A. Ran, M. Kuik, J. A. Love, C. M. Proctor, I. Nagao, G. C. Bazan, T.-Q. Nguyen, *Adv. Mater.* **2014**, *26*, 7405.

[37] R. A. Marsh, J. M. Hodgkiss, S. Albert-Seifried, R. H. Friend, *Nano Lett.* **2010**, *10*, 923.

[38] K. Kim, J. Liu, M. A. G. Namboothiry, D. L. Carroll, *Applied Physics Letters* **2007**, *90*, 163511.

[39] G. F. Burkhard, E. T. Hoke, M. D. McGehee, *Advanced Materials* **2010**, *22*, 3293.

[40] J. Mizuguchi, *J. Phys. Chem. A* **2000**, *104*, 1817.

[41] T. Erb, U. Zhokhavets, G. Gobsch, S. Raleva, B. Stühn, P. Schilinsky, C. Waldauf, C. J. Brabec, *Advanced Functional Materials* **2005**, *15*, 1193.

[42] T. Martens, J. D'Haen, T. Munters, Z. Beelen, L. Goris, J. Manca, M. D'Olieslaeger, D. Vanderzande, L. De Schepper, R. Andriessen, *Synthetic Metals* **2003**, *138*, 243.

[43] D. M. DeLongchamp, R. J. Kline, A. Herzing, *Energy Environ. Sci.* **2012**, *5*, 5980.

[44] K. R. Graham, P. M. Wieruszewski, R. Stalder, M. J. Hartel, J. Mei, F. So, J. R. Reynolds, *Adv. Funct. Mater.* **2012**, *22*, 4801.

[45] J. S. Moon, C. J. Takacs, Y. Sun, A. J. Heeger, *Nano Lett.* **2011**, *11*, 1036.

[46] J. Y. Kim, K. Lee, N. E. Coates, D. Moses, T.-Q. Nguyen, M. Dante, A. J. Heeger, *Science* **2007**, *317*, 222.

[47] J. S. Moon, C. J. Takacs, S. Cho, R. C. Coffin, H. Kim, G. C. Bazan, A. J. Heeger, *Nano Lett.* **2010**, *10*, 4005.

[48] N. I. Kato, *J Electron Microsc (Tokyo)* **2004**, *53*, 451.

[49] J. E. Anthony, *Chem. Rev.* **2006**, *106*, 5028.

[50] J. E. Anthony, J. S. Brooks, D. L. Eaton, S. R. Parkin, *Journal of the American Chemical Society* **2001**, *123*, 9482.

[51] S. Haid, M. Marszalek, A. Mishra, M. Wielopolski, J. Teuscher, J.-E. Moser, R. Humphry-Baker, S. M. Zakeeruddin, M. Grätzel, P. Bäuerle, *Advanced Functional Materials* **2012**, *22*, 1291.

[52] C. Kim, J. Liu, J. Lin, A. B. Tamayo, B. Walker, G. Wu, T.-Q. Nguyen, *Chem. Mater.* **2012**, *24*, 1699.

[53] J. Liu, B. Walker, A. Tamayo, Y. Zhang, T.-Q. Nguyen, *Advanced Functional Materials* **2013**, *23*, 47.

[54] V. Coropceanu, J. Cornil, D. A. da Silva Filho, Y. Olivier, R. Silbey, J.-L. Brédas, *Chem. Rev.* **2007**, *107*, 926.

[55] A. Hadipour, B. de Boer, J. Wildeman, F. B. Kooistra, J. C. Hummelen, M. G. R. Turbiez, M. M. Wienk, R. a. J. Janssen, P. W. M. Blom, *Advanced Functional Materials* **2006**, *16*, 1897.

[56] G. Dennler, M. C. Scharber, T. Ameri, P. Denk, K. Forberich, C. Waldauf, C. J. Brabec, *Advanced Materials* **2008**, *20*, 579.

[57] J. You, L. Dou, K. Yoshimura, T. Kato, K. Ohya, T. Moriarty, K. Emery, C.-C. Chen, J. Gao, G. Li, Y. Yang, *Nat Commun* **2013**, *4*, 1446.

[58] L. Dou, J. You, J. Yang, C.-C. Chen, Y. He, S. Murase, T. Moriarty, K. Emery, G. Li, Y. Yang, *Nat Photon* **2012**, *6*, 180.

[59] W. Li, A. Furlan, K. H. Hendriks, M. M. Wienk, R. A. J. Janssen, *J. Am. Chem. Soc.* **2013**, *135*, 5529.

[60] J. Zhou, Y. Zuo, X. Wan, G. Long, Q. Zhang, W. Ni, Y. Liu, Z. Li, G. He, C. Li, B. Kan, M. Li, Y. Chen, *J. Am. Chem. Soc.* **2013**, *135*, 8484.

[61] T. S. van der Poll, J. A. Love, T.-Q. Nguyen, G. C. Bazan, *Advanced Materials* **2012**, *24*, 3646.

[62] J. A. Love, C. M. Proctor, J. Liu, C. J. Takacs, A. Sharenko, T. S. van der Poll, A. J. Heeger, G. C. Bazan, T.-Q. Nguyen, *Advanced Functional Materials* **2013**, *23*, 5019.

[63] V. Gupta, A. K. K. Kyaw, D. H. Wang, S. Chand, G. C. Bazan, A. J. Heeger, *Sci. Rep.* **2013**, *3*, 1965.

[64] C. Duan, F. Huang, Y. Cao, *Journal of Materials Chemistry* **2012**, *22*, 10416.

[65] R. S. Ashraf, B. C. Schroeder, H. A. Bronstein, Z. Huang, S. Thomas, R. J. Kline, C. J. Brabec, P. Rannou, T. D. Anthopoulos, J. R. Durrant, I. McCulloch, *Advanced Materials* **2013**, *25*, 2029.

[66] R. S. Ashraf, Z. Chen, D. S. Leem, H. Bronstein, W. Zhang, B. Schroeder, Y. Geerts, J. Smith, S. Watkins, T. D. Anthopoulos, H. Sirringhaus, J. C. de Mello, M. Heeney, I. McCulloch, *Chem. Mater.* **2011**, *23*, 768.

[67] J.-Y. Wang, S. K. Hau, H.-L. Yip, J. A. Davies, K.-S. Chen, Y. Zhang, Y. Sun, A. K.-Y. Jen, *Chem. Mater.* **2011**, *23*, 765.

[68] J. You, L. Dou, K. Yoshimura, T. Kato, K. Ohya, T. Moriarty, K. Emery, C.-C. Chen, J. Gao, G. Li, Y. Yang, *Nat Commun* **2013**, *4*, 1446.

[69] G. C. Welch, R. C. Bakus, S. J. Teat, G. C. Bazan, *J. Am. Chem. Soc.* **2013**, *135*, 2298.

[70] J. L. Baker, L. H. Jimison, S. Mannsfeld, S. Volkman, S. Yin, V. Subramanian, A. Salleo, A. P. Alivisatos, M. F. Toney, *Langmuir* **2010**, *26*, 9146.

[71] W. Zhang, J. Smith, S. E. Watkins, R. Gysel, M. McGehee, A. Salleo, J. Kirkpatrick, S. Ashraf, T. Anthopoulos, M. Heeney, I. McCulloch, *J. Am. Chem. Soc.* **2010**, *132*, 11437.

[72] I. McCulloch, R. S. Ashraf, L. Biniek, H. Bronstein, C. Combe, J. E. Donaghey, D. I. James, C. B. Nielsen, B. C. Schroeder, W. Zhang, *Acc. Chem. Res.* **2012**, *45*, 714.

[73] J. T. Rogers, K. Schmidt, M. F. Toney, E. J. Kramer, G. C. Bazan, *Advanced Materials* **2011**, *23*, 2284.

[74] C. Du, W. Li, Y. Duan, C. Li, H. Dong, J. Zhu, W. Hu, Z. Bo, *Polym. Chem.* **2013**, *4*, 2773.

[75] A. C. Dürr, F. Schreiber, M. Münch, N. Karl, B. Krause, V. Kruppa, H. Dosch, *Applied Physics Letters* **2002**, *81*, 2276.

[76] Y. M. Sun, Y. Q. Ma, Y. Q. Liu, Y. Y. Lin, Z. Y. Wang, Y. Wang, C. A. Di, K. Xiao, X. M. Chen, W. F. Qiu, B. Zhang, G. Yu, W. P. Hu, D. B. Zhu, *Advanced Functional Materials* **2006**, *16*, 426.

[77] J. I. Langford, A. J. C. Wilson, *Journal of Applied Crystallography* **1978**, *11*, 102.

[78] D. Chen, A. Nakahara, D. Wei, D. Nordlund, T. P. Russell, *Nano Lett.* **2011**, *11*, 561.

[79] Y. Chen, X. Wan, G. Long, *Acc. Chem. Res.* **2013**, *46*, 2645.

[80] V. D. Mihailetchi, J. Wildeman, P. W. M. Blom, *Phys. Rev. Lett.* **2005**, *94*, 126602.

[81] D. Di Nuzzo, S. van Reenen, R. A. J. Janssen, M. Kemerink, S. C. J. Meskers, *Phys. Rev. B* **2013**, *87*, 085207.

[82] S. Scheinert, M. Grobosch, J. Sprogies, I. Hörselmann, M. Knupfer, G. Paasch, *Journal of Applied Physics* **2013**, *113*, 174504.

[83] X. Yang, *Semiconducting Polymer Composites: Principles, Morphologies, Properties and Applications*, John Wiley & Sons, **2012**.

[84] D. Stauffer, A. Aharony, *Introduction To Percolation Theory*, CRC Press, **1994**.

[85] M. Sahini, M. Sahimi, *Applications Of Percolation Theory*, CRC Press, **1994**.

[86] R. Zallen, *The Physics of Amorphous Solids*, Wiley, **1998**.

[87] K. Levon, A. Margolina, A. Z. Patashinsky, *Macromolecules* **1993**, *26*, 4061.

[88] C. Kübel, L. González-Ronda, L. F. Drummy, D. C. Martin, *Journal of Physical Organic Chemistry* **2000**, *13*, 816.

[89] J. Li, B. Ray, M. A. Alam, M. Östling, *Phys. Rev. E* **2012**, *85*, 021109.

[90] C. J. Brabec, N. S. Sariciftci, J. C. Hummelen, *Advanced Functional Materials* **2001**, *11*, 15.

[91] V. d. Mihailetchi, J. k. j. van Duren, P. w. m. Blom, J. c. Hummelen, R. a. j. Janssen, J. m. Kroon, M. t. Rispens, W. j. h. Verhees, M. m. Wienk, *Advanced Functional Materials* **2003**, *13*, 43.

[92] C. J. Takacs, Y. Sun, G. C. Welch, L. A. Perez, X. Liu, W. Wen, G. C. Bazan, A. J. Heeger, *J. Am. Chem. Soc.* **2012**, *134*, 16597.

[93] E. D. Gomez, K. P. Barteau, H. Wang, M. F. Toney, Y.-L. Loo, *Chem. Commun.* **2010**, *47*, 436.

[94] A. J. Lovinger, H. E. Katz, A. Dodabalapur, *Chem. Mater.* **1998**, *10*, 3275.

[95] D. C. Martin, J. Chen, J. Yang, L. F. Drummy, C. Kübel, *Journal of Polymer Science Part B: Polymer Physics* **2005**, *43*, 1749.

[96] G. S, N. H, S. Ns, *Chem. Rev.* **2007**, *107*, 1324.

[97] A. Pivrikas, N. S. Sariciftci, G. Juška, R. Österbacka, *Progress in Photovoltaics: Research and Applications* **2007**, *15*, 677.

[98] C. M. Proctor, M. Kuik, T.-Q. Nguyen, *Progress in Polymer Science* **2013**, *38*, 1941.

[99] S. R. Cowan, A. Roy, A. J. Heeger, *Phys. Rev. B* **2010**, *82*, 245207.

[100] L. J. A. Koster, V. D. Mihailetchi, R. Ramaker, P. W. M. Blom, *Applied Physics Letters* **2005**, *86*, 123509.

[101] A. Maurano, R. Hamilton, C. G. Shuttle, A. M. Ballantyne, J. Nelson, B. O'Regan, W. Zhang, I. McCulloch, H. Azimi, M. Morana, C. J. Brabec, J. R. Durrant, *Advanced Materials* **2010**, *22*, 4987.

[102] G. F. A. Dibb, T. Kirchartz, D. Credgington, J. R. Durrant, J. Nelson, *J. Phys. Chem. Lett.* **2011**, *2*, 2407.

[103] A. M. Goodman, A. Rose, *Journal of Applied Physics* **2003**, *42*, 2823.

[104] L. M. Andersson, C. Müller, B. H. Badada, F. Zhang, U. Würfel, O. Inganäs, *Journal of Applied Physics* **2011**, *110*, 024509.

[105] S. Albrecht, S. Janietz, W. Schindler, J. Frisch, J. Kurpiers, J. Kniepert, S. Inal, P. Pingel, K. Fostiropoulos, N. Koch, D. Neher, *J. Am. Chem. Soc.* **2012**, *134*, 14932.

[106] K. Tvingstedt, K. Vandewal, F. Zhang, O. Inganäs, *J. Phys. Chem. C* **2010**, *114*, 21824.

[107] D. Credgington, F. C. Jamieson, B. Walker, T.-Q. Nguyen, J. R. Durrant, *Advanced Materials* **2012**, *24*, 2135.

[108] A. Hadipour, B. de Boer, P. W. M. Blom, *Advanced Functional Materials* **2008**, *18*, 169.

[109] D. Meyerhofer, *Journal of Applied Physics* **2008**, *49*, 3993.

[110] D. T. Duong, B. Walker, J. Lin, C. Kim, J. Love, B. Purushothaman, J. E. Anthony, T.-Q. Nguyen, *Journal of Polymer Science Part B: Polymer Physics* **2012**, *50*, 1405.

[111] D. B. Hall, P. Underhill, J. M. Torkelson, *Polymer Engineering & Science* **1998**, *38*, 2039.

[112] E. Mohajerani, F. Farajollahi, R. Mahzoon, S. Baghery, *J. Optoelectron. Adv. Mater.* **2007**, *9*, 3901.

[113] C. B. Walsh, E. I. Franses, *Thin Solid Films* **2003**, *429*, 71.

[114] M. Lenes, L. J. A. Koster, V. D. Mihailetchi, P. W. M. Blom, *Applied Physics Letters* **2006**, *88*, 243502.

[115] G. Li, V. Shrotriya, Y. Yao, Y. Yang, *Journal of Applied Physics* **2005**, *98*, 043704.

[116] D. W. Sievers, V. Shrotriya, Y. Yang, *J. Appl. Phys.* **2006**, *100*, 114509.

[117] T. Kirchartz, T. Agostinelli, M. Campoy-Quiles, W. Gong, J. Nelson, *J. Phys. Chem. Lett.* **2012**, *3*, 3470.

[118] V. D. Mihailetchi, H. X. Xie, B. de Boer, L. J. A. Koster, P. W. M. Blom, *Advanced Functional Materials* **2006**, *16*, 699.

[119] J. D. Kotlarski, D. J. D. Moet, P. W. M. Blom, *J. Polym. Sci. Pt. B-Polym. Phys.* **2011**, *49*, 708.

[120] C. J. Lawrence, *Physics of Fluids (1958-1988)* **1988**, *31*, 2786.

[121] M. A. Aegerter, M. Mennig, *Sol-Gel Technologies for Glass Producers and Users*, Springer, **2004**.

[122] D. E. Bornside, C. W. Macosko, L. E. Scriven, *Journal of Applied Physics* **1989**, *66*, 5185.

[123] T. Ohara, Y. Matsumoto, H. Ohashi, *Physics of Fluids A: Fluid Dynamics (1989-1993)* **1989**, *1*, 1949.

[124] V. Mittal, *Polymers for Energy Storage and Conversion*, John Wiley & Sons, **2013**.

[125] E. A. Guggenheim, *Trans. Faraday Soc.* **1937**, *33*, 151.

[126] D. R. Stull, *Industrial & Engineering Chemistry* **1947**, *39*, 517.

[127] W.-Y. Shiu, K.-C. Ma, *Journal of Physical and Chemical Reference Data* **2000**, *29*, 387.

[128] L. Ye, Y. Jing, X. Guo, H. Sun, S. Zhang, M. Zhang, L. Huo, J. Hou, *J. Phys. Chem. C* **2013**, *117*, 14920.

[129]   Y. Kim, G. Kim, J. Lee, K. Lee, *Solar Energy Materials and Solar Cells* **2012**, *105*, 272.

[130]   L. A. Perez, J. T. Rogers, M. A. Brady, Y. Sun, G. C. Welch, K. Schmidt, M. F. Toney, H. Jinnai, A. J. Heeger, M. L. Chabinyc, G. C. Bazan, E. J. Kramer, *Chem. Mater.* **2014**, *26*, 6531.

[131]   J. T. Rogers, K. Schmidt, M. F. Toney, G. C. Bazan, E. J. Kramer, *J. Am. Chem. Soc.* **2012**, *134*, 2884.

[132]   D. C. Coffey, O. G. Reid, D. B. Rodovsky, G. P. Bartholomew, D. S. Ginger, *Nano Lett.* **2007**, *7*, 738.

[133]   L. S. C. Pingree, O. G. Reid, D. S. Ginger, *Nano Lett.* **2009**, *9*, 2946.

[134]   M. Guide, X.-D. Dang, T.-Q. Nguyen, *Advanced Materials* **2011**, *23*, 2313.

[135]   X.-D. Dang, A. Mikhailovsky, T.-Q. Nguyen, *Applied Physics Letters* **2010**, *97*, 113303.

[136]   B. A. Collins, J. E. Cochran, H. Yan, E. Gann, C. Hub, R. Fink, C. Wang, T. Schuettfort, C. R. McNeill, M. L. Chabinyc, H. Ade, *Nat Mater* **2012**, *11*, 536.

[137]   B. A. Collins, Z. Li, J. R. Tumbleston, E. Gann, C. R. McNeill, H. Ade, *Advanced Energy Materials* **2013**, *3*, 65.

[138]   J. R. Tumbleston, A. C. Stuart, E. Gann, W. You, H. Ade, *Advanced Functional Materials* **2013**, *23*, 3463.

[139]   W. Ma, J. R. Tumbleston, L. Ye, C. Wang, J. Hou, H. Ade, *Adv. Mater.* **2014**, *26*, 4234.

[140]   T. Coffey, S. G. Urquhart, H. Ade, *Journal of Electron Spectroscopy and Related Phenomena* **2002**, *122*, 65.

[141]   W. L. Leong, G. C. Welch, J. Seifter, J. H. Seo, G. C. Bazan, A. J. Heeger, *Adv. Energy Mater.* **2013**, *3*, 356.

[142]   J. E. Coughlin, A. Zhugayevych, R. C. Bakus, T. S. van der Poll, G. C. Welch, S. J. Teat, G. C. Bazan, S. Tretiak, *J. Phys. Chem. C* **2014**, *118*, 15610.

[143]   Y. Liu, X. Wan, F. Wang, J. Zhou, G. Long, J. Tian, Y. Chen, *Adv. Mater.* **2011**, *23*, 5387.

[144]   S. Shen, P. Jiang, C. He, J. Zhang, P. Shen, Y. Zhang, Y. Yi, Z. Zhang, Z. Li, Y. Li, *Chem. Mater.* **2013**, *25*, 2274.

[145]   L. Dou, J. You, Z. Hong, Z. Xu, G. Li, R. A. Street, Y. Yang, *Advanced Materials* **2013**, *25*, 6642.

[146]   Y. Liu, J. Zhao, Z. Li, C. Mu, W. Ma, H. Hu, K. Jiang, H. Lin, H. Ade, H. Yan, *Nat Commun* **2014**, *5*, 5293.

[147]   B. Walker, C. Kim, T.-Q. Nguyen, *Chem. Mater.* **2011**, *23*, 470.

[148]   Y. Liu, C.-C. Chen, Z. Hong, J. Gao, Y. (Michael) Yang, H. Zhou, L. Dou, G. Li, Y. Yang, *Sci Rep* **2013**, *3*, 3356.

[149]   J. E. Coughlin, Z. B. Henson, G. C. Welch, G. C. Bazan, *Acc. Chem. Res.* **2014**, *47*, 257.

[150]   Y. Liu, X. Wan, B. Yin, J. Zhou, G. Long, S. Yin, Y. Chen, *J. Mater. Chem.* **2010**, *20*, 2464.

[151]   G. He, Z. Li, X. Wan, Y. Liu, J. Zhou, G. Long, M. Zhang, Y. Chen, *J. Mater. Chem.* **2012**, *22*, 9173.

[152]   G. He, Z. Li, X. Wan, J. Zhou, G. Long, S. Zhang, M. Zhang, Y. Chen, *J. Mater. Chem. A* **2013**, *1*, 1801.

[153] J. A. Love, I. Nagao, Y. Huang, M. Kuik, V. Gupta, C. J. Takacs, J. E. Coughlin, L. Qi, T. S. van der Poll, E. J. Kramer, A. J. Heeger, T.-Q. Nguyen, G. C. Bazan, *J. Am. Chem. Soc.* **2014**, *136*, 3597.

[154] L.-Y. Lin, C.-W. Lu, W.-C. Huang, Y.-H. Chen, H.-W. Lin, K.-T. Wong, *Org. Lett.* **2011**, *13*, 4962.

[155] A. Zhugayevych, O. Postupna, R. C. Bakus II, G. C. Welch, G. C. Bazan, S. Tretiak, *J. Phys. Chem. C* **2013**, *117*, 4920.

[156] T. Yanai, D. P. Tew, N. C. Handy, *Chemical Physics Letters* **2004**, *393*, 51.

[157] Y. Takano, K. N. Houk, *J. Chem. Theory Comput.* **2005**, *1*, 70.

[158] W. Ma, C. Yang, X. Gong, K. Lee, A. J. Heeger, *Advanced Functional Materials* **2005**, *15*, 1617.

[159] C.-W. Chu, H. Yang, W.-J. Hou, J. Huang, G. Li, Y. Yang, *Applied Physics Letters* **2008**, *92*, 103306.

[160] M. L. Chabinyc, M. F. Toney, R. J. Kline, I. McCulloch, M. Heeney, *J. Am. Chem. Soc.* **2007**, *129*, 3226.

[161] N. I. Craciun, J. Wildeman, P. W. M. Blom, *Phys. Rev. Lett.* **2008**, *100*, 056601.

[162] A. L. Kanibolotsky, I. F. Perepichka, P. J. Skabara, *Chem. Soc. Rev.* **2010**, *39*, 2695.

[163] P. J. Skabara, J.-B. Arlin, Y. H. Geerts, *Adv. Mater.* **2013**, *25*, 1948.